

MECHANICALLY ADJUSTABLE SINGLE-MOLECULE
TRANSISTORS AND STENCIL MASK
NANOFABRICATION OF HIGH-RESOLUTION
SCANNING PROBES

A Dissertation

Presented to the Faculty of the Graduate School

of Cornell University

in Partial Fulfillment of the Requirements for the Degree of

Doctor of Philosophy

by

Alexandre Champagne

August 2005

This document is in the public domain.

MECHANICALLY ADJUSTABLE SINGLE-MOLECULE TRANSISTORS AND
STENCIL MASK NANOFABRICATION OF HIGH-RESOLUTION SCANNING
PROBES

Alexandre Champagne, Ph.D.

Cornell University 2005

This dissertation presents the development of two original experimental techniques to probe nanoscale objects. The first one studies electronic transport in single organic molecule transistors in which the source-drain electrode spacing is mechanically adjustable. The second involves the fabrication of high-resolution scanning probe microscopy sensors using a stencil mask lithography technique.

We describe the fabrication of transistors in which a single organic molecule can be incorporated. The source and drain leads of these transistors are freely suspended above a flexible substrate, and their spacing can be adjusted by bending the substrate. We detail the technology developed to carry out measurements on these samples.

We study electronic transport in single C_{60} molecules at low temperature. We observe Coulomb blockaded transport and can resolve the discrete energy spectrum of the molecule. We are able to mechanically tune the spacing between the electrodes (over a range of 5 Å) to modulate the lead-molecule coupling, and can electrostatically tune the energy levels on the molecule by up to 160 meV using a gate electrode. Initial progress in studying different transport regimes in other molecules is also discussed.

We present a lithographic process that allows the deposition of metal nanostructures with a resolution down to 10 nm directly onto atomic force microscope (AFM) tips. We show that multiple layers of lithography can be deposited and aligned. We fabricate high-resolution magnetic force microscopy (MFM) probes using this method and discuss progress to fabricate other scanning probe microscopy (SPM) sensors.

BIOGRAPHICAL SKETCH

Alexandre Champagne was born in 1977 in Trois-Rivières, Québec, Canada. He enjoyed a happy childhood with his brother Frédéric. He mostly spent his high-school years playing sports. After the mandatory two-years in community college, he went on to obtain a B.S. in physics from McGill University in Montréal. While at McGill he managed to learn English. He then joined the physics Ph.D. program at Cornell. He has enjoyed his six years in Ithaca, doing work he loves and playing with great friends. To his own surprise, he is now headed for California. He will be pursuing a post-doc at Caltech. He plans on returning to his frozen homeland someday.

À mes parents,
Lise et Michel.

“People do not care how much you know,
until they know how much you care.”

Anonymous

ACKNOWLEDGEMENTS

What I have, I owe to many. I happily acknowledge the ones that have made my stay in Ithaca and at Cornell both enjoyable and enriching.

Let me first thank my advisor, Dan Ralph. You have been outstanding in all regards. I could not have asked for a better advisor. Your love of science, knowledge, patience, support and hard work have helped me a great deal. I am deeply grateful.

Thanks to Paul McEuen for his advice on my experiments and his help with finding a job and writing my thesis. Thanks to Piet Brouwer for his teaching, helping me get a job and acting as a proxy for my defense. Thank you Jim Sethna for your enthusiasm and helping with my A exam and thesis.

I would like to thank the entire Ralph group and McEuen group, for their help in countless ways. Thank you Aaron for introducing me to experimental physics. Thanks, Mandar and Ed for welcoming me to the group when I was just a clueless kid. Your advices were precious and your energy made it fun to work in the lab. Thanks to Alex Corwin for his help with all my computer problems and for the fun conversations. Thank you Jason for teaching me about nanofabrication and being a friend. A very special thank you to Abhay. You have been quite extraordinary. Your talent speaks for itself, and your expert help and kind support have been very important to me. Sergey, you have been a wonderful labmate, thanks for all the tips. Thank you to Ferdinand and Kirill. Both of you have been good friends over the last few years, and have made my time in the lab seem like play time. Your passion for science and your knowledge of just about anything were very precious. Jack and Jacob, thank you for being passionate and fun labmates. Thank you Janice for your help with my thesis, and for all the conversations. Thank you

Josh for putting up with me over the last year. You have rapidly become a skilled experimentalist and I am happy to pass on to you my experiment. I wish you tons of success. Thanks to Jiwoong, Ethan, Marie, Ilya, Kiran, Markus, Sami, Vera, Jun, Ken, Luke, Edgar, Chad, Andrew Perella, it was a pleasure to get to know you and have your knowledge at hand.

Thank you Sned for significantly increasing my manhood by showing me how to machine metal and make lots of smoke. Thanks to Ron Kemp for his help in TOL. Thank you very much to Carol Daugherty for maintaining the Hitachi SEM at the veterinary school, which has been so precious for both of my projects.

I want to thank all my friends in Ithaca that have made my time here heaps of fun. Thank you Xavier, Javail, Jeremy, Barbara, Mike, Dan Pringle, Chris, Yanqi, Diane, Dayne, and all the ones I have forgotten to include.

Thanks to my lifelong friends from Québec without whom life would not be as much fun. Thank you Marc, Patrick, Mathieu, Simon, Yan and Martin. I look forward to another fifty years of parties at the lake.

Last but foremost, I want to thank my parents. Merci cher parents pour tout ce que vous m'avez donné. Votre soutien et amour sont ce que j'ai de plus précieux.

TABLE OF CONTENTS

1	Introduction	1
1.1	Perspective	1
1.2	Single-molecule electronics	3
1.2.1	Electrostatically controlled single-molecule junctions	5
1.2.2	Mechanically controlled single-molecule junctions	9
1.3	High-resolution scanning probe microscopy	11
1.4	Organization of this thesis	14
	Bibliography	17
2	Coulomb blockade in a mechanically-adjustable transistor	19
2.1	Single-electron tunneling	21
2.1.1	Charging energy	21
2.1.2	Tunneling thresholds	22
2.1.3	Tunnel rates	25
2.2	Electrostatic control: resolving excited energy levels	26
2.3	Mechanical control: changing the lead-molecule coupling	28
	Bibliography	32
3	Fabrication of mechanically-adjustable single-molecule transistors	33
3.1	Introduction	33
3.2	Silicon-back-gate devices	34
3.2.1	Field oxide	34
3.2.2	Photolithography and gate oxide	37
3.2.3	Electron-beam lithography	44
3.2.4	Dicing, final wet oxide etch, and SEM imaging	47
3.3	Electromigration	51
3.4	Nanotube devices	52
3.5	Metallic particle devices	57
	Bibliography	61
4	Measurement setup: gated-mechanically controllable break-junction technique (g-MCBJ)	62
4.1	Introduction	62
4.2	Four Kelvin setup	63
4.2.1	Mechanical assembly	66
4.2.2	Sample handling	66
4.2.3	Mechanical motion calibration	68
4.3	Variable temperature setup	73
4.3.1	Mechanical assembly	74

4.3.2	VTI assembly motion calibration	74
4.4	Electronics	77
4.5	Future improvements	79
Bibliography		80
5	Electrostatic and mechanical control in single-C₆₀ devices	81
5.1	Introduction	81
5.2	Sample preparation	82
5.3	Gate and mechanical control	84
5.3.1	Changes in conductance and capacitances	84
5.3.2	Changes in the gate voltage degeneracy point	88
5.4	Conclusions	92
Bibliography		94
6	Other experiments with g-MCBJs and outlook	95
6.1	Kondo physics in single-molecule transistors	95
6.2	Vibrational energy levels in single molecules	102
6.3	Short carbon nanotubes	102
6.4	Metallic dots	106
Bibliography		108
7	A custom Atomic Force Microscope (AFM) for fabricating high-resolution scanning probes	109
7.1	Introduction	109
7.1.1	Review of some fabrication processes used to make scanning probes	111
7.1.2	Pattern transfer on AFM tips using a stencil mask: technical requirements	116
7.2	Instrument design	117
7.2.1	The evaporation system	117
7.2.2	The microscope	119
7.2.3	Tuning fork feedback, electronics and software	127
Bibliography		137
8	Nanometer-scale scanning probes built using stencil lithography	138
8.1	Stencil Mask Fabrication	138
8.1.1	Fabrication steps	140
8.1.2	Stencil design and characterization	146
8.2	Pattern transfer procedure	151
8.2.1	Tip preparation	151
8.2.2	Alignment procedure	152

8.2.3	Evaporation	156
8.3	Results	159
8.3.1	Lithographic capabilities	160
8.3.2	Magnetic probes	162
8.3.3	Progress toward making strong coupling gated-STM probes .	167
8.4	Outlook	172
Bibliography		177
A	Numerical simulation of Coulomb blockade in mechanically-adjustable single-molecule transistors	179
A.1	Introduction	179
A.2	Mathematica code	179

LIST OF TABLES

8.1	Pattern transfer procedure for stencil lithography on AFM tips . . .	158
-----	--	-----

LIST OF FIGURES

1.1	Molecular motor	2
1.2	Probing correlated electrons	4
1.3	Single-molecule electronic devices	6
1.4	Electromigration break-junction	8
1.5	Mechanically controllable break-junction	10
1.6	Atomic Force Microscopy	12
1.7	Scanning Probe Microscopy	13
2.1	Circuit diagram of a single-molecule transistor	20
2.2	Coulomb blockade diamond	23
2.3	Excited energy levels	27
2.4	Numerical simulation of changing lead-dot coupling	30
3.1	g-MCBJ fabrication overview	35
3.2	Gated-MCBJ fabrication	36
3.3	10X alignment and gate trenches	38
3.4	Photolithography	43
3.5	E-beam pattern	45
3.6	Dicing pattern	48
3.7	HF wet etch	50
3.8	Electromigration	53
3.9	Gated-nanotube-in-break-junction fabrication	54
3.10	Gated-nanotube-in-break-junction	58
3.11	Metallic nano-grains in g-MCBJs	60
4.1	Gated-MCBJ technique	64
4.2	4-Kelvin fridge	65
4.3	4-Kelvin mechanical assembly	67
4.4	Mechanical motion calibration (4K fridge)	70
4.5	Mechanical stability	72
4.6	Variable temperature (1.5-300K) assembly	75
4.7	Mechanical motion calibration (VTI fridge)	76
4.8	Electronics used for measuring g-MCBJ samples	78
5.1	Cartoons of our devices	83
5.2	Conductance versus V and V_g	85
5.3	$I - V$ characteristics	87
5.4	Capacitances versus displacement	89
5.5	Gate voltage degeneracy point	91
5.6	Mechanically controlled transistor action	93
6.1	Kondo assisted tunneling	96
6.2	Mechanical tuning of the Kondo resonance	98

6.3	Magnetic field dependence of the Kondo resonance	100
6.4	Temperature dependence of the Kondo resonance	101
6.5	Vibrational modes in C_{60}	103
6.6	Carbon nanotube g-MCBJs	104
6.7	Carbon nanotube tuning	105
6.8	Metallic particles in g-MCBJs	107
7.1	Stencil mask lithography	110
7.2	E-beam lithography on AFM tips	113
7.3	Other SPM tips fabrication methods	115
7.4	The vacuum chamber	118
7.5	AFM used to do stencil lithography on tips	120
7.6	Vibration isolation	121
7.7	AFM assembly	124
7.8	AFM scanning tube and sample holder	126
7.9	Resonance of a tuning fork	128
7.10	Mounting an AFM tip on a tuning fork	131
7.11	AFM Electronics Overview	132
7.12	Approach and tuning fork control software	134
7.13	AFM scans	136
8.1	Commercial AFM tip	139
8.2	Stencil fabrication steps	141
8.3	Photolithography mask used for fabricating stencils	143
8.4	Stencil masks	145
8.5	E-beam lithography on stencils	147
8.6	Stencil mask inspection	150
8.7	AFM tip inspection	153
8.8	Evaporation pin hole alignment	155
8.9	Lithography on AFM tips	161
8.10	Magnetic film characterization	164
8.11	Magnetic force microscopy with our sensors	166
8.12	Making macroscopic electrodes on AFM tips	170
8.13	Electrodes on an AFM tip	171
8.14	Gated-STM tip	173
8.15	New AFM design	176

Chapter 1

Introduction

In this chapter we review some work in recent literature to motivate and provide background for the work to be presented in the following chapters.

1.1 Perspective

Our society has been transformed by the advent of microfabrication of electronic circuits. More generally, the capability to control matter at the micron and nanometer scale has enabled great advances in the natural sciences, engineering and medicine. Still, most scientists would agree that our capability to build and organize nanometer-sized objects in three dimensions is very limited.

Clearly we have much to learn from nature about manufacturing three dimensional machines with atomic precision. Figure 1.1 shows an example of nature's work, a molecular motor (Myosin V) [1], made up of a few hundred atoms, which can walk along actin filaments inside human cells and deliver "cargos" to different parts of the cells. Each part of the motor has sophisticated capabilities that rely on a combination of physical and chemical properties. Such a machinery is far more advanced than what our technology will allow us to fabricate in the foreseeable future. To further develop our fabrication capabilities at the nanoscale we must first learn a lot more about the physical interactions that take place between nanoscale objects.

This thesis presents the development of two original techniques to probe nanoscale objects and their interactions. The first and main part (chapters 2-6) of this thesis is concerned with studying electronic transport in single organic molecules, and

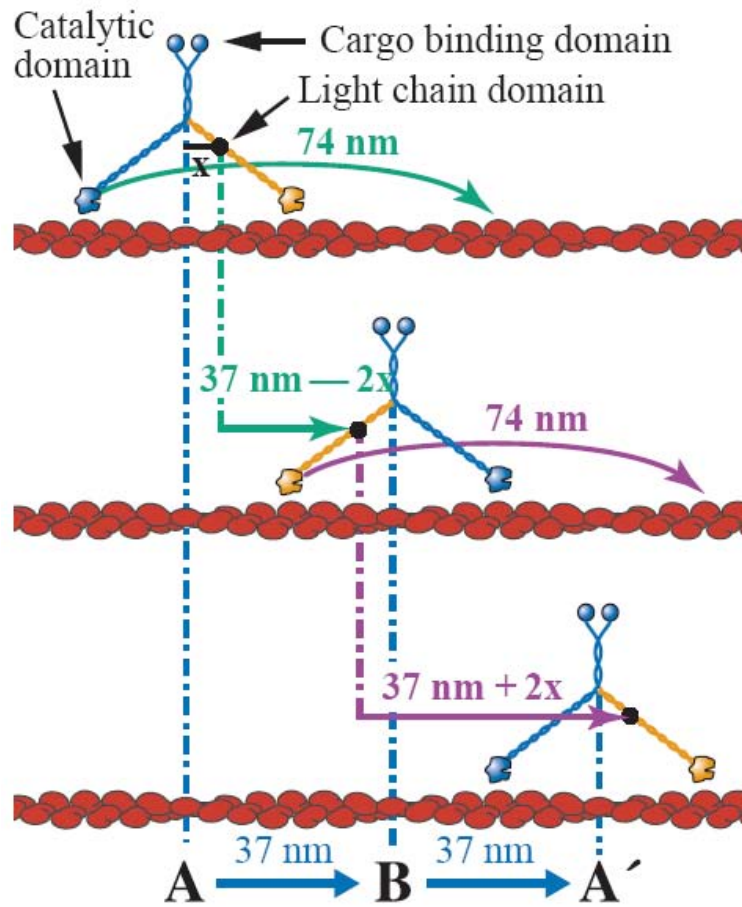


Figure 1.1: [Molecular motor] Cartoon of a myosin V molecular motor walking on an actin filament (from [1]).

is an extension of previous work [2]. The second part (chapters 7-8), describes the fabrication of advanced scanning sensors which can be used to probe in three dimensions the physical properties of nanoscale objects on a surface.

The work to be presented is also motivated by physics itself. While the field of condensed matter physics is now mature, numerous questions remain about physics at the nanoscale. For instance, the control and transport of electronic spin in nanosystems [3] is a relatively young field of research, and correlated electronic states still pose many interesting questions [4, 5, 6]. While this thesis does not address directly such problems (except section 6.1), the techniques developed here were designed in part to be able to address some of these questions. Figure 1.2 (a) (from ref. [7]) shows an example of how a scanning probe can be used to study correlated electrons. Specifically, a scanning single-electron sensor is used to probe localized electron states in a quantum Hall liquid. Panels (b) and (c) of Fig. 1.2 show data from a single-molecule transistor which was used by reference [8] to study the Kondo effect (a correlated electronic state) in the presence of ferromagnetism.

1.2 Single-molecule electronics

Organic molecules are “quantum boxes” that can be engineered with atomic precision by chemists. For this reason studying single organic molecules opens up lots of interesting experimental tests of quantum mechanics. [2, 8, 9, 10, 11, 12]

On the technological side, large scale molecular electronic devices have been successfully built and commercialized [13]. Molecular electronics presents a wide range of useful features for nanofabrication: the small size of its components (single molecules), possible self-assembly (low fabrication cost), and functional elements

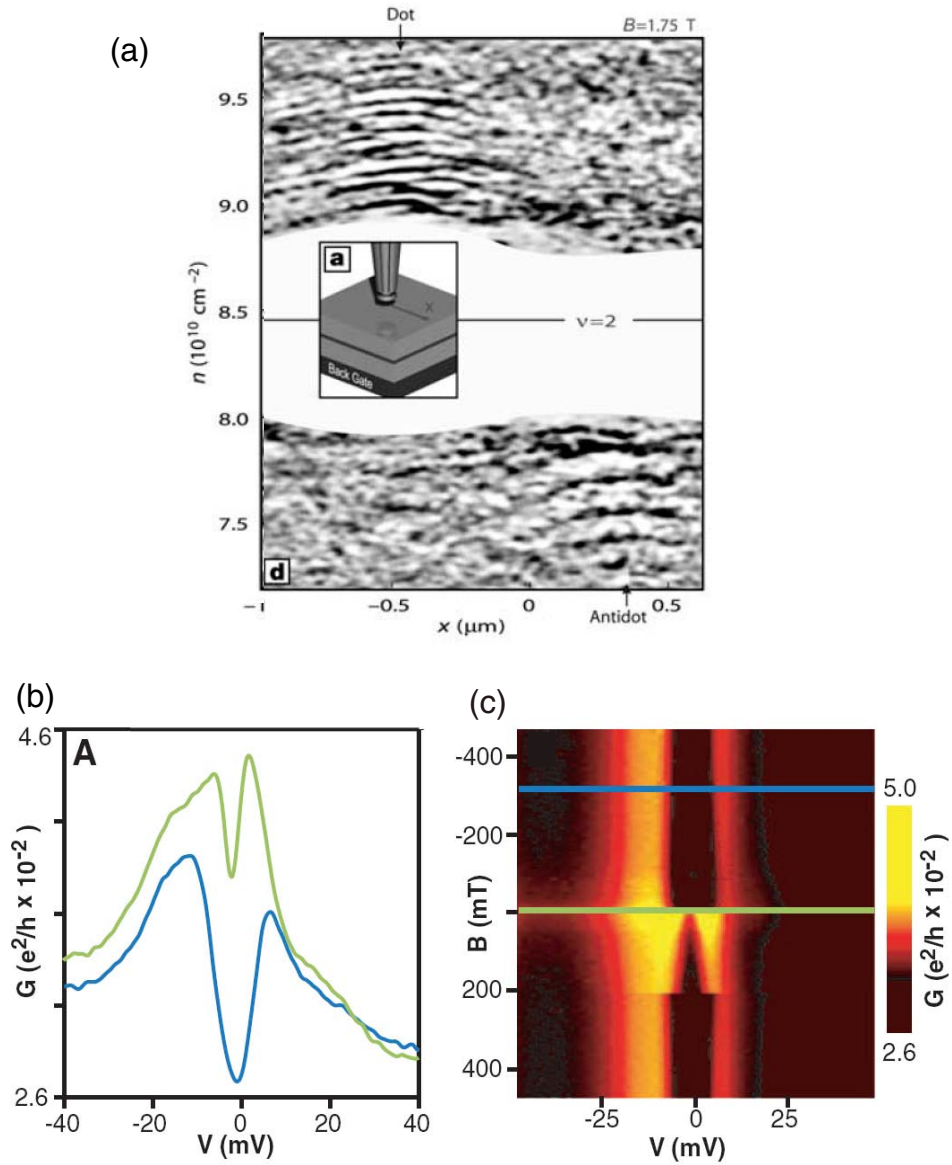


Figure 1.2: [Probing correlated electrons] (a) (Taken from [7]) Scanning single-electron transistor 1-d scan versus electron density in a 2-dimensional electron gas. The stripes visible in the image represent localized electronic states. (b) and (c) (taken from [8]) Conductance through a single C_{60} molecule as a function of bias voltage and magnetic field. The two peaks in conductance arise from the Kondo resonance splitting due to its interaction with the ferromagnetic electrodes.

(chemistry) [14]. One of the dreams of molecular electronics is to be able to fabricate useful devices whose active element consists of a single organic molecule (see Fig. 1.3 [15]). These devices have proven difficult to fabricate because they cannot rely on a statistical average of molecular properties, but instead demand a precise control of the environment of a single molecule. In order to develop single-molecule devices, more must be learned about how they are influenced by their environment (metallic electrodes, charge traps, neighboring molecules, etc ...) [14].

To both study fundamental physics and further the development of devices, it is desirable to make electrical contacts to single molecules in a controlled and “tunable” environment. Because of the small scale of organic molecules (≈ 1 nm), this is a very challenging task. Two separate strategies have been employed to systematically adjust a molecular device *in situ*. Electrostatic gating permits control of electron transport through a molecule by shifting its energy levels [2]. Mechanical adjustability, using scanning probes or mechanically-controlled break junctions, enables manipulation of the device structure and the strength of bonding to electrodes [16, 17, 11]. We briefly review both types of experiments. In chapters 3-6 we will discuss how we have combined both techniques into a single one, enabling more controlled and systematic experiments.

1.2.1 Electrostatically controlled single-molecule junctions

The lower inset of Fig. 1.4 (a) shows a cartoon of a single-molecule transistor, which consists of an organic molecule attached to source and drain electrodes and a nearby gate electrode that can electrostatically shift the energy levels inside the molecule (all the data shown in Fig. 1.4 was taken from [10]). The upper inset of Fig. 1.4 (a) shows a narrow gold wire used to make such a device. The wire

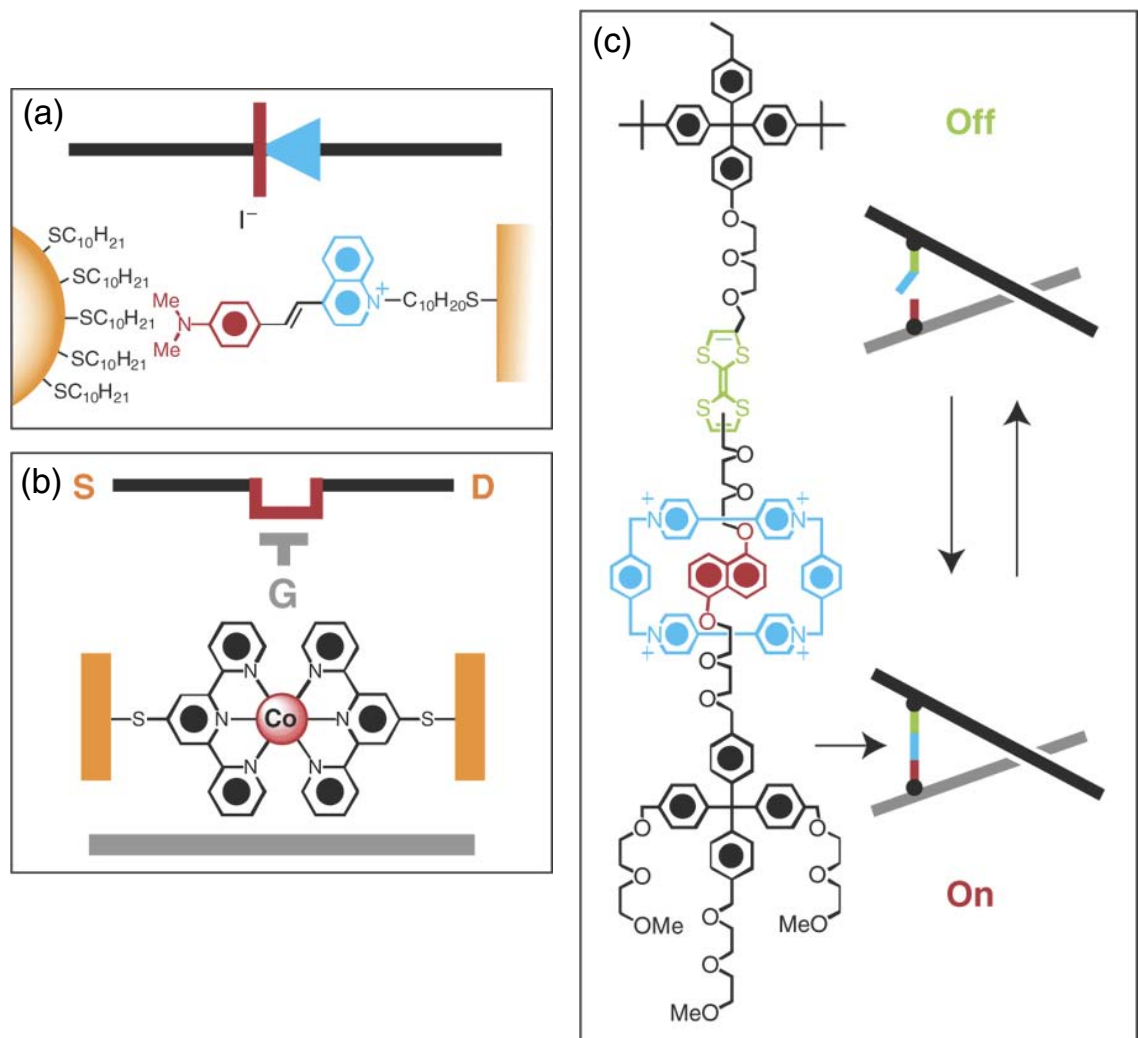


Figure 1.3: [Single-molecule electronic devices] (Taken from [15]) (a) A molecular rectifier. (b) A single molecule transistor. (c) A molecular switch.

is deposited on top of a gate electrode (protected by an insulating layer), and the molecules of interest are deposited on the Au wire. The device is then cooled down to liquid helium temperature (4.2 K). A large current is sent through the Au wire until it fails and a small gap (≈ 1 nm) in the Au line is opened. If the concentration of molecules is adjusted properly, a single molecule can be trapped in the gap and then be studied by monitoring the current flowing through it as a function of bias and gate voltage.

Figure 1.4 (a) shows a typical $I - V$ characteristic recorded on such devices at low temperature ($T < 4.2$ K). The region of zero current is known as the Coulomb blockade, and is due to the large charging energy ($E_c > 100$ meV) associated with adding an electron onto a small object (molecule)

$$E_c = \frac{e^2}{2C_\Sigma} \quad (1.1)$$

where e is the electron charge and C_Σ is the total capacitance of the molecule. The onset of current flow is seen as a step in the $I - V$ curve and corresponds to an energy level inside the molecule lining up with the Fermi level of the leads. Because of the charging energy, only one electron at a time can flow through the molecule. It can be shown [18] that the maximum conduction through one such conduction channel is the quantum of conductance $G_o = 2e^2/h$. Figure 1.4 (b) shows a two dimensional plot of conductance (dI/dV) versus bias and gate voltage. The dark regions on the left and right correspond to the Coulomb blockade region where essentially no current flows, while bright lines indicate the opening of a conduction channel. We see that the gate voltage can be used to tune the size of the blockade down to zero. At this point, the ground states with N and $N+1$ electrons are degenerate. The extra lines running parallel to the Coulomb blockade edges are associated with excited states of the molecules (vibrational levels). From

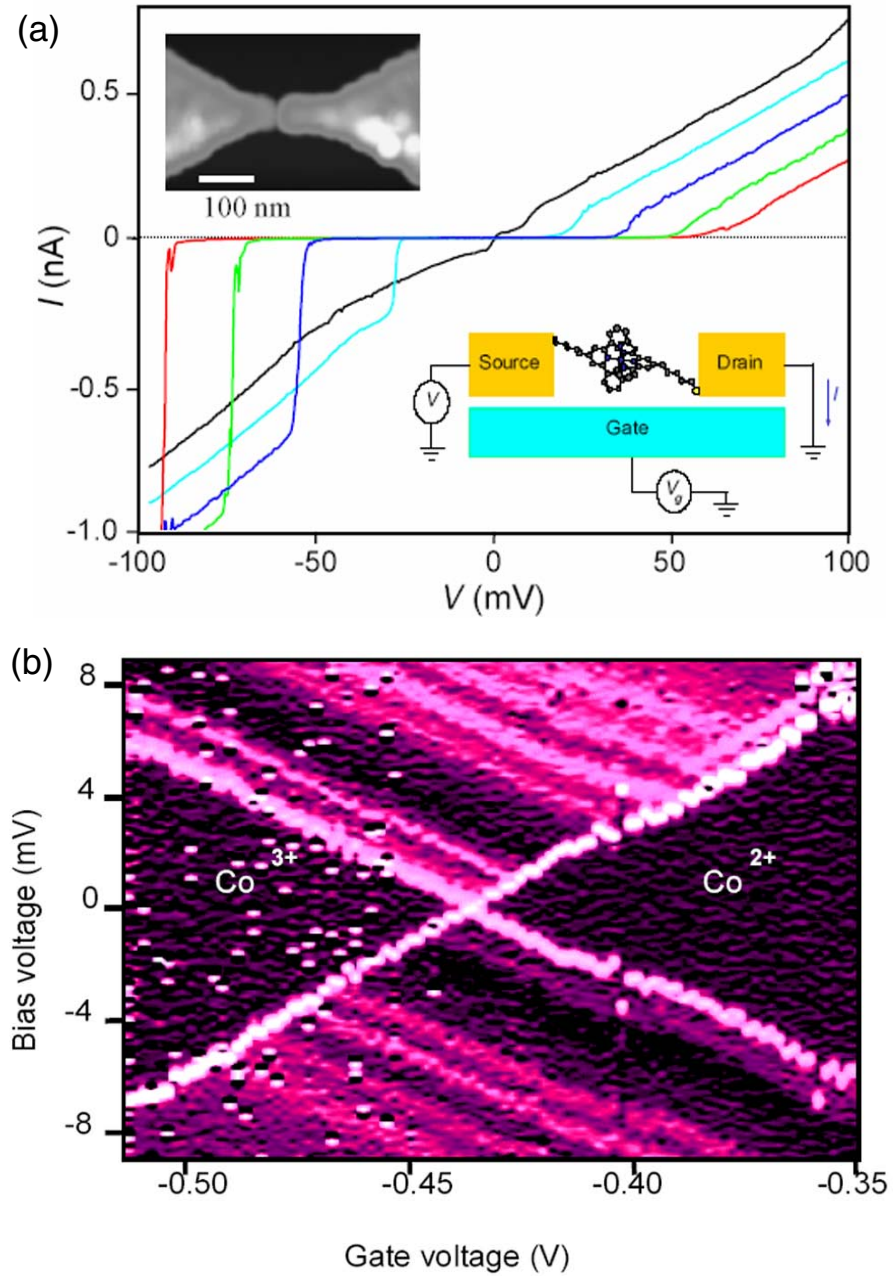


Figure 1.4: [Electromigration break-junction] (Taken from [10]) (a) $I - V$ characteristics for a single $[\text{Co}(\text{tpy}-(\text{CH}_2)_5\text{-SH})_2]^{2+}$ molecule transistor. (b) A two dimensional dI/dV color plot versus bias and gate voltage.

plots like the one in Fig. 1.4 (b), and using other knobs like magnetic field and temperature, it is possible to learn about the interactions inside the molecule and the interactions between the molecule and the electrodes. More details on transport in single-molecules will be given in chapter 2.

1.2.2 Mechanically controlled single-molecule junctions

Another method to study molecular junctions is to do away with the gate electrode, but instead allow the source and drain electrodes to move with respect to each other. The advantage of this method is that it can tune between different transport regimes where the molecule is either strongly or weakly coupled to the electrodes. There are different approaches to implement a mechanical degree of freedom in a molecular junction. The most ubiquitous are: scanning probe microscopy (SPM) [17, 19] and mechanically controllable break-junctions (MCBJ) [16, 11, 12]. The work presented in this thesis makes use of the MCBJ technique. A MCBJ consists of a narrow bridge of metal suspended above a flexible substrate (see Fig. 1.5 (a)). By bending the substrate, one can break the bridge and then adjust the spacing between the resulting electrodes. If the breaking is done in the presence of molecules, then one or a few molecules can be incorporated in the junction [12]. The power of the technique resides in the fact that the motion between the electrodes can be tuned with sub-angstrom accuracy since the displacement of the electrodes is greatly reduced from the amount of motion used to bend the substrate (see chapter 4).

Figure 1.5 (b) presents data from [12] where the conductance through a Au constriction is monitored while it is slowly broken. As the wire breaks, the number of conduction channels through it is reduced and leads to steps in the conductance.

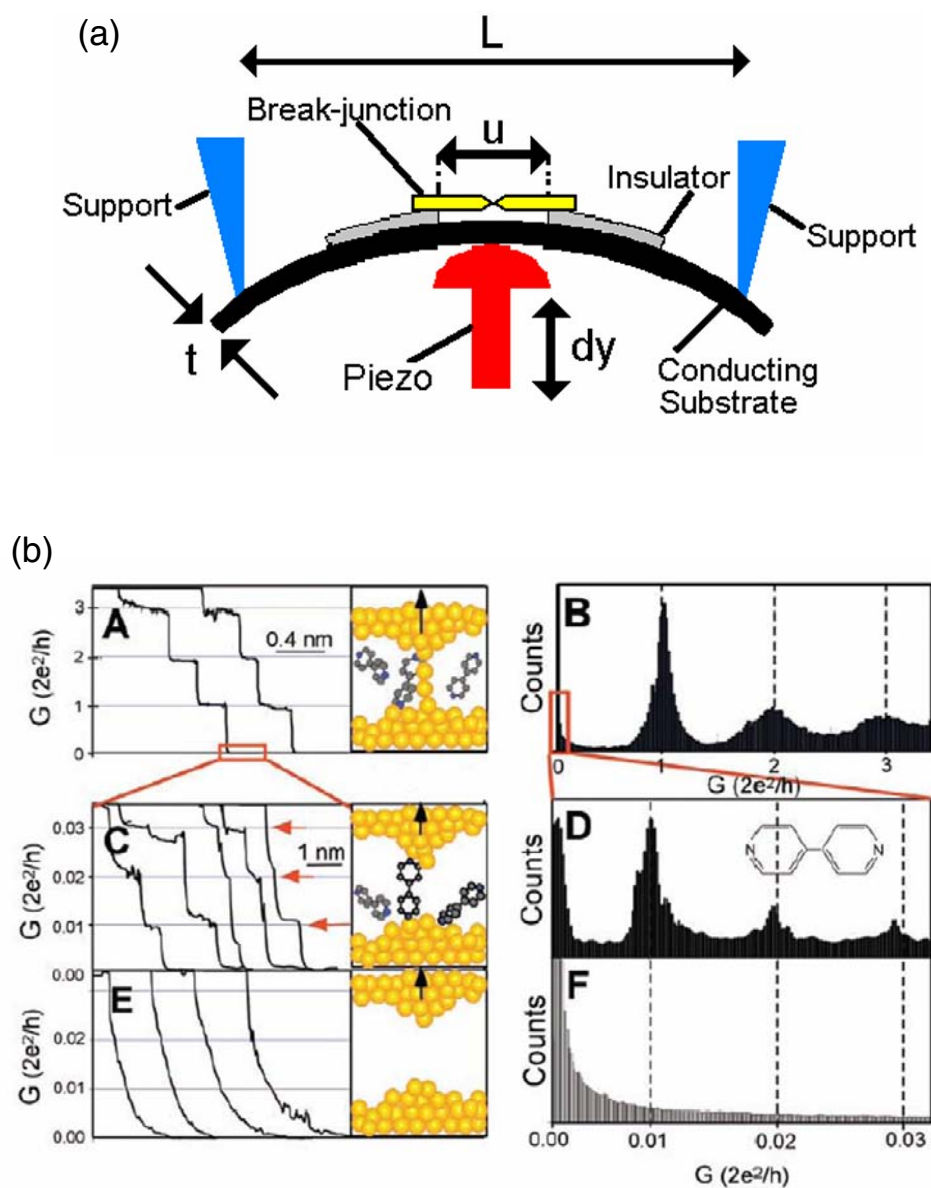


Figure 1.5: [Mechanically controllable break-junction] (a) A schematic of a mechanically controllable break-junction (MCBJ) assembly. (b) (taken from [12]) Left-hand side, conductance versus electrode displacement. Right-hand side, histograms of many conductance plots showing the quantization of conductance.

Even below one quantum of conductance (G_o), which corresponds to a one Au atom-wide bridge, smaller steps in conductance are observed when molecules are present in the environment. These smaller steps are associated with a decreasing number of molecules bridging the junction. By building histograms of these steps, the conductance through one and a few molecules can be inferred.

1.3 High-resolution scanning probe microscopy

Scanning probe microscopy (SPM) [20] is generally based on the atomic force microscope (AFM). An AFM consists of a sharp tip mounted at the end of a cantilever beam with a sharply resonant vibration mode. When scanning the tip above a surface, any interaction between the tip and surface will modify the resonance frequency of the cantilever beam. Therefore, by monitoring the frequency (or amplitude) of the beam as the tip is scanned, it is possible to form a two dimensional map of the the tip-surface interactions. Furthermore, if a feedback system is implemented, which maintains a constant cantilever resonant frequency by changing the tip-surface distance, a three dimensional image can be acquired. Figure 1.6 (a) shows a practical implementation of an AFM, the inset shows a tip (the apex has a radius of curvature ≈ 20 nm). An AFM relies on the van der Waals interaction (see Fig. 1.6 (b)) to image a surface, and can achieve atomic resolution (see Fig. 1.6 (c)).

It is possible to modify an AFM tip to probe other quantities besides the van der Waals force. For instance a magnetic coating [23], a gate electrode [24] or a single-electron transistor [25] can be added to the tip to image respectively magnetic forces, the response to a changing electrostatic potential, or variations in charge and potential on a surface.

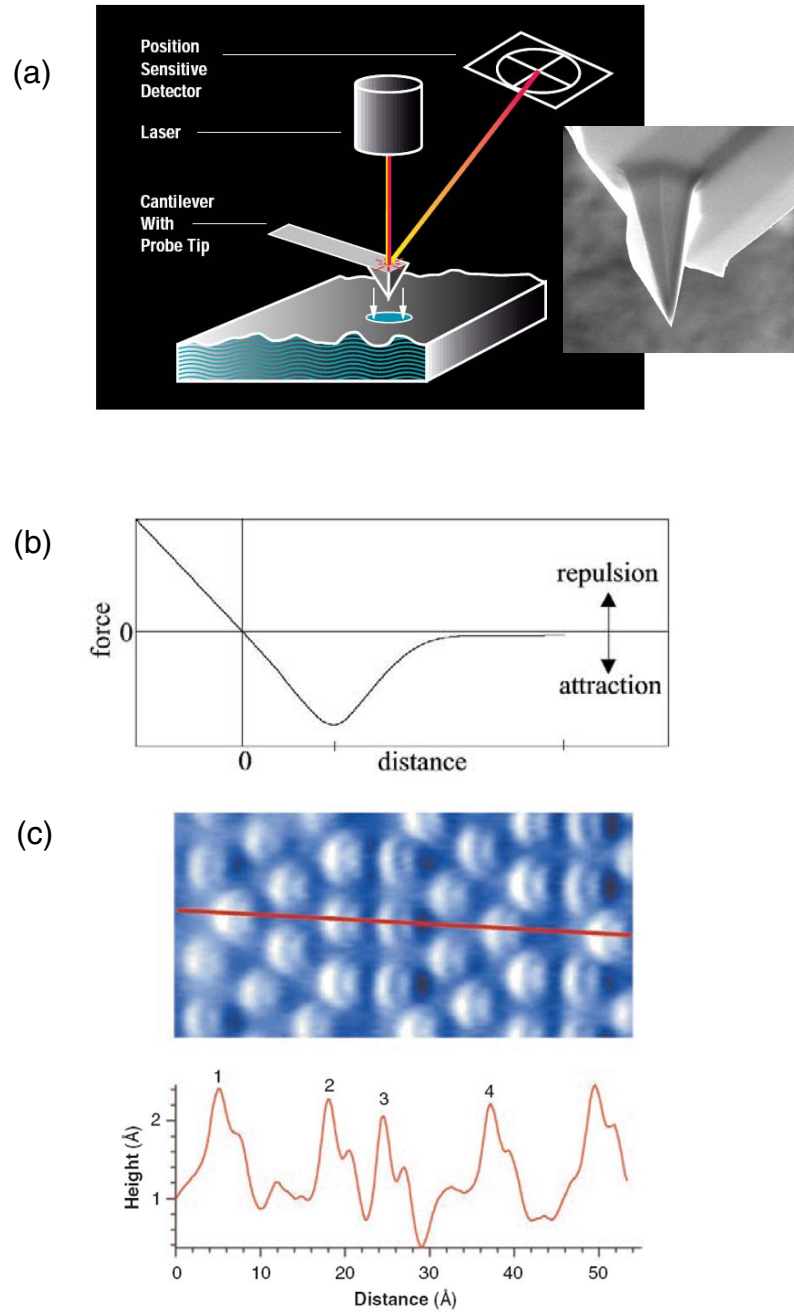


Figure 1.6: [Atomic Force Microscopy] (a) (taken from [21]) Atomic force microscopy. The inset show an AFM tip, the tip is about $10 \mu\text{m}$ tall and its apex has a radius of curvature $\approx 20 \text{ nm}$. (b) A plot of the potential energy between an AFM tip and surface. (c) (taken from [22]) An AFM image showing atomic resolution on a silicon surface.

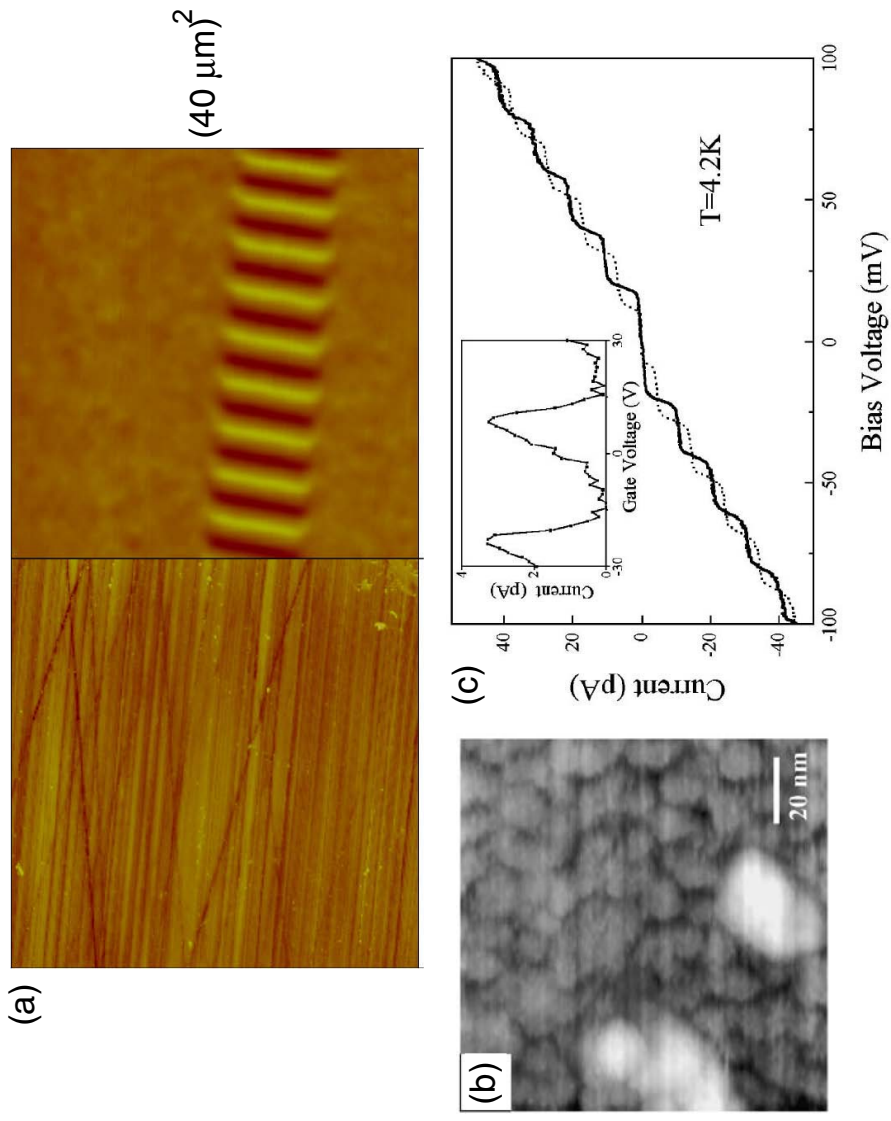


Figure 1.7: [Scanning Probe Microscopy] (a) (taken from [21]) Topographic (left) and magnetic force (right) images of a recording tape, $(40\mu\text{m})^2$. (b) and (c) (taken from [24]) A gated-STM image of Au cluster on a Pt film, and gate voltage controlled Coulomb staircase inside one Au cluster.

Figure 1.7 (a) shows an example of a magnetic force microscopy (MFM) scan. The left hand side shows a topographical image acquired by monitoring the van der Waals interaction between the tip and surface, while the right hand side shows a map of the tip-surface magnetic interaction. To separate the two interactions is relatively easy. At first the tip is scanned in close proximity to the surface (where van der Waals force is much larger than magnetic dipole-dipole force) to acquire a topographical image. Another scan is then performed, but at a larger distance (usually 10s of nanometers) and following the topography just acquired so as to maintain a constant tip-sample distance. Any force then measured by a frequency shift in the cantilever is ascribed to magnetic interaction, which decay as $(distance)^{-4}$ as opposed to $(distance)^{-6}$ for van der Waals.

Figure 1.7 (b) shows a scanning tunneling microscopy (STM) image of Au cluster on a Pt film. A STM does not monitor forces between the tip and surface, but rather how much tunneling current flows between the two. The inset of Fig. 1.7 (c) shows how adding an extra gate electrode to a STM tip enable it to measure Coulomb oscillations (change in the number of electrons) inside the Au particles. This technique, g-STM, makes it possible to study both the energy levels spectrum inside nanoscale objects and simultaneously image them in three dimensions. Details on the state-of-the-art fabrication techniques of advanced SPM probes will be given in chapters 7 and 8.

1.4 Organization of this thesis

In this chapter we have motivated the development of new techniques, and given background on some techniques previously used, to study electronic transport in single organic molecules and develop advanced forms of scanning probe microscopy.

In this thesis we will discuss how we have fabricated and measured single molecule devices that allow both electrostatic and mechanical control of the electronic transport. We will also describe a technique that was developed to fabricate high-resolution SPM probes that cannot be made by other currently available fabrication means.

Because research is by definition a collaborative effort, this thesis makes consistent use of the pronoun “we” when describing the work herein. Nevertheless, the work (nanofabrication, machining, instrumentation, software development, measurements, analysis, ...) presented in chapters 2-6 and 8 was done by the author himself (except when mentioned otherwise). The work in chapter 7 was an even collaboration between Aaron Couture and the author.

- Chapter 2 provides a brief theoretical background on transport in single-molecules (quantum dots) that can be both electrostatically gated and mechanically adjusted.
- Chapter 3 describes the fabrication of gated-mechanically adjustable break-junctions (g-MCBJs) to study single molecules.
- Chapter 4 discusses the measurement apparatus and technique developed to measure g-MCBJs.
- Chapter 5 presents results of transport measurements made on single C_{60} molecules in g-MCBJs.
- Chapter 6 summarizes a number of ongoing experiments using g-MCBJs to probe different transport regimes in single-molecules.

- Chapter 7 describes the design and fabrication of an atomic force microscope which can be used to fabricate high-resolution SPM sensors.
- Chapter 8 details the fabrication of high-resolution SPM probes, and their characterization.

BIBLIOGRAPHY

- [1] A. Yildiz et al., *Science* **300**, 2061 (2003).
- [2] A. N. Pasupathy, PhD thesis, Cornell University, 2004.
- [3] I. Zutic, J. Fabian, and S. Das Sarma, *Reviews of Modern Physics* **76**, 323 (2004).
- [4] O. Ujsaghy, G. Zarand, and A. Zawadowski, *Solid State Communications* **117**, 167 (2001).
- [5] S. Das Sarma and A. Pinczuk, *Perspectives in quantum Hall effects*, Wiley, 1997.
- [6] E. Dagotto, *Reviews of Modern Physics* **66**, 763 (1994).
- [7] S. Ilani et al., *Nature* **427**, 328 (2004).
- [8] A. N. Pasupathy et al., *Science* **306**, 86 (2004).
- [9] H. Park et al., *Nature* **407**, 57 (2000).
- [10] J. Park et al., *Nature* **417**, 722 (2002).
- [11] R. H. M. Smit et al., *Nature* **419**, 906 (2002).
- [12] B. Q. Xu, X. Y. Xiao, and N. J. Tao, *Journal of the American Chemical Society* **125**, 16164 (2003).
- [13] S. R. Forrest, *Nature* **428**, 911 (2004).
- [14] J. R. Heath and M. A. Ratner, *Physics Today* **56**, 43 (2003).
- [15] A. H. Flood, J. F. Stoddart, D. W. Steuerman, and J. R. Heath, *Science* **306**, 2055 (2004).
- [16] M. A. Reed, C. Zhou, C. J. Muller, T. P. Burgin, and J. M. Tour, *Science* **278**, 252 (1997).
- [17] B. C. Stipe, M. A. Rezaei, and W. Ho, *Science* **280**, 1732 (1998).
- [18] S. Datta, *Electronic transport in mesoscopic systems*, Cambridge, 1997.
- [19] X. D. Cui et al., *Science* **294**, 571 (2001).
- [20] R. Wiesendanger, *Scanning Probe Microscopy and Spectroscopy*, Cambridge, 1994.
- [21] Veeco Instruments, <http://www.veeco.com>.

- [22] F. J. Giessibl, S. Hembacher, H. Bielefeldt, and J. Mannhart, *Science* **289**, 422 (2000).
- [23] U. Hartmann, *Annual Review of Materials Science* **29**, 53 (1999).
- [24] L. Gurevich, L. Canali, and L. P. Kouwenhoven, *Applied Physics Letters* **76**, 384 (2000).
- [25] M. J. Yoo et al., *Science* **276**, 579 (1997).

Chapter 2

Coulomb blockade in a mechanically-adjustable transistor

In this chapter we give a brief introduction to the Coulomb blockade theory in the context of a single-molecule quantum dot. We comment on single-electron tunneling, resolving the excitation spectrum, and the effect of tuning the coupling to the leads in a single-molecule transistor. A more extensive review of Coulomb blockade and spectroscopy in quantum dots can be found elsewhere [1, 2, 3].

Figure 2.1 shows a schematic of a single-molecule transistor. For the purpose of this chapter we will refer to it as a single-electron transistor (SET). If it is energetically forbidden to change the number of electrons on the molecule (because of the charging energy), the only first order process by which current can flow through the device is for electrons to tunnel directly from the source electrode to the drain electrode. This is the so called Coulomb blockade. In this case, the molecule only acts as a “spacer” that determines the thickness of the tunneling barrier. The tunnel current decays exponentially with distance (see section 4.2.3), and is generally very small in the devices we measure. When a sufficiently large bias voltage is applied across the molecule, electrons are allowed to hop on and off the molecule one at the time (changing the number of electrons on the molecule by two would cost even more energy). Here we discuss how information about the molecule’s electronic states can be extracted by monitoring the current flow through the molecule in the SET regime.

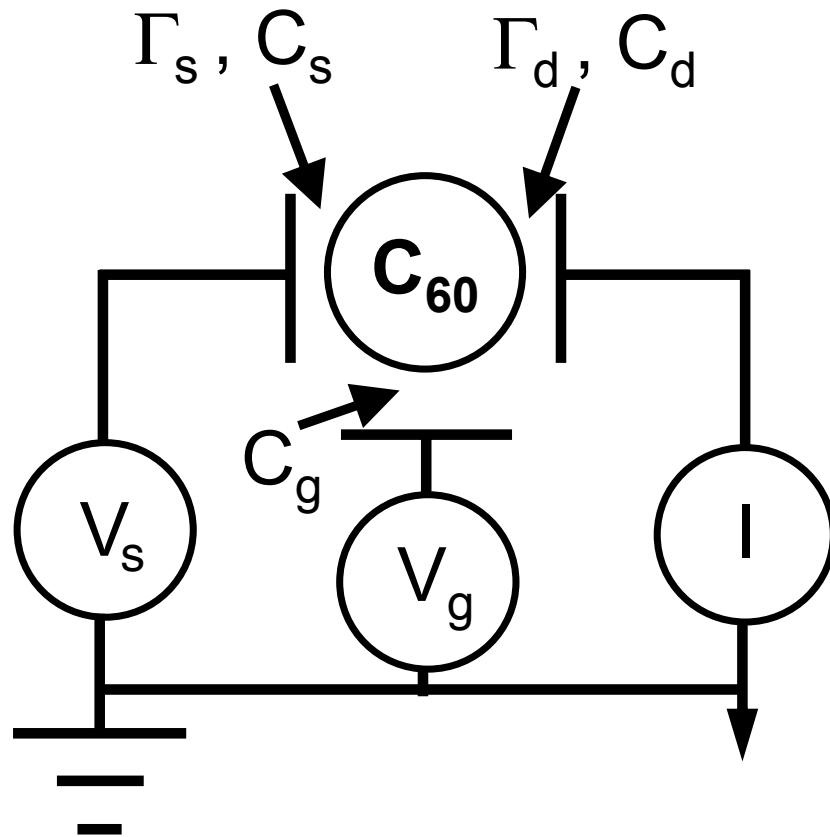


Figure 2.1: [Circuit diagram of a single-molecule transistor] Schematic of the electrical circuit of a molecular single-electron transistor.

2.1 Single-electron tunneling

2.1.1 Charging energy

We discussed briefly in chapter 1 how the current across a SET is blocked at low bias voltage due to the charging energy associated with adding an electron on the molecule. To find out what is the charging energy of the molecule in Fig. 2.1, we must first derive what is the electrostatic potential (V) at the molecule. Using the parameters from Fig. 2.1 we have

$$Q = C_s(V - V_s) + C_d(V - V_d) + C_g(V - V_g) \quad (2.1)$$

where Q is the total excess charge on the source, drain and gate capacitors, $C_{s,d,g}$ are respectively the source, drain and gate capacitances, and $V_{s,d,g}$ are the potentials on the source, drain and gate electrodes. From Eqn. 2.1 we obtain,

$$V = \frac{Q_o + ne + C_s V_s + C_d V_d + C_g V_g}{C_\Sigma} \quad (2.2)$$

where $C_\Sigma = C_s + C_d + C_g$, and $Q_o + ne = Q$, n is the integer number of excess electrons on the molecule, and e the electron charge. The charge Q_o is referred to as an offset charge, and is determined by the charge defects in the environment of the molecule. The value of Q_o will typically remain constant during our measurements as long as none of the background charges move. From now on we set $V_d = 0$, as is done in our experiments. The charging energy $\Delta U_{n \rightarrow n+1}$ of the molecule is now calculated by integrating the amount of work done while changing the charge from $Q_o + ne$ to $Q_o + (n + 1)e$,

$$\Delta U_{n \rightarrow n+1} = \int_0^e V dq = e \left(\frac{C_s}{C_\Sigma} V_s + \frac{C_g}{C_\Sigma} V_g \right) + \frac{e^2}{C_\Sigma} \left(\frac{Q_o}{e} + \left(n + \frac{1}{2} \right) \right) \quad (2.3)$$

Note that $\Delta U_{n \rightarrow n+1} = E_C = \frac{e^2}{2C_\Sigma}$ as mentioned in chapter 1 if $V_s = V_g = 0$, $Q_o = 0$ and $n = 0$. Proceeding as above, we find

$$\Delta U_{n \rightarrow n-1} = -e \left(\frac{C_s}{C_\Sigma} V_s + \frac{C_g}{C_\Sigma} V_g \right) - \frac{e^2}{C_\Sigma} \left(\frac{Q_o}{e} + \left(n - \frac{1}{2} \right) \right) \quad (2.4)$$

is the change in the energy on the molecule due to removing one electron.

2.1.2 Tunneling thresholds

As we saw in Fig. 1.4 (b), the current flow through the molecule is turned on at a bias voltage (V_s) threshold which is linearly dependent on the gate voltage (V_g). We will now derive the equations relating the V_s threshold to V_g . The results are plotted in Fig. 2.2 (a), where the solid lines represent the threshold between the blockade and SET regimes. The diamonds labeled “N-1”, “N” and “N+1” represent the blockaded ground states of the molecule with N-1, N and N+1 electrons.

Figure 2.2 (b) shows a cartoon of the molecule deep in the Coulomb blockade regime, where the next available energy level on the molecule is far above the Fermi level of the leads. The four possible biasing configurations for when an energy level on the molecule aligns with the Fermi level of one of the leads are shown in Fig. 2.2 (c). These four thresholds are labeled $V_{s,d}^\pm$ depending on whether the electron tunnels on (+) or off (-) the molecule from the source (s) or drain (d) electrode. The condition for V_s^+ is

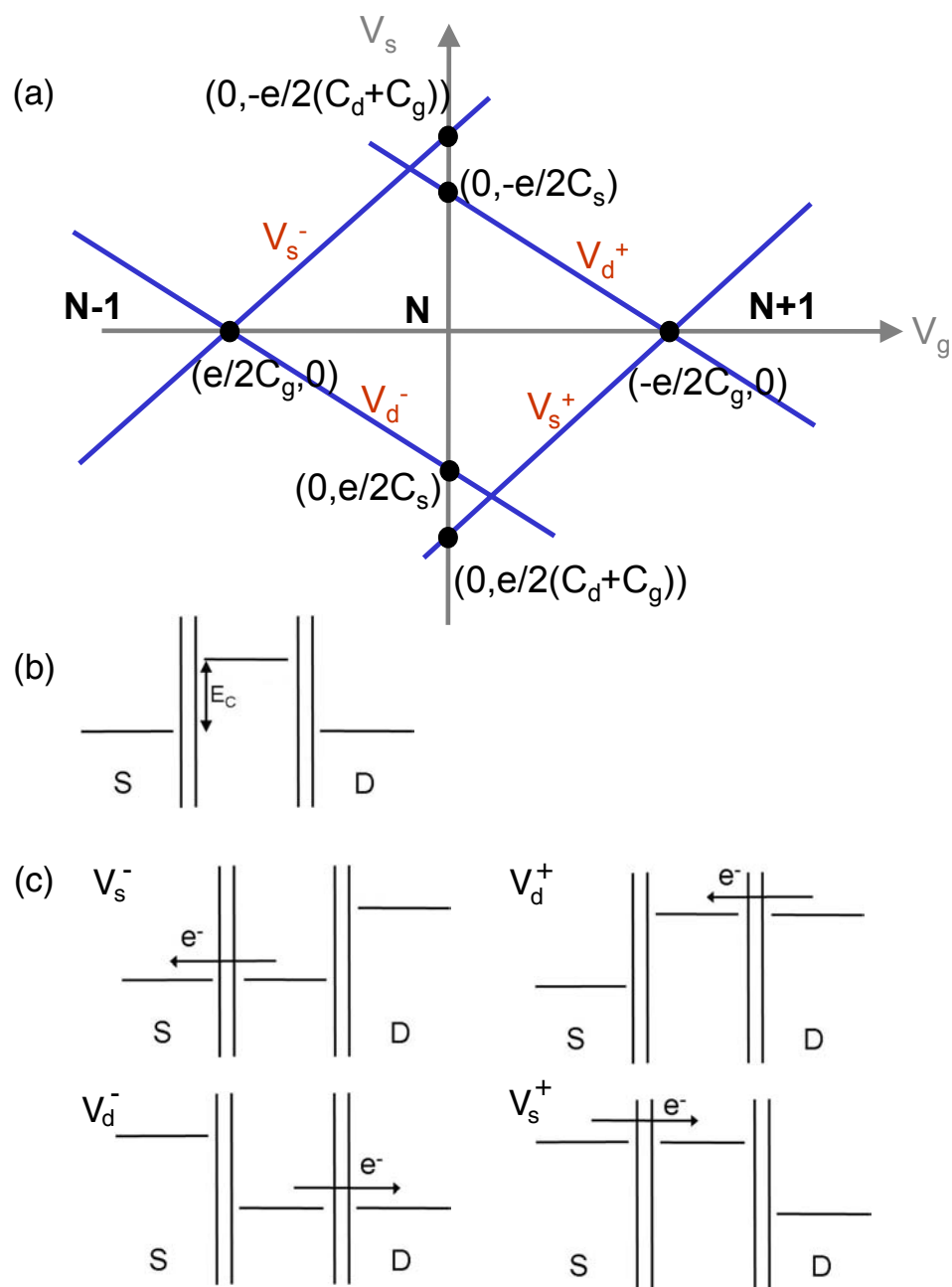


Figure 2.2: [Coulomb blockade diamond] (a) Plot of the Coulomb tunneling threshold (peaks in dI/dV) versus bias voltage (V_s) and gate voltage (V_g). (b) Band alignment between a molecule's lowest unoccupied energy level (LUMO) and the Fermi level of the leads inside the Coulomb blockade. (c) Band alignment between the molecule and leads at the Coulomb thresholds.

$$\Delta E_s^+ = E_{final} - E_{initial} = \Delta U_{n \rightarrow n+1} - eV_s^+ = 0. \quad (2.5)$$

Using Eqn. 2.3 we obtain,

$$V_s^+ = \frac{e}{(C_d + C_g)} \left[\frac{Q_o + C_g V_g}{e} + \left(n + \frac{1}{2}\right) \right]. \quad (2.6)$$

Similarly we obtain the other threshold voltages,

$$V_s^- = \frac{e}{(C_d + C_g)} \left[\frac{Q_o + C_g V_g}{e} + \left(n - \frac{1}{2}\right) \right] \quad (2.7)$$

$$V_d^+ = \frac{-e}{C_s} \left[\frac{Q_o + C_g V_g}{e} + \left(n + \frac{1}{2}\right) \right] \quad (2.8)$$

$$V_d^- = \frac{-e}{C_s} \left[\frac{Q_o + C_g V_g}{e} + \left(n - \frac{1}{2}\right) \right] \quad (2.9)$$

If we now set (for simplicity) $Q_o = 0$, we can use the above four equations to draw Fig. 2.2 (a). We use Fig. 2.2 (a) to extract important parameters of the device. The width of the Coulomb diamond is clearly equal to e/C_g . If the device has symmetric tunnel junctions ($C_s = C_d \gg C_g$), then the height of the Coulomb diamond is equal to the charging energy E_C . Also, the slopes of the V_s^+ , V_s^- thresholds are equal to $(C_d + C_g)/C_g$, while the slopes of the V_d^+ , V_d^- thresholds are equal to $-C_s/C_g$. Therefore, if we experimentally measure Fig. 2.2 (a), we can extract the device parameters C_s , C_d , C_g .

In the experiments that will be discussed in this thesis, it is generally not possible to measure the entire Coulomb diamond, both because the charging energy is large and the gate coupling is weak. Nevertheless, by measuring the slope of

the tunneling thresholds, the capacitance ratios $(C_d + C_g)/C_g$ and C_s/C_g can be extracted.

2.1.3 Tunnel rates

By making use of Fermi's Golden Rule we find that the tunneling rates across the source-molecule and molecule-drain barriers are given by,

$$\Gamma_{s,d}^{\pm} = \frac{1}{R_{s,d}e^2} \left(\frac{-\Delta E_{s,d}^{\pm}}{1 - \exp(\Delta E_{s,d}^{\pm}/k_bT)} \right) \quad (2.10)$$

where $R_{s,d}$ is the tunneling resistance across the source-molecule or molecule-drain junction, and

$$\begin{aligned} \Delta E_s^+ &= \Delta U_{n \rightarrow n+1} - eV_s \\ \Delta E_s^- &= \Delta U_{n \rightarrow n-1} + eV_s \\ \Delta E_d^+ &= \Delta U_{n \rightarrow n+1} \\ \Delta E_d^- &= \Delta U_{n \rightarrow n-1} \end{aligned} \quad (2.11)$$

The total current across the molecule can then be calculated from

$$I(V_s) = e \sum_{n=-\infty}^{\infty} \sigma(n) \left[\Gamma_d^+(n) - \Gamma_d^-(n) \right] \quad (2.12)$$

where $\sigma(n)$ is the ensemble-averaged probability that the number of electron on the molecule is n . From this equation and taking into account that the net transition probability between two states is zero in the steady state, it is possible to numerically calculate the current across the molecule. This method will be used in section 2.3.

2.2 Electrostatic control: resolving excited energy levels

The previous section discussed the conditions under which electrons can flow through the ground state of the molecule. Figure 1.4 (b), shows that beyond the Coulomb threshold a number of extra peaks in conductance can be observed. These conductance peaks correspond to excited states of the molecule through which electrons can flow provided that they have enough energy. In organic molecules, low energy excited states are typically vibrational states [4]. Figure 2.3 (a) shows a cartoon of a Coulomb diamond plot for the case of a single excited state (one for each charge state). Figure 2.3 (b), describes the energy level alignment between the electrodes and the molecule at different locations in the Coulomb diamond plot.

From the diagrams in Fig. 2.3 (b), we understand why the excited-level transitions run parallel to the ground state transitions: they depend on the same C_s , C_d , C_g . Furthermore, by looking for instance at the two band diagrams “2” and “3”, we find that when these two transitions intersect (as they do in Fig. 2.3 (a)), the source-drain bias is exactly equal to the excited level’s energy δE^- . Therefore the energy of excited levels can be readily deduced from the conductance (dI/dV) versus V_s and V_g plot in Fig. 2.3 (a). We note that while the current flow through the molecule’s ground state is the same for both positive and negative bias (if we neglect the spin degree of freedom), it is not the case for excited states (see [4]). Indeed, in devices that have asymmetric junctions ($\Gamma_s \gg \Gamma_d$), the excited state lines can be completely suppressed for one bias sign.

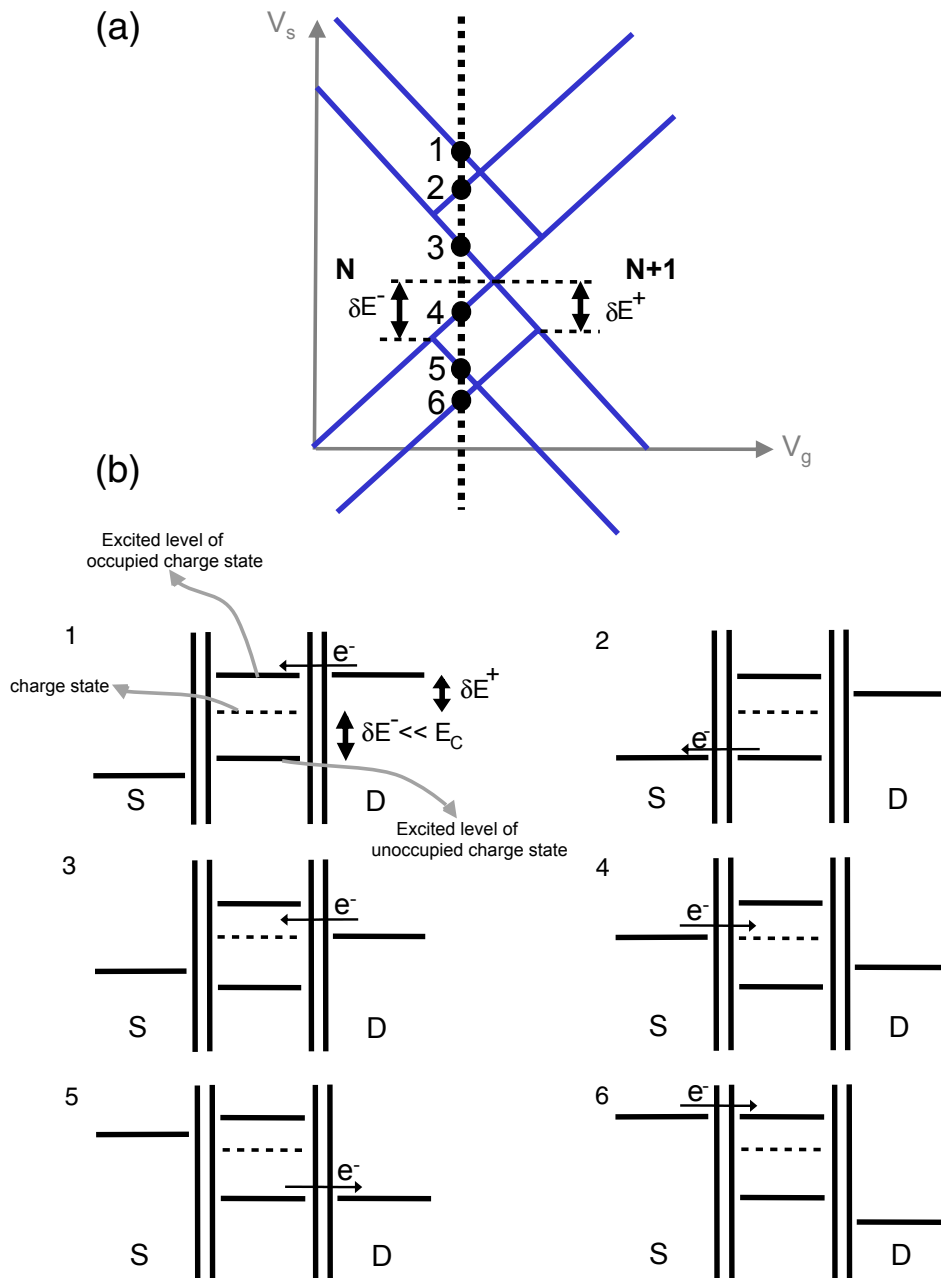


Figure 2.3: [Excited energy levels] (a) dI/dV versus V_s and V_g for a molecule with a single excited level. (b) Band alignment between the molecule's spectrum and the leads' Fermi levels at the points labeled on panel (a).

2.3 Mechanical control: changing the lead-molecule coupling

In the following chapters we will discuss single-molecule transistors where it is possible to mechanically tune the source-drain spacing. Here we discuss the effects, on the transport through the molecule, of changing the source-drain spacing in a SET.

The obvious effect of increasing the distance between the molecule and the leads (or at least the distance between the molecule and one of the leads) is to reduce the overall conductance of the device. This can readily be seen from Eqn. 2.10, since increasing the size of the tunnel junctions will increase their resistances R_s, R_d .

We also expect that increasing the width of the tunnel junctions should change the capacitances C_s, C_d . We detailed in section 2.1.2 how it is possible to measure the device's capacitances by measuring conductance versus bias and gate voltages.

Another effect of motion on transport has also been reported previously [5]. Since the work function ϕ of the metallic electrodes and the ionization energy of the molecule are unlikely to be equal, we expect a contact potential $\Delta\phi$ to form at the metal-molecule interface. As the source and drain electrodes are displaced, the capacitances between the leads and molecule change, and the amount of gating on the molecule from the contact potential will also change. Therefore we expect the source-drain displacement to act as a gate on the molecule, and the strength of the gating effect to depend on C_s, C_d and $\Delta\phi$.

Figure 2.4 (a) shows an $I - V$ characteristics measured in one of our single C₆₀ transistors, and an $I - V$ curve obtained from a numerical simulation based on

Eqns. 2.10 and 2.12. The simulation uses as parameters the capacitance ratios C_s/C_g , C_d/C_g and the junction’s overall resistance, which are measured experimentally (see section 2.1.2). The rest of the parameters in the simulation are adjusted to fit the experimental data. The simple code used is provided in Appendix A.

Figure 2.4 (b) shows the evolution of the derivative (dI/dV) of the data in panel (a) as a function of source-drain displacement. We see that the mechanical motion in this case causes changes reminiscent of a Coulomb diamond. Using our numerical simulation, we let the capacitances $C_{s,d}$ evolve linearly between their initial and final experimental values, and use $\Delta\phi$ as a fit parameter to obtain Fig. 2.4 (c). The curvature of the Coulomb threshold lines arises from the changing capacitance of the junctions, and the “mechanically controlled diamond” comes from the gating effect of the source-drain electrodes as they move away from the molecule. The details of the code are in Appendix A. To obtain Fig. 2.4 (c) we used $\Delta\phi = 27$ meV, which is consistent with experimentally measured values (see section 5.3.2).

Ultimately we are interested in studying more intricate effects of changing the molecule-lead coupling in a molecular transistor. For instance there are predictions on how the coupling to the vibrational levels of the molecule (electron-phonon coupling) behaves when the tunneling barrier size is modified [6, 7, 8]. As a simple example of how vibrational levels can be influenced by the leads’ motion, we can think of an organic molecule which is strongly bonded to the electrodes. As the electrodes are pulled apart we expect that the molecule will be stretched, and its vibrational modes will be shifted.

A well known many-body state of electrons, the Kondo effect, has been observed in single-molecule transistors [9, 10] and is known to depend very strongly on the

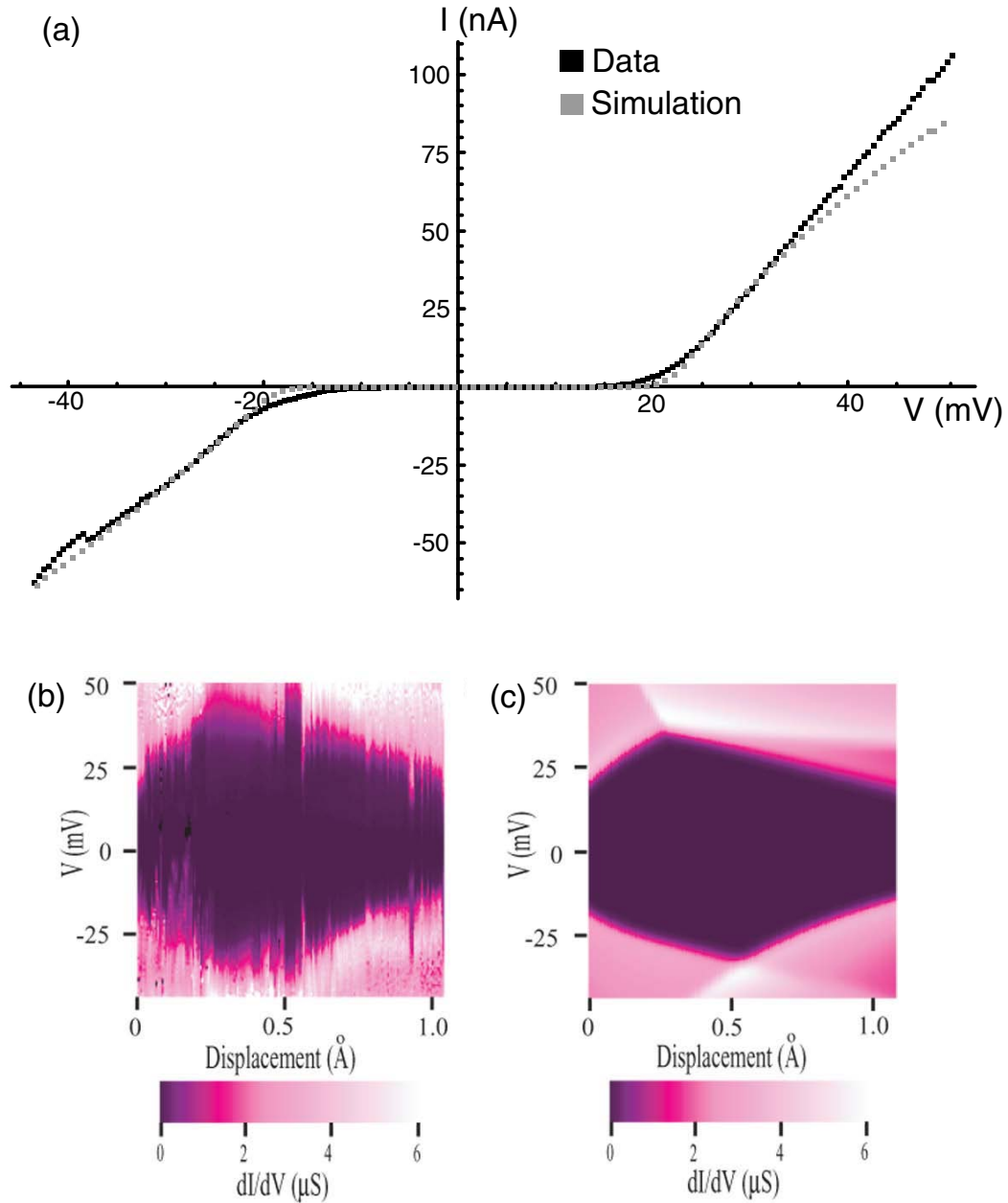


Figure 2.4: [Numerical simulation of changing lead-dot coupling] (a) $I - V$ characteristic from one of our C_{60} single-molecule transistors, and a numerical simulation of the same data. (b) dI/dV (color) versus bias voltage and mechanical displacement for the same sample as in (a). (c) A numerical simulation of (b), obtained with the orthodox Coulomb blockade theory, using parameters extracted from (b) and a fit of the parameter $\Delta\phi$.

coupling between the leads and the molecule. In this regime, it should therefore be possible to mechanically tune the amount of coherent electron flow through the molecule, from a many-body state to a single-electron tunneling picture. Early progress on experiments to probe effects of tuning the electrode-molecule coupling on a Kondo state and vibrational levels is described in chapter 6.

Other systems should also show changes in transport when tuning the source-drain spacing: for example, molecular transistors made with ferromagnetic or superconducting leads.

BIBLIOGRAPHY

- [1] C. T. Black, PhD thesis, Harvard University, 1996.
- [2] M. Tinkham, D. Davidovic, D. C. Ralph, and C. T. Black, *Journal of Low Temperature Physics* **118**, 271 (2000).
- [3] J. Park, PhD thesis, University of California, Berkeley, 2003.
- [4] A. N. Pasupathy, PhD thesis, Cornell University, 2004.
- [5] A. E. Hanna and M. Tinkham, *Physical Review B* **44**, 5919 (1991).
- [6] S. Braig and K. Flensberg, *Physical Review B* **68**, (2003).
- [7] S. Braig and K. Flensberg, *Physical Review B* **70**, (2004).
- [8] Z. Z. Chen, R. Lu, and B. F. Zhu, *Physical Review B* **71**, (2005).
- [9] J. Park et al., *Nature* **417**, 722 (2002).
- [10] W. J. Liang, M. P. Shores, M. Bockrath, J. R. Long, and H. Park, *Nature* **417**, 725 (2002).

Chapter 3

Fabrication of mechanically-adjustable single-molecule transistors

3.1 Introduction

One of the most critical parts of our experiments is fabricating high-quality devices which make electrical contact to single molecules. These devices should be tunable in as many ways as possible to allow us to study the nature of electronic transport in single molecules. Here we discuss a fabrication method to make single-molecule transistors equipped with a gate electrode and whose source-drain electrode spacing can be adjusted *in situ*. How these devices, electrostatically-gated-mechanically controllable break-junctions (g-MCBJ), are operated was briefly introduced in chapter 1 and will be discussed further in chapter 4.

The main challenge in making g-MCBJs is minimizing the molecule-gate spacing to enable useful gating. As our gate electrode, we use a degenerately-doped Si substrate, which allows us to employ standard lithographic techniques to produce a molecule-gate spacing as small as 40 nm, compared to 1 μm substrate spacing achieved previously with MCBJs on rougher metal or glass substrates [1].

The fabrication process described herein closely follows previous work done by Abhay Pasupathy [2] and Jiwoong Park [3]. A large number of small but significant changes were made to the previous fabrication recipe. For this reason and the sake of completeness, the fabrication process will be described in detail. The fabrication is done at the Cornell Nanofabrication Facility (CNF). Most of the devices I used

in my experiments were entirely fabricated in the older facility (Knight Lab), but all of the procedures described here can be done in the new clean room.

In section 3.2 we describe how to make gated-mechanically controllable break-junction (g-MCBI) devices used to study single organic molecules. Figure 3.1 shows an overview of the g-MCBI devices we fabricate. A large number of chips are defined on a 4-inch wafer. Each chip contains 36 devices, each of which consists of a large contact pad ($200\ \mu\text{m}$)² and a narrow (50 nm) Au-constriction suspended 40 nm above a conducting substrate. Section 3.3 discusses the electromigration process [4] used to wire up single molecules using the g-MCBI devices. We then discuss how to adapt the fabrication process to wire-up single carbon nanotubes (section 3.4) and metallic particles (section 3.5).

3.2 Silicon-back-gate devices

Our fabrication process begins with 200 μm thick 4-inch wafers polished on one side. The wafers are heavily doped so that they can be used as a back-gate and their resistivity is about $0.003\ \mu\Omega\cdot\text{cm}$. Figure 3.2 outlines the main fabrication steps to make g-MCBI devices.

3.2.1 Field oxide

The first step is the growth of a field oxide on our wafers which creates an insulating layer between the conducting wafer and the devices we will build on it.

The wafers (generally 25 of them) are MOS cleaned following the standard CNF procedure. The wafers are then loaded into the silicon oxide furnace. I use two dummy wafers at either ends of the wafer boat to help ensure a uniform oxide thickness over all the wafers. The growth is done at 1000 °C for 40 minutes. This

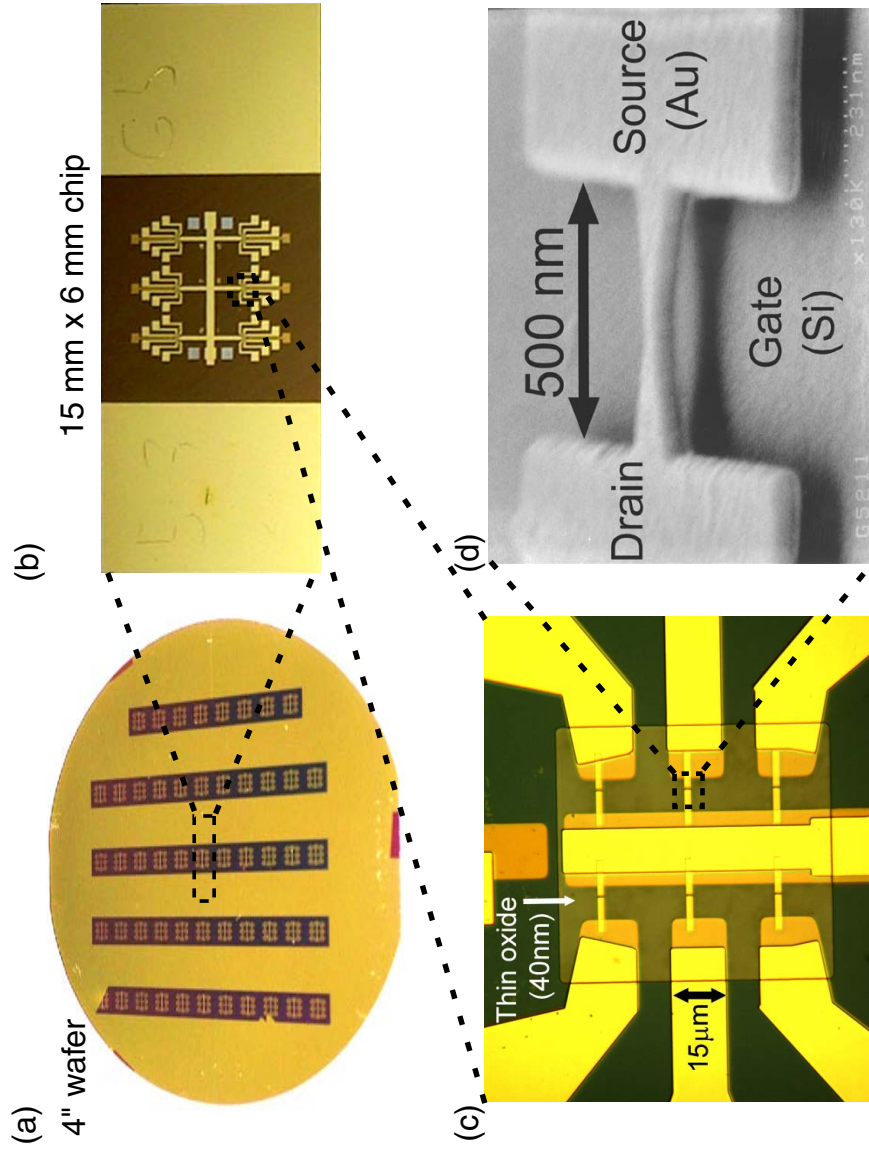


Figure 3.1: [g-MCBL fabrication overview] (a) A 4-inch wafer on which an array of g-MCBL chips were fabricated. (b) A single g-MCBL chip which contains 36 Au break-junction devices. (c) Optical zoom of the active region of six devices. (d) SEM image of a single break-junction suspended 40 nm above the Si substrate.

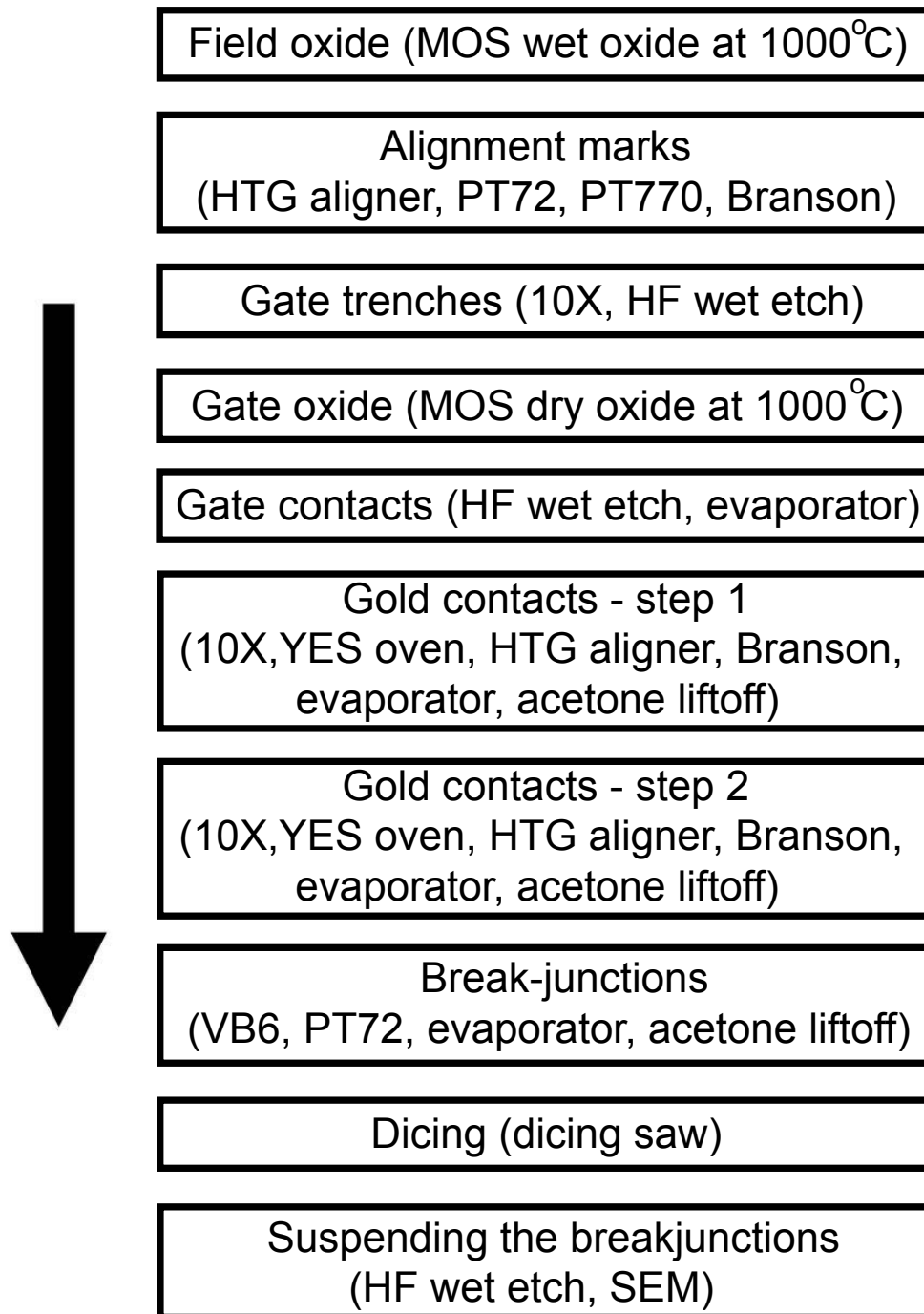


Figure 3.2: [Gated-MCBI fabrication] Flowchart for the fabrication of gated-MCBI devices.

gives about 300 nm of SiO₂, which is an appropriate thickness (less than 250 nm is not recommended). The film thickness is measured using the Leitz interferometer.

3.2.2 Photolithography and gate oxide

Stepper alignment marks

Next, we define alignment marks (GCA keys) to be used by the 10X stepper to align the different layers of photolithography. These marks are transferred onto the wafers by contact lithography using the HTG contact aligner. The mask used is shown in Fig. 3.3 (a), and was made using the GCA PG3600F pattern generator. The pattern transfer goes as follows:

1. Prime the wafers with P-20 at 4000 rpm for 30 seconds.
2. Spin Shipley-1813 resist at 3000 rpm for 60 seconds.
3. Bake at 115 °C for 60 seconds.
4. Expose with the HTG contact aligner for 6 seconds using the mask shown in Fig 3.3 (a).
5. Develop in MIF300 for about 70 seconds and rinse with DI water.
6. Etch the pattern into the oxide. First descum the resist with a 30 sec O₂ RIE. Then, etch the oxide film using any of the RIEs (Applied Materials, PT72 or Oxford80) using a CHF₃/O₂ gas. I usually etch two wafers at the time. Monitor the etch rate by measuring the film thickness of a dummy piece, and etch about twice as long as required to etch through the oxide film.

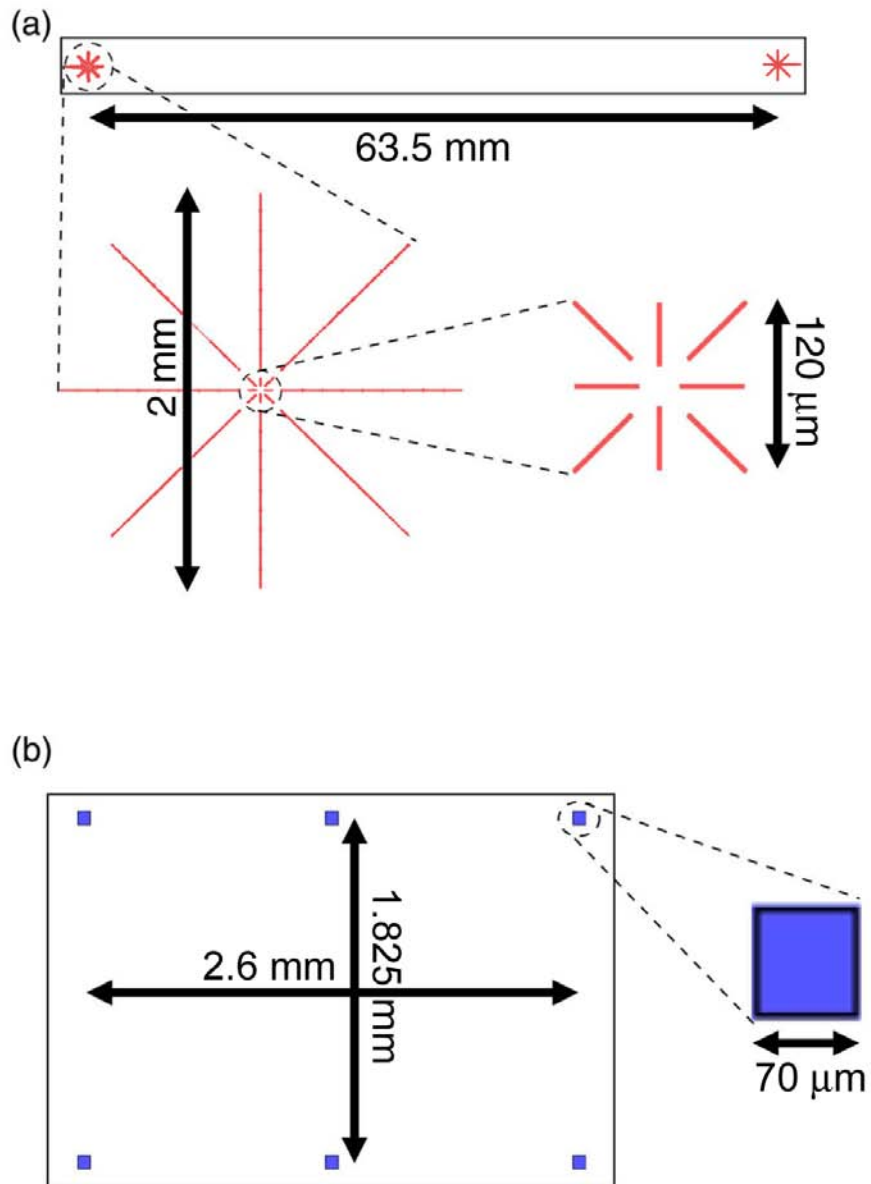


Figure 3.3: [10X alignment and gate trenches] (a) Contact lithography mask used to produce alignment marks (GCA keys) for the 10X stepper. (b) 10X stepper mask used to make gate trenches.

7. Etch the pattern into the silicon. To do this use the Unaxis770 or PT770 with the standard Si recipe for about 2 minutes.
8. Remove the resist with a 15 minutes ashing in the Branson barrel etcher. (200 μm -thick wafers can be damaged when used in the GaSonic etcher)

Gate trenches

We now make gate trenches where the field oxide thickness will be reduced and the break-junctions built. The purpose of these trenches is both to increase the gate-sample coupling by reducing their separation and to define the height at which the MCBJ devices will be suspended above the substrate once the gate oxide is etched. The pattern transfer is done with the 10X stepper and the mask shown in Fig. 3.3 (b). To create gate trenches, follow these steps:

1. Prime, spin and bake S1813 on the wafers as described above.
2. Expose the wafers on the 10X stepper using the mask in Fig. 3.3 (b). Align the wafer using the GCA keys with key offsets of $X = +1.75$, $Y = -9.0$. I expose an array of 5 columns by 12 rows of 15×6 mm dies. The exposure time is 2 seconds.
3. Hard bake the wafers for 60 seconds at 115 °C.
4. Develop in MIF300 for 60 seconds.
5. Descum wafers with a 20 seconds O_2 RIE etch.
6. Use a HF buffered oxide etchant (BOE) 6:1 to etch the silicon oxide in the trenches. Etch for 7.5 minutes (about twice what is needed). Rinse carefully (you will be playing with lots of HF).

7. Remove the resist with the Branson barrel etcher (or the GaSonics if you dare).

Gate oxide

The gate trenches are now completely free of all oxide. We shall now grow a thin (40 nm) high-quality dry oxide at the bottom of the gate trenches. This oxide will create the spacing between our devices and the backgate. We proceed like this:

1. MOS clean the wafers.
2. Grow roughly 40 nm of dry oxide at 1000°C. This takes about 25 minutes. Make sure to use two dummy wafers at both ends of the wafer boat. Also, load at least one dummy wafer with no prior oxide so that it can be used to measure the oxide thickness.
3. Etch away the oxide just grown in a “clean” 6:1 BOE bath. Over-etch by a factor of 1.5.
4. Grow the gate oxide again. You will need to do another MOS clean. This time use the calibration from the previous growth to grow exactly 40 nm. Make sure to include a dummy wafer with no oxide, to verify the thickness grown. The purpose of growing the oxide twice is to minimize the surface roughness of the oxide (seems to work). In the future an oxide thickness of less than 40 nm may be used to improve the gate coupling. My guess is that we can probably scale down our oxide thickness to 20 nm. Reducing it further would probably run into problems with the oxide roughness and the characterization procedure.

Gate contacts

We want to make ohmic contact to the gate electrode (Si substrate) without creating any leakage between the devices and the gate. To do this we fabricate 4 $(300\ \mu\text{m})^2$ platinum contacts that are directly in contact with the substrate and to which wirebonds can be made easily. The 10X mask used to transfer the pattern has only 4 squares on it, their location is shown in Fig. 3.4 (a) as the 4 large purple squares on the left and right sides of the chip design. We fabricate the gate contacts using the following steps:

1. Prime, spin and bake S1813 on the wafers as described above.
2. Develop for 60 seconds in MIF300.
3. Etch the SiO_2 either in an RIE (18 min / wafer in App. Mat. with 30 mTorr, 90 Watts and 30 sccm CHF_3) or with a BOE 6:1 wet etch (6 minutes).
4. If you used a wet etch, do a descum in the Branson barrel etcher for 1.5 minutes.
5. Use the Sharon evaporator to deposit 2 nm Ti/ 50 nm Pt on the wafers using the water cooled stage. The cooling is crucial to avoid hard baking the resist.
6. Liftoff in acetone. Use a syringe or squeeze bottle to stir the solution, and inspect under the microscope **before** drying the wafer.
7. Rapid thermal annealing is unnecessary since the heat from the evaporation suffices to create a platinum silicide. The result should give an ohmic contact between the gate-contact pads and Si wafer.

Contact pads and wiring

The bulk of the sample's metallization is done during this step. Here we create the contact pads to which wirebonds will be attached, and the wires that connect the pads to the break-junctions. Figure 3.4 shows the 10X mask used in this step (the gate contacts are shown in Fig. 3.4 (a) but are not on the mask used here).

To create the sample contacts and wiring we follow these steps:

1. Prime, spin and bake S1813 on the wafers as described above.
2. Using the 10X stepper expose the mask shown in Fig. 3.4 (a) with the same parameters we used for the gate trenches.
3. Image reverse the resist by baking the wafers in the YES ammonia oven.
4. Flood expose the wafers for 180 seconds using the HTG.
5. Develop the wafers for 1.75 minutes in MIF321.
6. Descum in the Branson barrel etcher for 1.5 minutes.
7. Evaporate 2 nm of Ti and 16 nm of Au using the Sharon evaporator.
8. Liftoff in acetone for a few hours.
9. Repeat the exact same process but now use a slightly different mask. The difference is shown in Fig. 3.4 (b). The new mask has shorter Au-leads in the trench region (darker color). The idea is that by exposing this mask, we can add more metal to the contact pads (reduce resistance), but at the same time avoid making thick Au-leads in the trench region (would prevent a smooth interconnect with the ebeam layer). This time deposit 2nm Ti and 100 nm of Au.

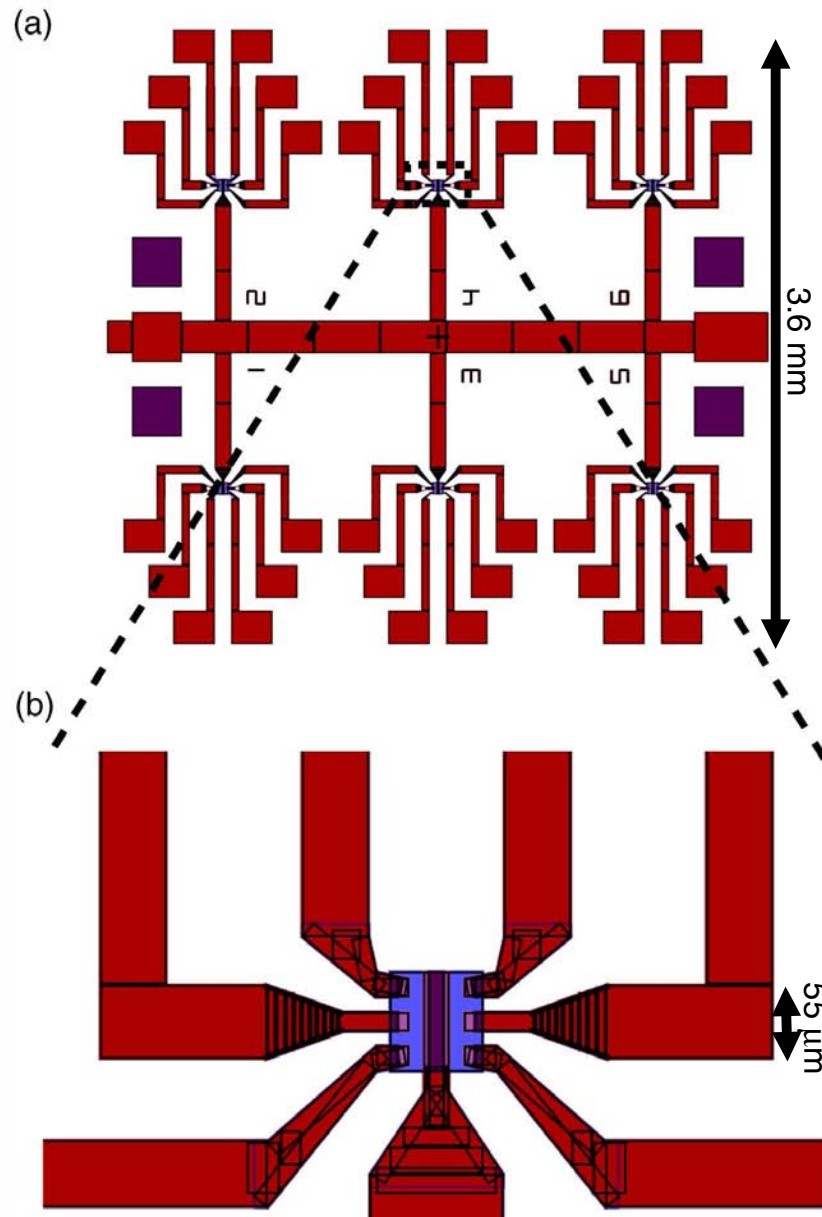


Figure 3.4: [Photolithography] (a) Photolithography pattern exposed using the 10X stepper. (b) Zoom of the photolithography around a gate trench. A first thin layer of lithography is used to define the end of the Au contacts that will connect to the e-beam lithography. A second layer is placed exactly on top of the first one, except for the last 10 μm of the contacts, to reduce the contact resistance.

The wafers are now ready for e-beam lithography.

3.2.3 Electron-beam lithography

The heart of our devices is the break-junctions themselves. These are fabricated by e-beam lithography on the Leica VB6 at CNF. Figure 3.5 (a) shows the location of the e-beam pattern with respect to the photolithography layers. Figure 3.5 (b) and (c) show the details of CAD pattern exposed with the VB6. Each junction has two connecting pads ($10\ \mu\text{m} \times 2\ \mu\text{m}$) that make contact to the photolithography, and a narrow bridge which will serve as a g-MCBI. The bridge is 500 nm long, has an initial width of 200 nm and shrinks down to a width of 50 nm at its center. These dimensions were optimized to facilitate the release of the bridge from the substrate with a HF etch. Many different geometries and materials were tried, but the best tradeoff between sturdiness, reproducibility, and range of mechanical motion was achieved with Au and the geometry shown in 3.5 (c). We will comment further on possible improvements for the breakjunctions' design in chapter 4.5.

The recipe given here aims at making wires with 50-nm-wide constrictions with a very high yield. The recipe could easily be refined to make narrower features, but this would also make it less robust. To fabricate nanowires which will be used as g-MCBI we follow these steps:

1. Clean the wafer with an oxygen plasma in the Branson barrel etcher for 1.5 minutes.
2. Spin 11 % PMMA/MAA copolymer (3:1 in ethyl lactate) at 3000 rpm for 60 seconds.
3. Bake for 15 minutes at 170 °C.

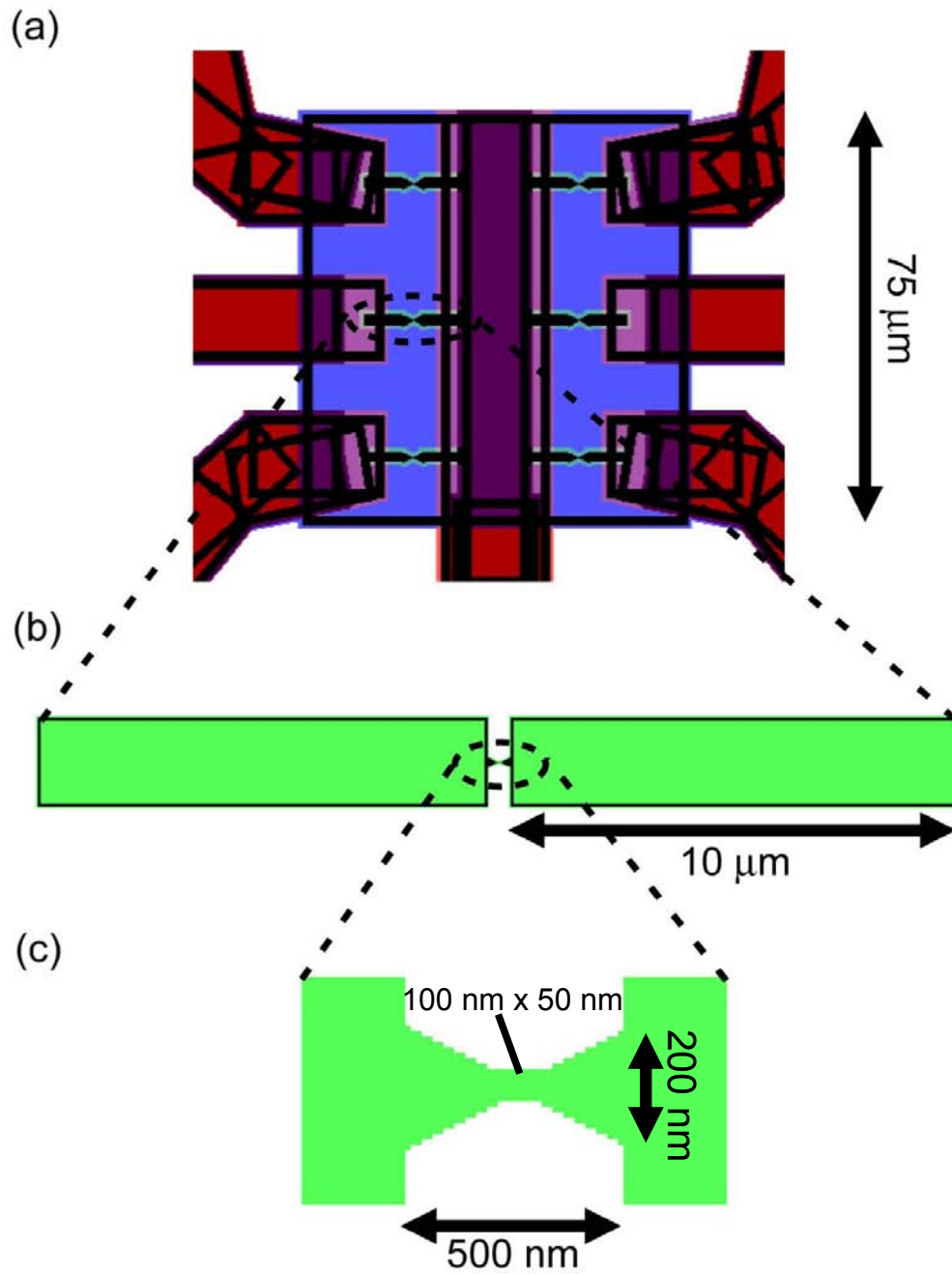


Figure 3.5: [E-beam pattern] (a) CAD drawing of the e-beam lithography for six devices. (b) Zoom of a single device's e-beam layer. (c) Zoom of the central constriction of the e-beam layer.

4. Spin 4 % 495K PMMA at 3000 rpm for 60 seconds.
5. Bake for 15 minutes at 170 °C.
6. Load your CAD pattern onto the VB6. The pattern I generally use can be found on the VB6 at VB.USERS.RALPH.ALEX.MBJ.FRE.P01M1L05_01.FRE.
7. Expose the wafer.
 - (a) Mount the wafer on the stage and measure the position of the # 1's on the dies at the four corners of the wafer.
 - (b) Set current to 1 nA, and run the calibration scripts.
 - (c) Define the coordinate system. To do this I run the scripts:
align_to_number_one.com, abs_to_die_align.com, and die_to_wafer.com,
which are located in VB.USERS.RALPH.ALEX.MBJ.18JUN03.
 - (d) Run the job file. I use
VB.USERS.RALPH.ALEX.MBJ.18JUN03.WAFER_X.COM.
8. Develop the wafer: 60 seconds in 1:3 MIBK:IPA, 15 seconds in methanol, 25 seconds in IPA.
9. Descum the wafer in the PT72 for 8 seconds. Clean thoroughly the RIE chamber before the descum.
10. Evaporate 32 nm of Au in Sharon. (no sticking layer is necessary, if needed use 2 nm of Ti)
11. Liftoff in 1:1 acetone:dichloromethane. Agitate, sonicate briefly (< 30 seconds), and inspect while still in the solvent.

3.2.4 Dicing, final wet oxide etch, and SEM imaging

Dicing

We are now done with the lithographic steps. Since we want to be able to process one or a few chips at a time from now on, we must dice the wafer into single chips. The dicing pattern is shown in Fig. 3.6, where the gray lines show the cuts to be made on the wafer. The dicing can be done in-house using the CNF dicer or you can send your wafers out to a dicing company [5]. In either case follow this procedure:

1. Prime the wafer with P-20. Spin S1818 at 2000 rpm for 60 seconds, and bake for 2 minutes at 115 °C.
2. Dice or send for dicing with a clear dicing pattern diagram like the one in Fig. 3.6. The dies are 15 mm × 6 mm.
3. Remove the dicing tape from the back of the wafer, and remove the photoresist with a long acetone soak and an O₂ RIE clean (60 seconds in App. Mat.). I leave the photoresist on until I actually want to use the chips, since the resist protects the chips against contamination.

Wet etch

To be able to mechanically tune the source-drain electrode distance of our break-junctions, we need the junctions to be suspended above the substrate. To achieve this we etch our chips in a 6:1 BOE (HF) solution for approximately 60-70 seconds. The exact etch time depends on many parameters, for instance the growth conditions of the SiO₂ and the amount of agitation during the etch. When the etch time is properly calibrated the result looks like Fig. 3.7 (a)-(b). There are three major

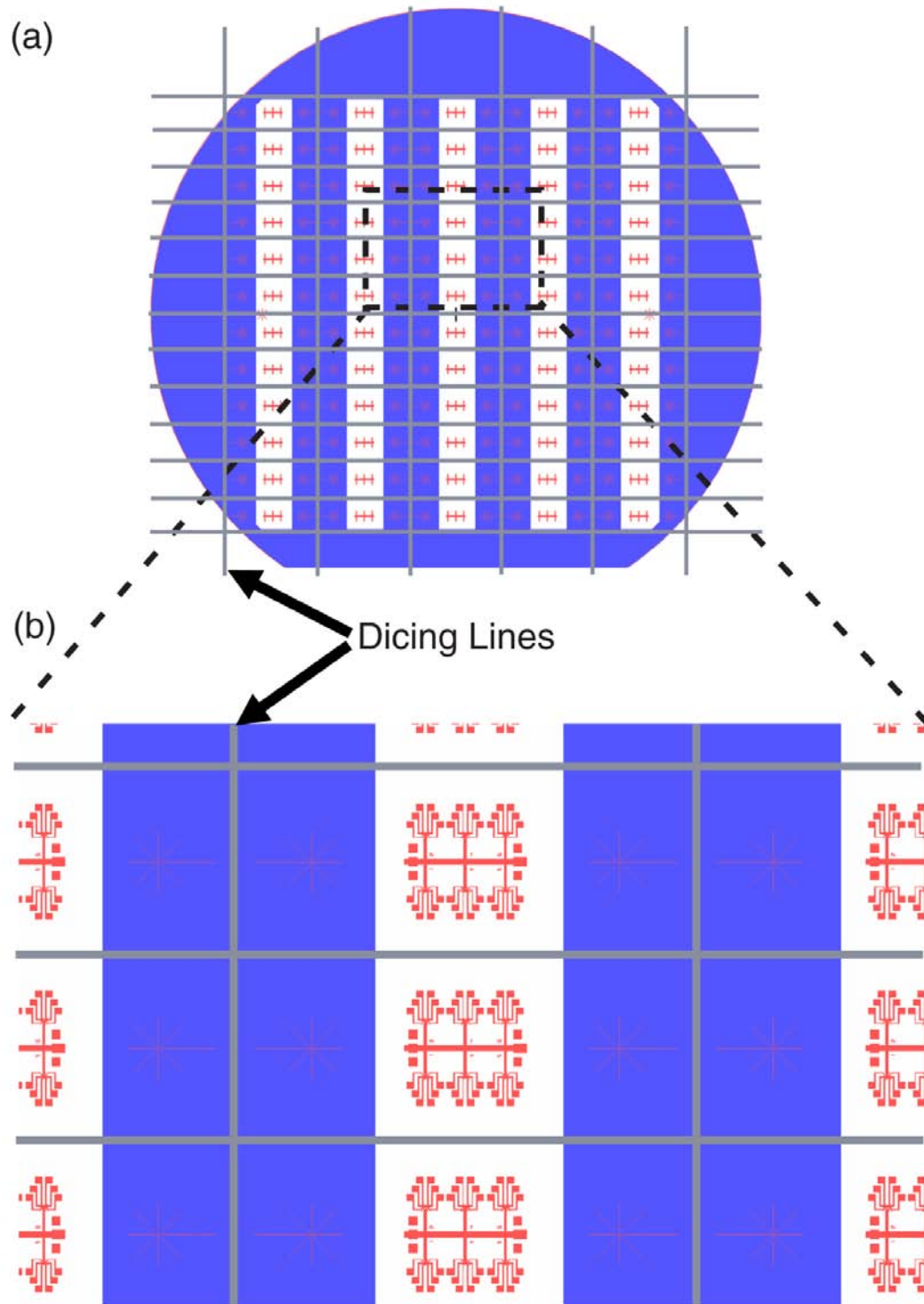


Figure 3.6: [Dicing pattern] (a) Dicing pattern for a 4-inch wafer of MCBJ chips.

(b) Close-up view.

attributes of a successful etch: there is no silicon oxide left under the bridge (not like Fig. 3.7 (c)), the bridge is straight and not collapsed (unlike Fig. 3.7 (d)), the wider part of the e-beam layer is not collapsed and touching the substrate (unlike Fig. 3.7 (e)).

Characterizing the suspended bridges is not easy. One check is to look for gate leakage. A large leakage indicates that the junctions are collapsed or that the edge of the e-beam contacts touch the backgate. Another check is to measure the resistance of the break-junctions. For our geometry, the resistance should be around 30Ω at room temperature. But for a detailed understanding of what has happened to our break-junction during the HF etch we must use SEM imaging. The next section discusses how the imaging is done.

SEM imaging

Imaging our g-MCBJ junctions is not straightforward because they are suspended only a very short distance (40 nm) away from the substrate. For this reason we need to image the junctions at a high tilt angle (usually 78°) to see under the Au bridge. Things are also complicated by the small contrast of SiO_2 on Si, which makes it difficult to tell whether or not all the SiO_2 was etched away.

By far the best microscope for this type of imaging is the Hitachi S4500 SEM available at the CIMC located in the Veterinary School. This microscope handles very well the necessary large astigmatism corrections needed for large tilt imaging. Furthermore, it is very reliable and easy to adjust. The standard imaging parameter are as follows: tilt = 78° , current = $10 \mu\text{A}$, voltage = 5 kV, detector = lower, aperture = 3. Normally, a good image (see Fig. 3.7 (b)) can be obtained in just a few minutes. With experience, the SEM can help to rapidly trouble shoot

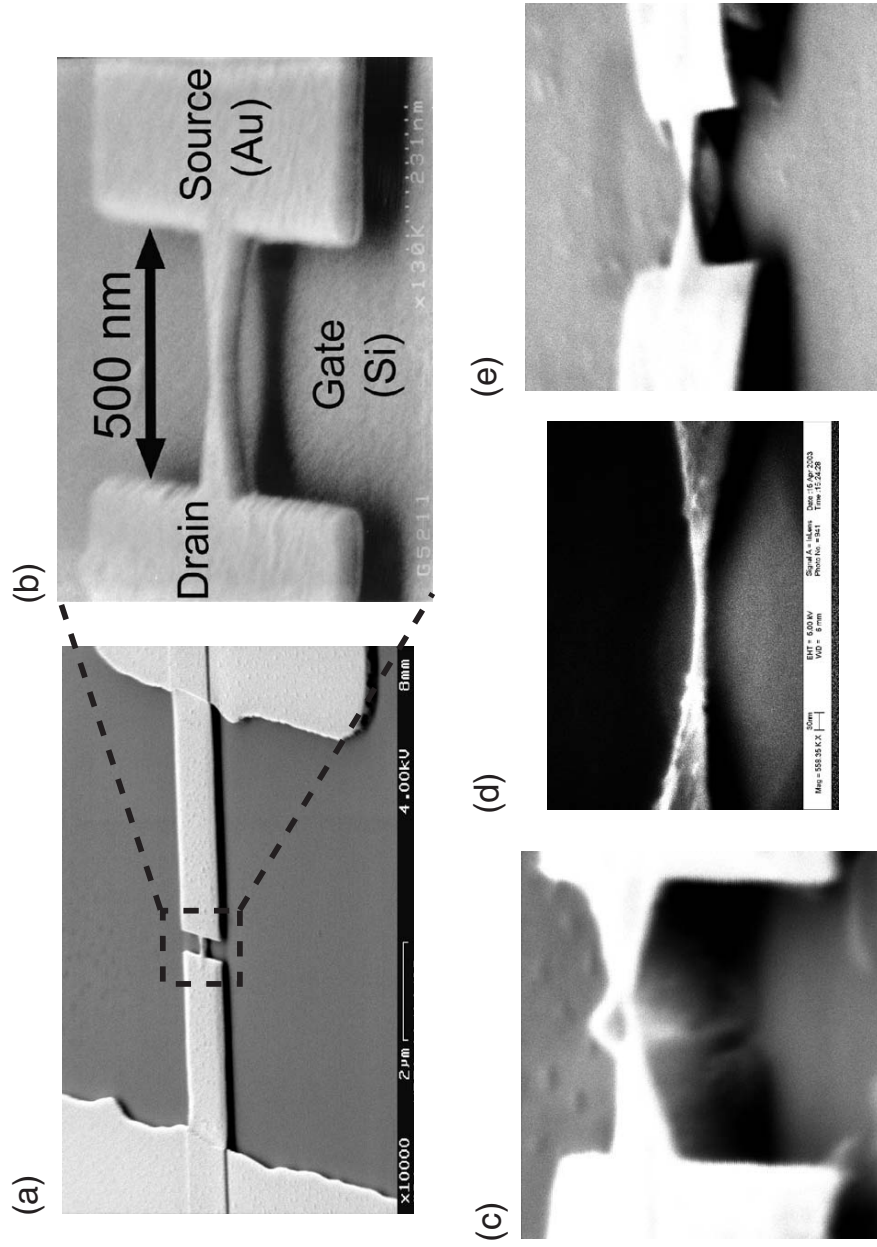


Figure 3.7: [HF wet etch] SEM images taken after the junction is released from the substrate via an HF etch. (a) The e-beam layer defining a junction and connecting it to the contacts defined by photolithography. (b) A suspended junction. (c) An under-etched junction. (d) A collapsed junction. (e) A junction where the Au contacts touch the backgate.

any problem with the e-beam lithography and final HF etch. Every time a new batch of chips is etched, one of them should be imaged. Doing otherwise would be foolhardy.

3.3 Electromigration

At last we are ready to create movable break-junctions and wire-up single molecules. To do this we need to break our suspended Au bridges so as to form two electrodes in close proximity. We will then be able to adjust the spacing between the two electrodes by bending the substrate on which the junctions are fabricated (see chapter 4). In non-gated MCBJ, the breaking of the junctions is done by bending the substrate until the metallic bridges fail [1]. For our g-MCBJ junctions this is not possible because our substrate (Si) is brittle and only allows a small amount of bending. Therefore we break our junctions using electromigration [4]. We ramp a DC voltage across a junction until the current flow causes the wire to fail and opens a ≈ 1 nm-size gap in the middle of the suspended Au-bridge. To achieve this gap size, appropriate for wiring-up a single molecule, the sample must be cooled down to liquid helium temperature. A lot of details about the electromigration technique can be found in Abhay Pasupathy's thesis [2]. Even though the chips were oxygen cleaned for 60 seconds prior to the last HF etch, they must be cleaned again before electromigration. We limit this last oxygen clean to 20 seconds in the Applied Materials, because an excessive etch can cause the bridges to collapse. It is wise to calibrate the effect of RIE cleaning on the bridges by SEM imaging.

Figure 3.8 (a) shows a typical $I - V$ curve obtained while breaking one of our wires. The suspended wires we use (as opposed to wires in contact with a

substrate) almost always break in one sharp step when a voltage ramp is applied to them. The resistance obtained varies widely, from 10's of $k\Omega$ to many $G\Omega$. To achieve more control over the resistance of the wire (or size of the gap), we can ramp a voltage across the junction until the resistance across it is no longer ohmic, then reduce the applied voltage before it breaks. By repeating this procedure, or simply waiting for the wire to break at a fix voltage, we can control the resistance of the tunnel junction created. Kirill Bolotin wrote a script that automates this procedure.

Figure 3.8 (b) and (c) show two suspended bridges after electromigration. In these images we can see the location of the break, but cannot extract the size of the gap. From transport measurements we know that the gap size can be made smaller than 1 nm. In order to wire up single molecules, we deposit a few drops of the appropriate molecular solution on the wires for about 30 seconds, then blow the junction dry and perform electromigration at ≤ 4.2 Kelvin. We adjust the molecular concentration of the solution so that a molecule gets trapped in about 30 % of the junctions. Details concerning how the junctions are characterized will be provided in chapter 5.

3.4 Nanotube devices

One molecule of great interest is the carbon nanotube. The fabrication process we described above is not suited for incorporating this molecule into g-MCBIJ devices. In this section, we discuss what changes were made to the above procedure to fabricate carbon nanotube mechanical break-junctions.

The flow chart to fabricate carbon nanotube g-MCBIJ devices is shown in Fig. 3.9. It is important to avoid RIE O_2 cleaning after the carbon tubes are grown

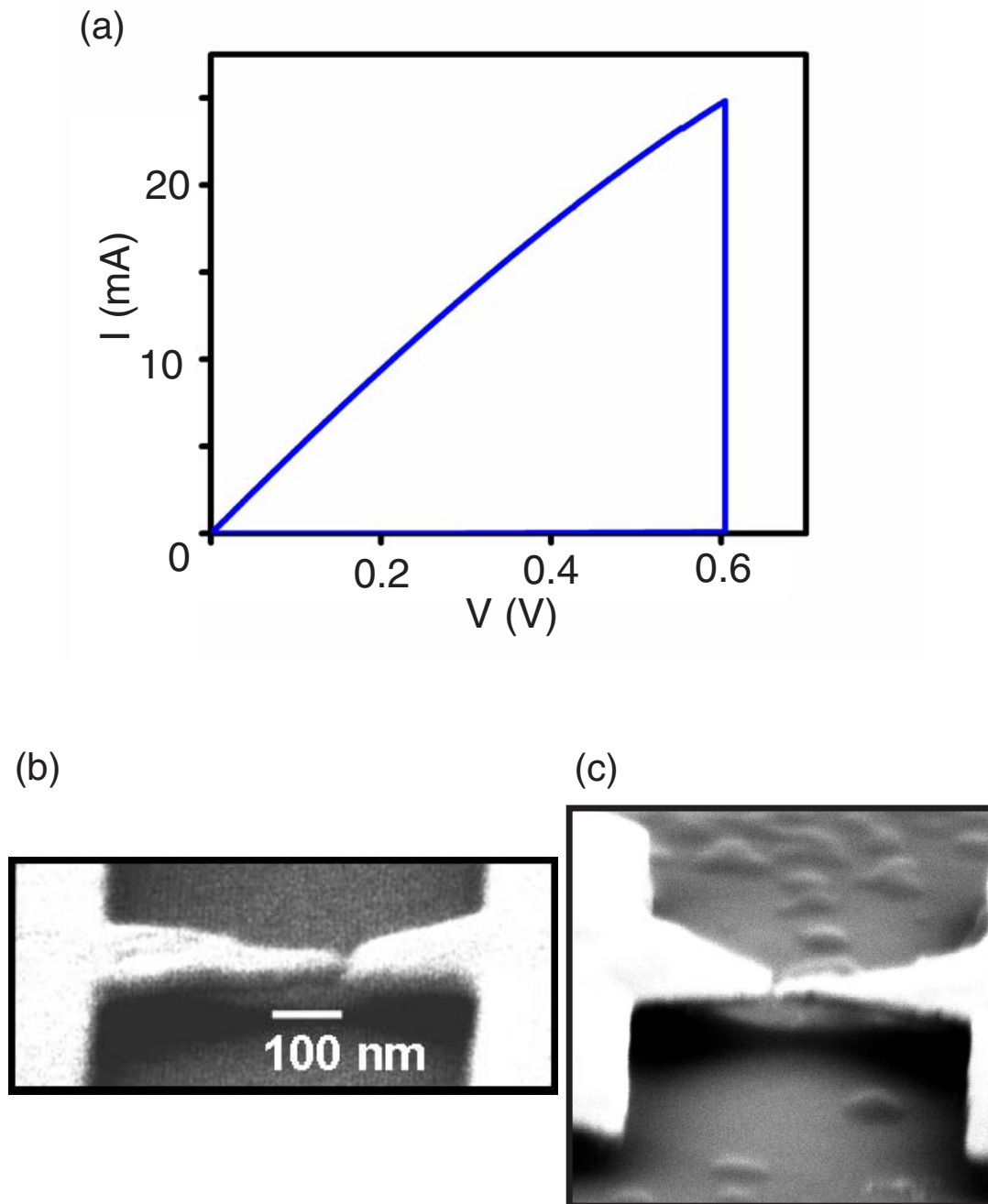


Figure 3.8: [Electromigration] An electromigration technique used to create Au contacts with a nm-size gap [4]. (a) $I - V$ curve showing how a suspended Au junction is electromigrated by ramping a voltage across it. (b) and (c), SEM images of junctions after electromigration.

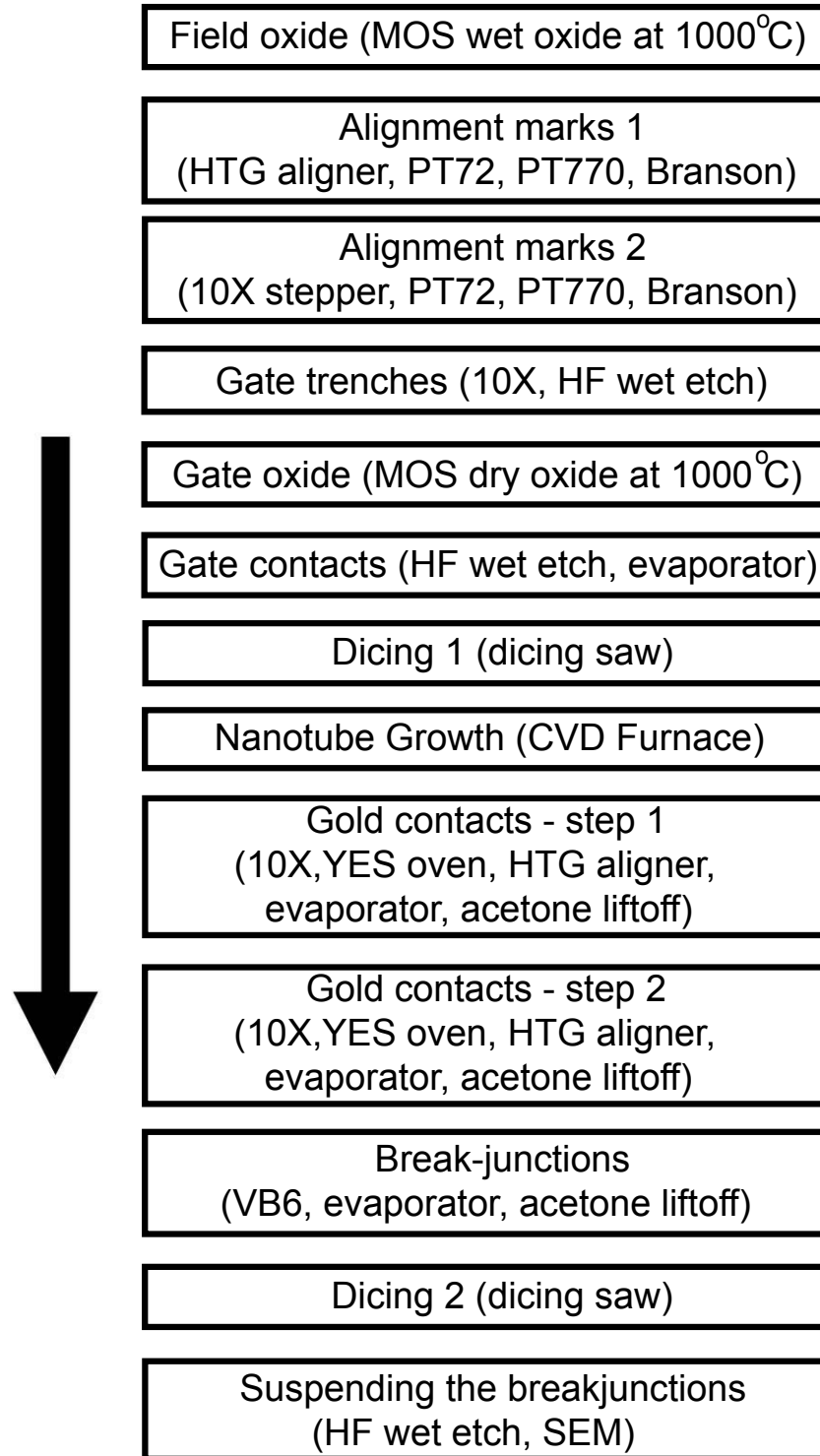


Figure 3.9: [Gated-nanotube-in-break-junction fabrication] Flowchart diagram for the fabrication of g-MCBI incorporating single carbon nanotubes. (note: O₂ RIE etches are to be avoided)

and until the e-beam metal layer is deposited. The fabrication steps are as follows:

1. Grow the field oxide as described in section 3.2.1.
2. Make 10X alignment marks as described in section 3.2.2.
3. Using the 10X stepper and a mask on which there are two GCA keys spaced 10 mm apart, repeat the same procedure as was used to make the previous alignment marks. This time, step the alignment marks into every die using the parameters given in section 3.2.2. These new alignment marks are etched the same way as the previous ones (section 3.2.2). The alignment marks created can be seen on the sides of every die in Fig. 3.6 (b).
4. Make gate trenches, grow gate oxide, and fabricate gate contacts as described in section 3.2.2.
5. Using the method laid out in section 3.2.3 dice the wafers into chips one die wide and 6 dies long (15 mm × 36 mm). This is necessary since the furnace used to grow the nanotubes can only accommodate chips less than 1 inch wide.
6. Grow the carbon nanotubes in the McEuen group chemical vapor deposition (CVD) furnace. To do so:
 - (a) Make a $\text{Fe}(\text{NO}_3)_3$ catalyst solution. The concentration should be adjusted to achieve a large tube density but not so large as to disturb the lithography. I have found that the optimal concentration is about 15 mg of $\text{Fe}(\text{NO}_3)_3$ in 90 mL of IPA. Soak the chip in the catalyst for 15 seconds and blow dry.

- (b) Heat the furnace to 700 °C in 1 SLM (Standard Liters per Minute) of Argon.
 - (c) Anneal the chips for 15 minutes in 0.15 SLM of Ar and 0.1 SLM of H₂.
 - (d) Grow the tube for 6 minutes by flowing 5.5 sccm of C₂H₄.
 - (e) Cool the furnace down in 1 SLM of Ar.
7. Make the Au contact pads and wiring on each chip by using the method described in section 3.2.2, but avoid oxygen plasma cleaning.
 8. Spin and bake an e-beam-resist bilayer as per section 3.2.3. Expose the e-beam pattern on each chip. Two CAD patterns were used, one is very similar to the one used in section 3.2.3, the other one is made up of two electrodes spaced apart by 100 nm. Both CAD patterns are available on the VB6 at VB.USERS.RALPH.ALEX.NTUBES.FRE. Figure 3.10 (a)-(b) shows the two patterns. The alignment procedure is involved but has been automated in a script (see VB.USERS.RALPH.ALEX.NTUBES.ALIGN_NT_CHIP.COM). The job file is available in
VB.USERS.RALPH.ALEX.NTUBES.20DEC04.WAFER_Y_EMIG.COM.
 9. Evaporate 32 nm of Au.
 10. Liftoff in 1:1 acetone:dichloromethane for a few hours.
 11. Oxygen clean the chip. For the break-junction e-beam pattern, RIE for 60 seconds in the Applied Materials. The idea is to etch away all the nanotubes that may be shorting the source and drain electrodes to the backgate. The tubes of interest are by default buried under the Au electrodes and will not be bothered by the oxygen clean. For the 100-nm-gap junctions, we must make

a photoresist mask to protect the 100-nm-gap during the oxygen clean. This is done by standard photolithography on the 10X stepper using a negative mask with $5\ \mu\text{m} \times 5\ \mu\text{m}$ squares located over each junction. A careful alignment is necessary. The chips can then be oxygen cleaned.

12. Dice by hand each chip into its six dies.
13. HF etch (BOE 6:1) the chips to suspend the break-junctions or in the case of gap junctions, the tubes themselves. The etch time for the gap junctions should be kept short enough to leave some oxide between the tube and substrate even after the tube is released. The etch time must be carefully calibrated.

Details concerning the characterization of the samples will be given in chapter 6. Figure 3.10 (a) shows a single carbon nanotube in a gated 100-nm-gap junction, Fig. 3.10 (b) shows a single nanotube in a g-MCBI junction.

3.5 Metallic particle devices

We now briefly comment on how the devices fabricated in section 3.2 can be used to study nanometer-size metallic grains instead of single molecules.

In order to wire-up a single nm-size metallic grain with one of our g-MCBI junctions we need to: suspend the junction with a wet HF etch, oxygen clean the junction, electromigrate the junction, then deposit a small amount of metal inside an evaporator on top of the junction. If the thickness deposited is inferior to the thickness necessary to create a continuous film, the metal evaporated balls up in small particles a few nm across. We rely on the residual surface contamination (carbon?) on the electrodes to act as an insulating barrier between the electrodes

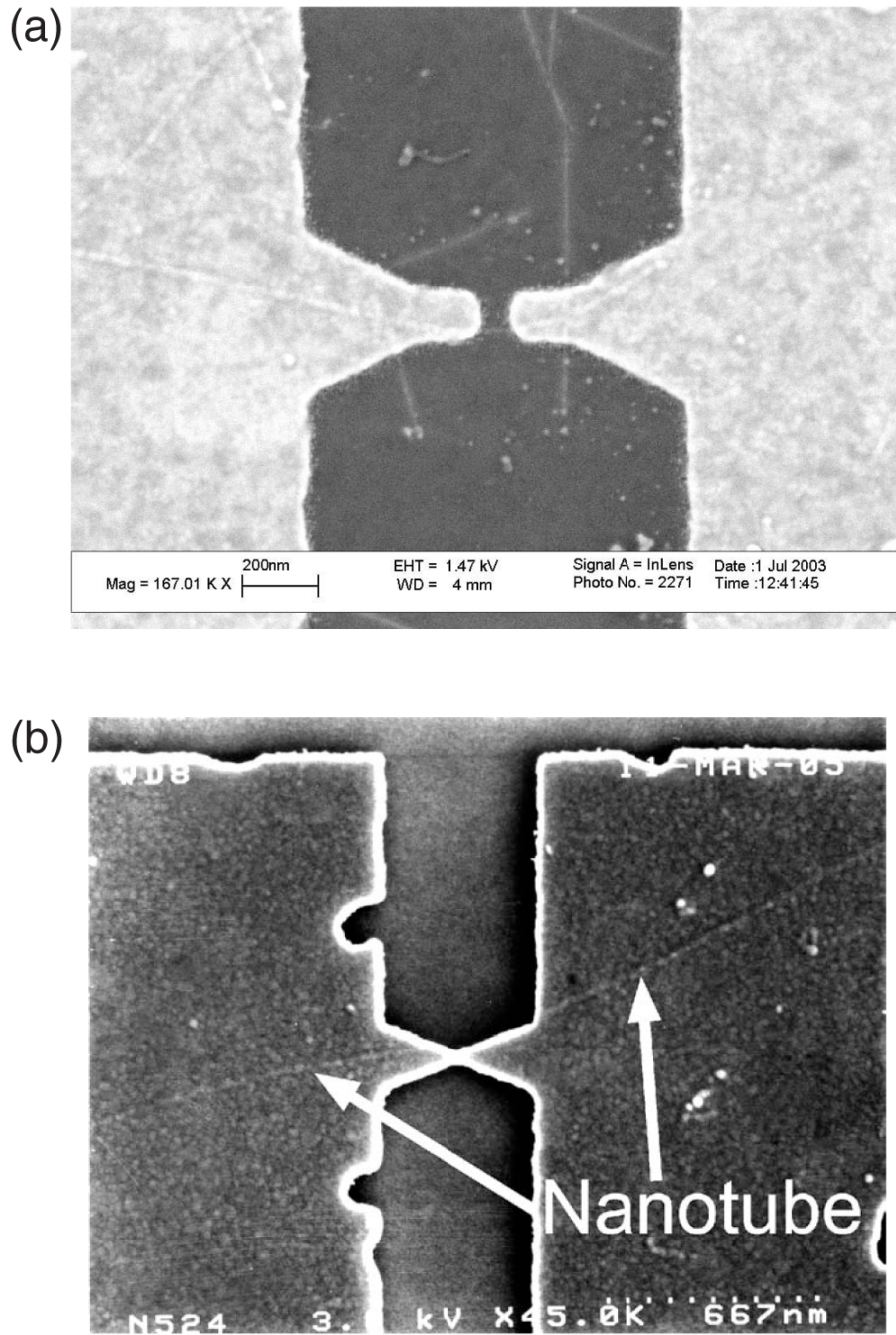


Figure 3.10: [Gated-nanotube-in-break-junction] SEM images showing a single carbon nanotube wired-up in (a) a 100-nm-gap junction and (b) a break-junction.

and the evaporated particles. This technique was used by Kirill Bolotin and Ferdinand Kuemmeth to make gated metallic quantum-dot transistors [6]. Figure 3.11 shows a suspended g-MCBJ junction made of 20 nm of Iridium, after it has been electromigrated, and on top of which 20 Å of Au were evaporated. We used Ir instead of Au to make the suspended bridge of this device because we need to perform electromigration at room temperature, prior to the evaporation. When gold nanowires are electromigrated at room temperature they form rather large gap (> 10 nm) which are not suitable for contacting a small particle. On the other hand Ir forms very small gaps even when electromigrated at room temperature. Iridium also has the advantage of having a larger Young's modulus which makes the bridge more resistant to oxygen cleaning and thermal cycling.

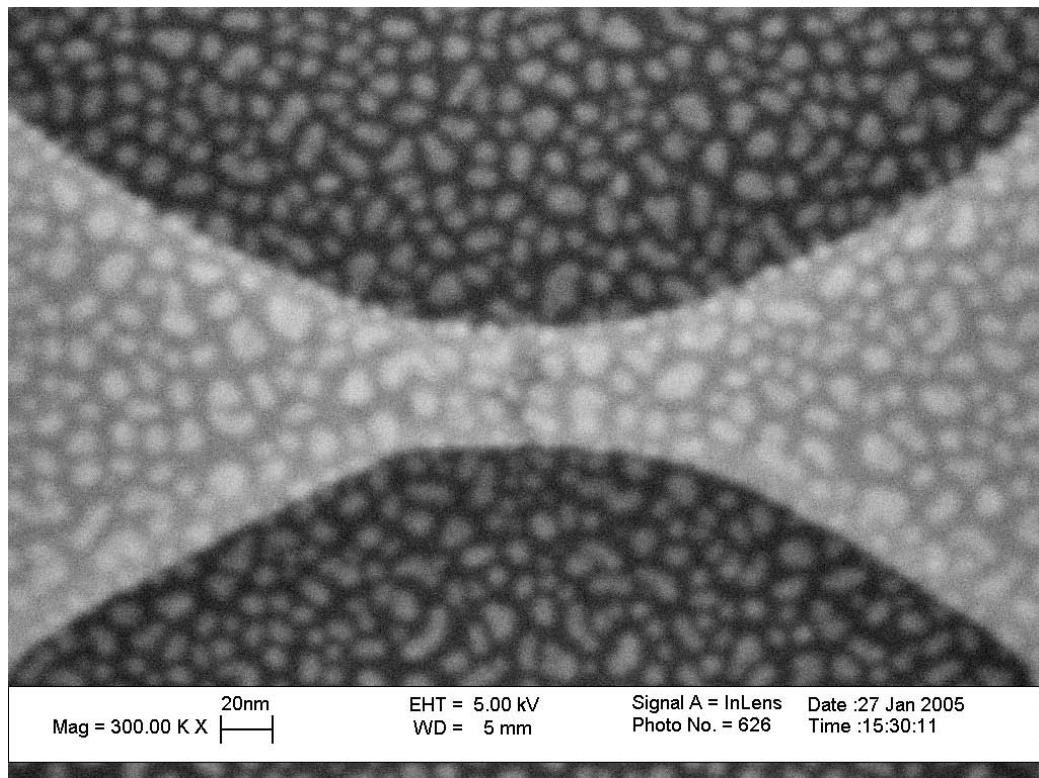


Figure 3.11: [Metallic nano-grains in g-MCBIJs] Top view of an Iridium g-MCBIJ which was electromigrated and on which Au nanoparticles were evaporated.

BIBLIOGRAPHY

- [1] J. M. vanRuitenbeek et al., Review of Scientific Instruments **67**, 108 (1996).
- [2] A. N. Pasupathy, PhD thesis, Cornell University, 2004.
- [3] J. Park, PhD thesis, University of California, Berkeley, 2003.
- [4] H. Park, A. K. L. Lim, A. P. Alivisatos, J. Park, and P. L. McEuen, Applied Physics Letters **75**, 301 (1999).
- [5] Micro Precision Equipment, 4986 Hwy 380, Greenville, TX 75401.
- [6] K. I. Bolotin, F. Kuemmeth, A. N. Pasupathy, and D. C. Ralph, Applied Physics Letters **84**, 3154 (2004).

Chapter 4

Measurement setup: gated-mechanically controllable break-junction technique (g-MCBI)

4.1 Introduction

A mechanically controllable break-junction (MCBJ) consists of a narrow bridge of metal suspended above a flexible substrate (see Fig. 4.1) [1, 2, 3, 4]. By bending the substrate, one can break the bridge and then adjust the spacing between the resulting electrodes. A brief introduction to the MCBJ technique was given in chapter 1, and we described how we fabricate gated-MCBJ devices in chapter 3.

Most of MCBJ experiments make use of a combination of a mechanical coarse approach and a piezoelectric fine tuning to bend a phosphorus-bronze chip on which MCBJ devices are built. The main advantages of using a piezoelectric stack to bend the substrate is that it can achieve very fine positioning and has a fast response time. In order to equip our MCBJs with a gate electrode, we use a silicon substrate. The smoothness of a single crystal Si wafer (as opposed to a metallic substrate) allows us to built junctions suspended only 40 nm above the wafer, which can then be used as an effective back-gate. The drawback of a silicon substrate is that it is relatively brittle. Therefore it only permits a small amount of substrate bending, and a large force is required to bend it. The limited bending range of Si forces us to make use of electromigration to initially break the junctions, as was described earlier (section 3.3). The large force needed to bend

a silicon chip precludes the use of a piezoelectric element to bend Si chips. We therefore resort to a purely mechanical assembly for bending. In order to achieve a mechanical control level as high as the one achieved in piezo-driven MCBJs, we fabricated very small junctions (the amount of electrode displacement scales with the junction's size as we will see in section 4.2.3), and we built a refined mechanical assembly that ensures a smooth and accurate motion.

In this chapter, we will discuss the techniques and hardware we developed to make measurements on g-MCBJ devices [5]. First, we describe in section 4.2 a 4-Kelvin assembly we use to operate and measure g-MCBJ samples. We discuss the design, operation and calibration of this apparatus, which we used to acquire the data presented in chapter 5. We then describe a recently built mechanical assembly which fits inside a more versatile fridge (section 4.3). This new measurement setup enables a number of new experiments which we are now pursuing (see chapter 6). In section 4.4, we briefly describe the electronics we use to make measurements. We conclude by commenting on possible improvements to the g-MCBJ devices.

4.2 Four Kelvin setup

Figure 4.2 shows a diagram of the 4-Kelvin fridge (Desert Cryogenics) we use. The fridge is a “dip-stick”, equipped with a vacuum can which can be loaded in a liquid helium dewar. The fridge has a 1-Kelvin pot, but is used only at 4.2 Kelvin. A small amount (10-20 mTorr) of ^4He exchange gas must be kept in the vacuum can at all time in order to insure that the sample sits at base temperature. The fridge is equipped with a thermocouple thermometer which is located inside the vacuum can.

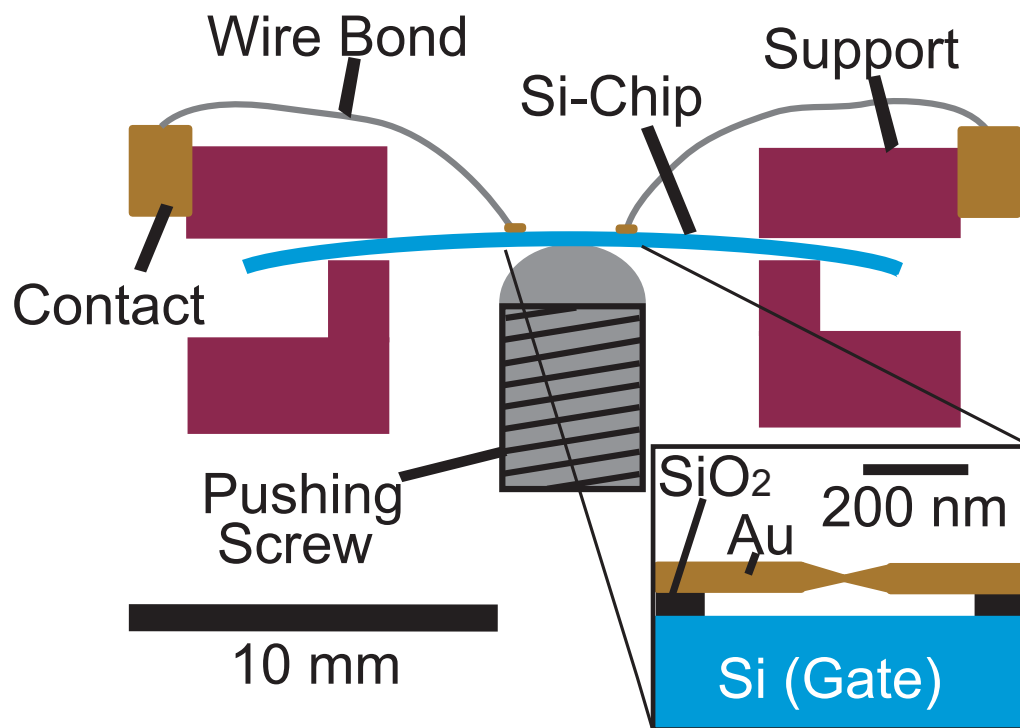


Figure 4.1: [Gated-MCMBJ technique] Design of the experimental apparatus.

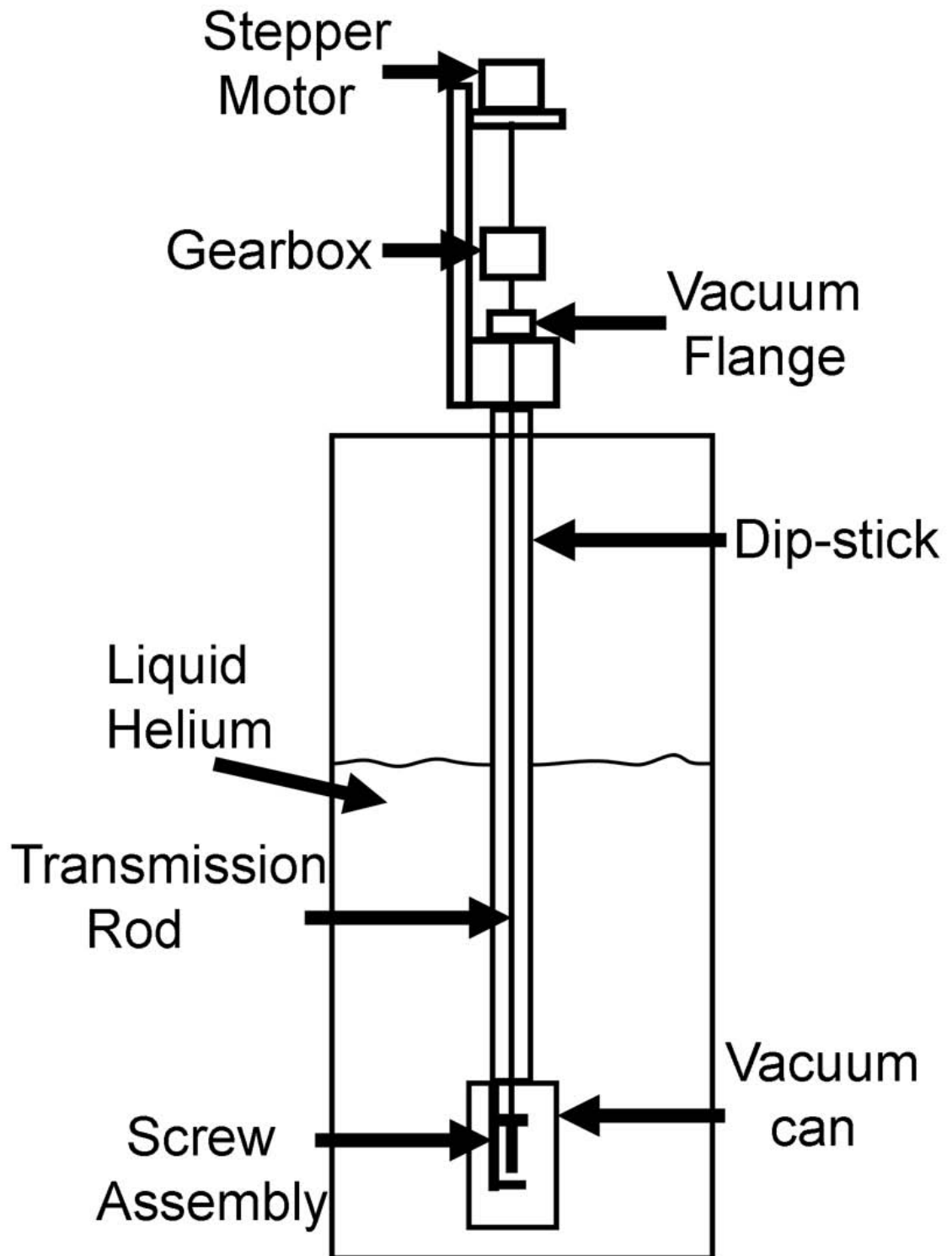


Figure 4.2: [4-Kelvin fridge] Diagram of the 4-Kelvin MCBJ assembly.

4.2.1 Mechanical assembly

Figure 4.3 (a) and (b) show pictures of the mechanical assembly used to bend the chips on which the g-MCIBJs are built. On top of the dip-stick (Fig. 4.3 (a)) we mounted a stepper motor (Danaher Motion) which has an angle resolution of less than 2 degrees, and outputs a large torque. The motor axis' motion is reduced via a gearbox (Pic-Design) with a ration 50.8:1. The gearbox's output axis is then mounted to a rotational vacuum coupling that mounts on top of the dip-stick. The rotational motion is sent down the stick, via a stainless steel rod, all the way to the vacuum can. Inside the can, Fig. 4.3 (b), two meshing gears (Boston Gears) reduce further the motion by a factor of two and transmit the motion from the SS rod to a fine threaded (1/80 inch pitch) pushing screw (Thorlabs).

Figure 4.1 shows the geometry of the sample mount located inside the vacuum can. We place a 15-mm long by 6-mm wide Si chip on which there are 36 g-MCIBJ devices (see chapter 3) against two supports spaced 10 mm apart, and apply a pushing screw to the middle of the chip (Fig. 4.3 (b) and (c)). We can then use the stepper motor to controllably rotate the screw and bend the chip. As many as 16 devices can be wire bonded at once (Fig. 4.3 (c)). The amount of bending allowed by the Si chip (≈ 0.3 mm over 10 mm) is generally not sufficient to break the metal bridge by mechanical motion alone. Therefore we first break the wires partially or fully at 4.2 K using electromigration, a technique used previously to make nm-scale gaps for molecular transistors [6, 7, 8].

4.2.2 Sample handling

A few comments are in order about the handling and preparation of samples and the fridge. Samples should be oxygen cleaned just prior to their wire bonding

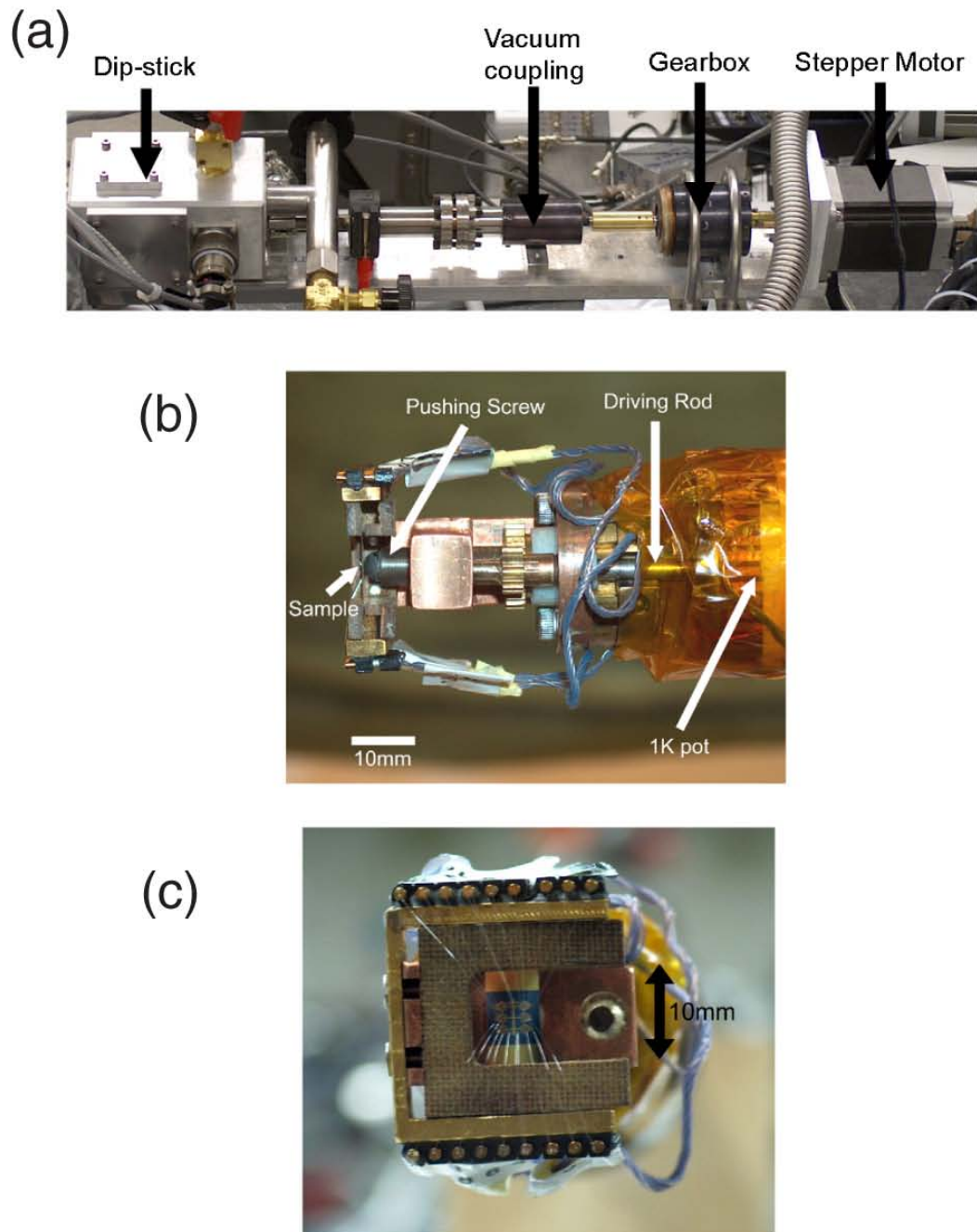


Figure 4.3: [4-Kelvin mechanical assembly] Pictures of the 4-Kelvin fridge. (a) The motor assembly mounted on top of the dip-stick. (b) The pushing screw assembly located inside the vacuum can. (c) Top-view of the sample holder, showing a wire bonded chip.

and cool down to remove possible surface contamination. For mounting a chip on the fridge, the screw-holder assembly is dismounted from the dip-stick and a chip is mounted on the holder. The screw-holder assembly is then mounted onto a wire bonding jig which is compatible with the CNF wire bonder. The wire bonding is complicated by the fact that the sample contact pads and the holder contacts are not in one plane (see Fig. 4.3 (b)). Still, with some practice and by keeping the sample holder's contacts nicely polished, the bonding can be relatively straightforward. During and after the wire bonding, great care must be taken to keep the samples grounded at all times to prevent electrostatic discharges that can kill them.

The cool down procedure for the 4-Kelvin fridge is simple but not trivial, and the manual should be consulted prior to cooling down. Before cooling down, a ^4He exchange gas is added to the vacuum can. The samples are then cooled down to liquid helium temperature, after which most of the exchange gas is removed (leaving about 10-20 mTorr). The samples should be given an hour or so to thermalize before beginning measurements. Once the samples are cold, they are electromigrated and measured.

4.2.3 Mechanical motion calibration

After the samples have been electromigrated, the distance between the source and drain electrodes of the junctions can be mechanically tuned. The data shown in Fig. 4.4 (a) shows how a junction's resistance increases smoothly upon bending the substrate. To calibrate this mechanical motion, we performed measurements at 4.2 K on bare Au electrodes with an initial tunnel resistance in excess of 100

$K\Omega$.¹ The resistance of a tunnel junction is expected to depend on the width x of the tunneling barrier approximately as [9]

$$R \propto e^{2\kappa x} \quad \kappa = \frac{\sqrt{2m_e\phi}}{\hbar} \quad (4.1)$$

where $\phi = 5.1$ eV is the Au work function and m_e the electron mass. From the data in Fig. 4.4 (b), we extract a calibration of 5.57 ± 0.06 pm per full rotation of the stepper motor. The average over our devices is 5.4 ± 0.3 pm/turn. The full range of motion available before the substrate breaks is generally 5 \AA . A few devices (not included in the average) exhibited much less motion per turn, together with large gate leakage currents (> 1 nA at a gate voltage $V_g = 1$ V). In SEM images, these were identified as collapsed bridges.

If the substrate of our chips bends uniformly, the expected source-drain displacement is [4]

$$\delta x = \frac{3ut}{L^2} \delta y \quad (4.2)$$

where u is the length of the suspended bridge (500 nm), t is the wafer thickness (200 μm), L is the distance between the two support posts used for bending (10 mm), and δy is the pushing screw displacement (3.1 μm per full rotation of the stepper motor). This formula predicts that the amount of source-drain electrode displacement is reduced by a factor of 3×10^{-6} with respect to the screw motion. We find that a full motor rotation corresponds to $\delta x = 9$ pm, within a factor of 2 of the calibration result. This discrepancy is similar to results from other MCBJ experiments [1, 2, 3, 4]. The difference between the theoretical prediction and our calibration can be ascribed to several factors. Non-uniform bending of the

¹Lower resistance junctions have a very small tunnel gap and are prone to conductance jumps with motion. Most likely because the size of the Au atoms at the interface is comparable to the size of the tunnel barrier.

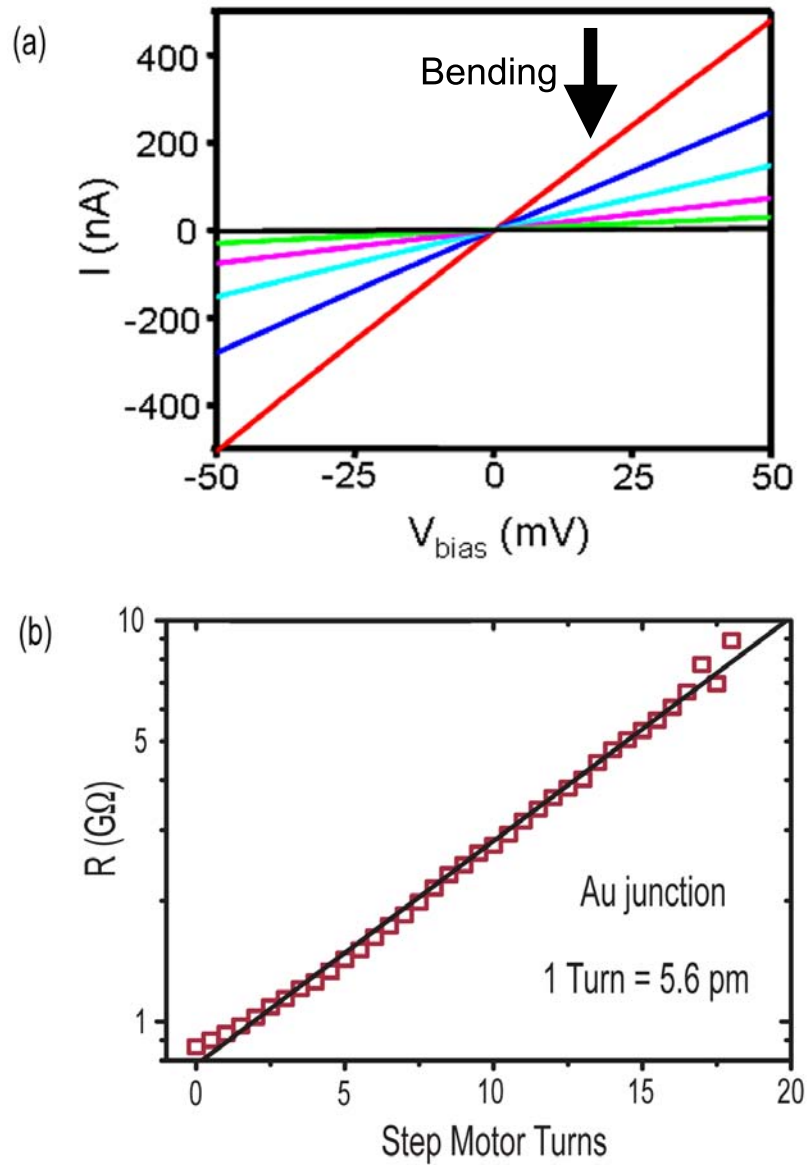


Figure 4.4: [Mechanical motion calibration (4K fridge)] (a) A series of I-V characteristics of a bare Au g-MCBI for different amounts of substrate bending. (b) Resistance of a bare Au g-MCBI versus source-drain displacement at 4.2 K, from which the amount of mechanical motion can be calibrated.

substrate causes departures from Eqn. 4.2 [10]. Also, in reality the potential barrier between the two tunneling electrodes may not be square as is assumed by Eqn. 4.1. It is also known that the tunnel barrier height can be significantly different from the bulk work function. Surface roughness and adsorbed gases can cause large changes in the value of ϕ [4, 11, 12]. For instance it was found that adsorbed ^4He on the Au electrodes can double the effective barrier height [13, 14]. We therefore must see our displacement calibration as an estimate of the true motion, probably valid to within a factor of 2. This uncertainty in the absolute value of our calibration is not detrimental to our measurements since our calibration is reproducible over time and between different samples.

A more accurate calibration for the displacement of MCBJs can be obtained by a technique called field emission resonance (FER) [11, 14]. When a bias voltage larger than ϕ is applied across a tunnel junction, the tilting of the potential barrier creates a potential well, which leads to conductance oscillations as a function of the applied bias voltage across the tunnel junction. By measuring the period of the conductance oscillations one can extract a displacement calibration [11, 14]. We have not tried this calibration method, mainly because it requires the implementation of a feedback system that can maintain a constant current through the junction during the measurement. It would be useful to attempt this calibration in the future.

Figure 4.5 (a) confirms that we have a precise and smooth mechanical control of our junctions. If the electromigration process used to break wires is stopped when the sample conductance reaches a few times G_o ($= 2e^2/h$), mechanical motion can be used to complete the process of breaking the wire, resulting in a stepwise reduction in conductance (see Fig. 4.5 (a)) as observed in other MCBJ devices [4].

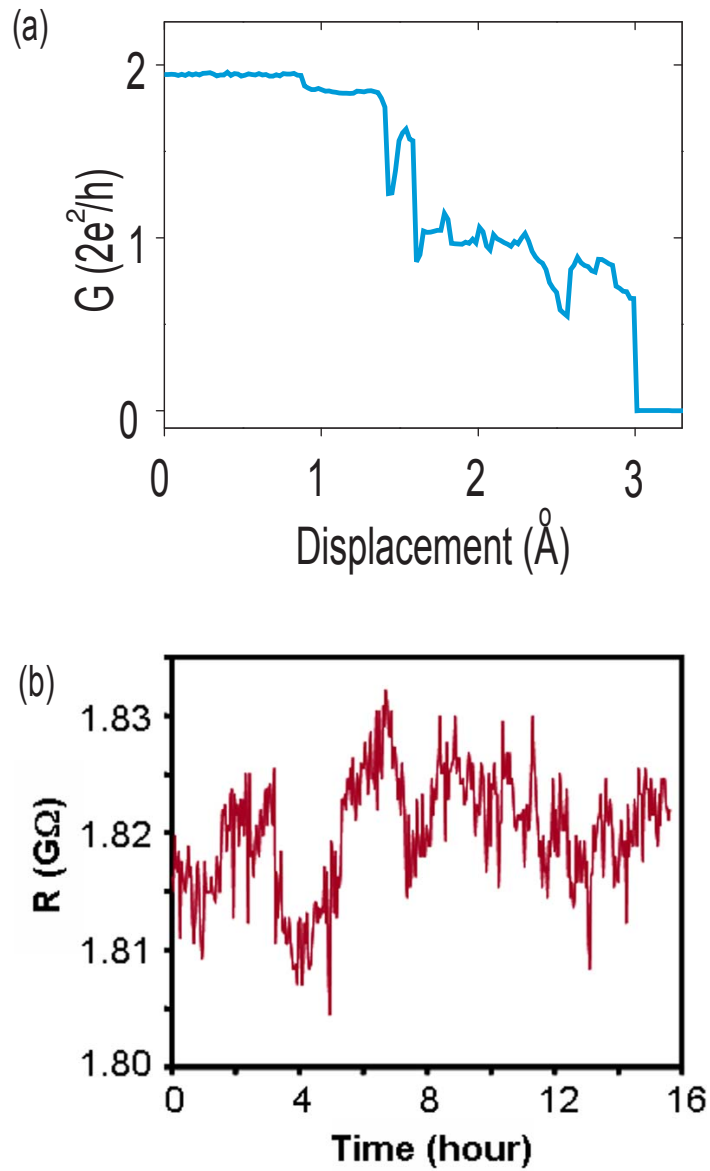


Figure 4.5: [Mechanical stability] (a) When an atomic-scale metal contact remains after electromigration, mechanical motion can be used to complete the process of breaking the wire. (b) Resistance of a calibrated g-MCBI as a function of time. From the mechanical calibration of the junction we can conclude that the displacement of the source-drain electrodes drift by less than 1 pm over several hours.

In the case of a Au wire, a single quantum of conductance corresponds to a single atom bridging the junction. Therefore, Fig. 4.5 (a) gives of confidence that our motion is smooth down to the atomic scale. We expect that the length of the last conductance plateau ($G = G_o$) should be of the order of the Au-atom interatomic spacing for a 1-d chain ($\approx 2.7 \text{ \AA}$ [15]).

A quantitative measure of the stability of our junctions over time is shown in Fig. 4.5 (b). The data shown is acquired by biasing at a constant voltage the junction from which we obtained the calibration curve in Fig. 4.4 (b). By converting the resistance fluctuations in Fig. 4.5 (b) into displacements using Eqn. 4.1 we find that the junction drifted by much than 1 pm over several hours. This great stability of the junctions is due to the huge reduction factor between the motion of the pushing screw and the motion of the electrodes. We can think of an MCBJ as a 1-dimensional scanning tunneling microscope (STM) with a very small mechanical loop. For our devices, the mechanical loop is only 1 μm in size (see the inset of Fig. 4.1) which prevents vibrations from coupling in. The stability of the devices allows us to measure them over long periods of time.

4.3 Variable temperature setup

To enlarge our experimental capabilities, and with some experiments in mind (see chapter 6), we built a second MCBJ apparatus. This assembly is in many ways similar to the previous one (see section 4.2), but fits inside a different fridge (VTI fridge). The VTI provides us with three main advantages with respect to the prior setup: it has a base temperature of 1.5 Kelvin, it is equipped with a 14 Tesla superconducting magnet, and it allows us to controllably vary the sample temperature between 1.5 K and 300 K.

4.3.1 Mechanical assembly

Pictures of the top (motor) and bottom (screw) of the mechanical assembly of the VTI insert are shown in Figure 4.6 (a) and (b). In order to minimize the weight and vibrations of the insert, a small (1/2 stack) stepper motor is used in this assembly. The reduction gearbox we use here has a reduction factor of 100:1. Due to space limitations there is no second stage of motion reduction, and the stainless steel transmission rod directly drives the pushing screw. In order to decouple the pushing screw from the vibrations in the transmission rod, as well as to minimize backlash, the screw is driven by a “fork” system (see Fig. 4.6 (b)). Also, the pushing screw used here has a finer thread (1/100 inch pitch) than the one previously used. The sample holder (Fig. 4.6 (c)) allows to wire bond up to 18 samples at once, and can conveniently be used with a wire bonding jig compatible with any wire bonding machine. A thermometer is mounted on the insert in close proximity to the sample.

4.3.2 VTI assembly motion calibration

We calibrate the mechanical motion of our samples in the VTI assembly with the same procedure we used in section 4.2.3. Because the thread of the pushing screw used here is 25 % finer than the one used in the 4K-fridge, we expect that the mechanical motion per motor turn we measure will be smaller than the previous calibration (5.4 pm/turn). From the fit in Fig. 4.7 we extract a calibration of 2.5 pm/turn. On average we obtain a calibration of 2.3 ± 0.2 pm/turn. This number is not consistent with our previous calibration (we would expect about 4.3 pm/turn). The two most likely sources for this discrepancy are a change in the effective length of the Au bridge due to a different oxide-etch time, or a variation in

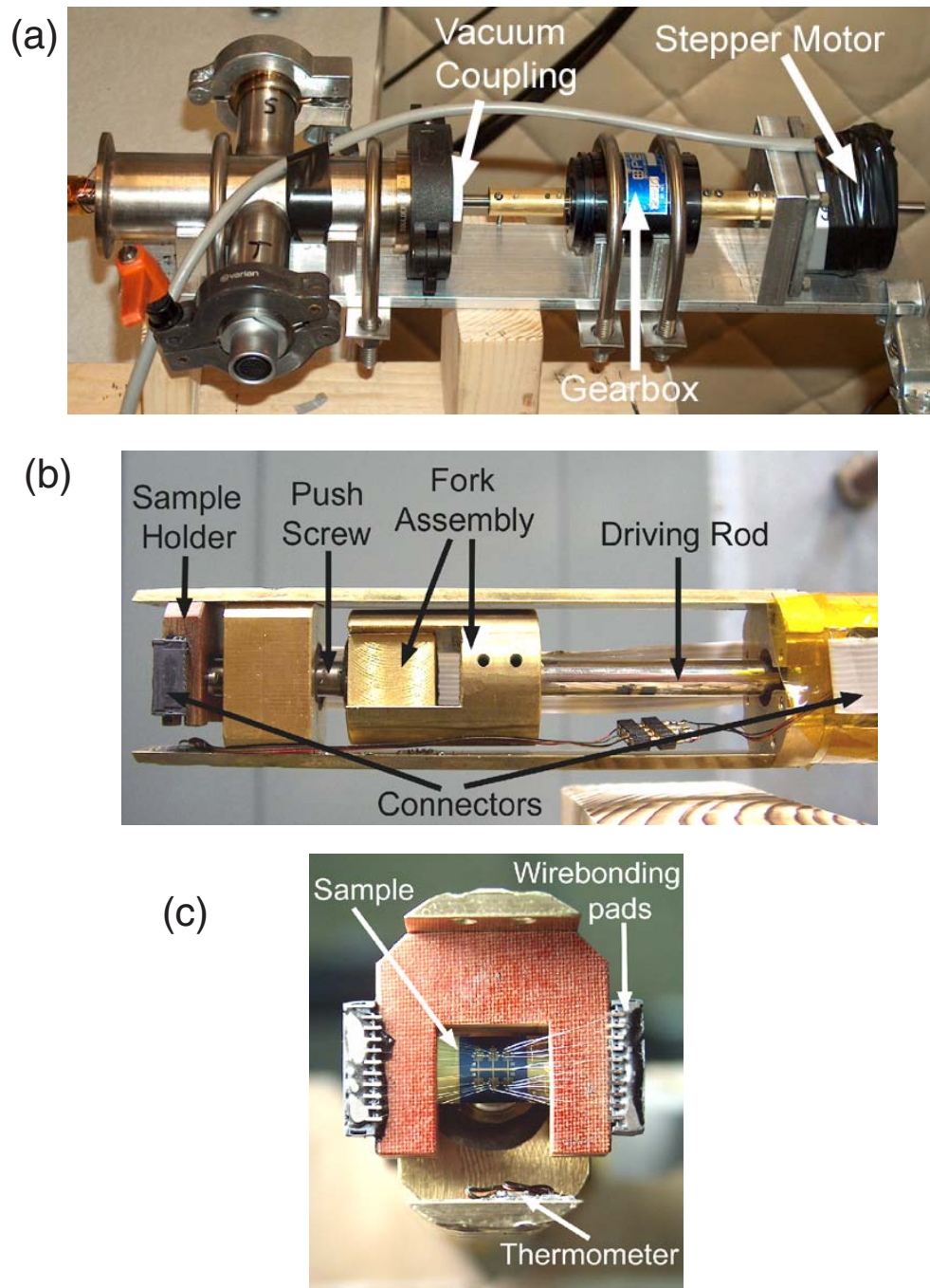


Figure 4.6: [Variable temperature (1.5-300K) assembly] Pictures of the VTI fridge mechanical assembly. (a) The motor assembly mounted on top of the insert. (b) The pushing screw assembly located at the bottom of the insert. (c) Top-view of the sample holder, showing a wire bonded chip.

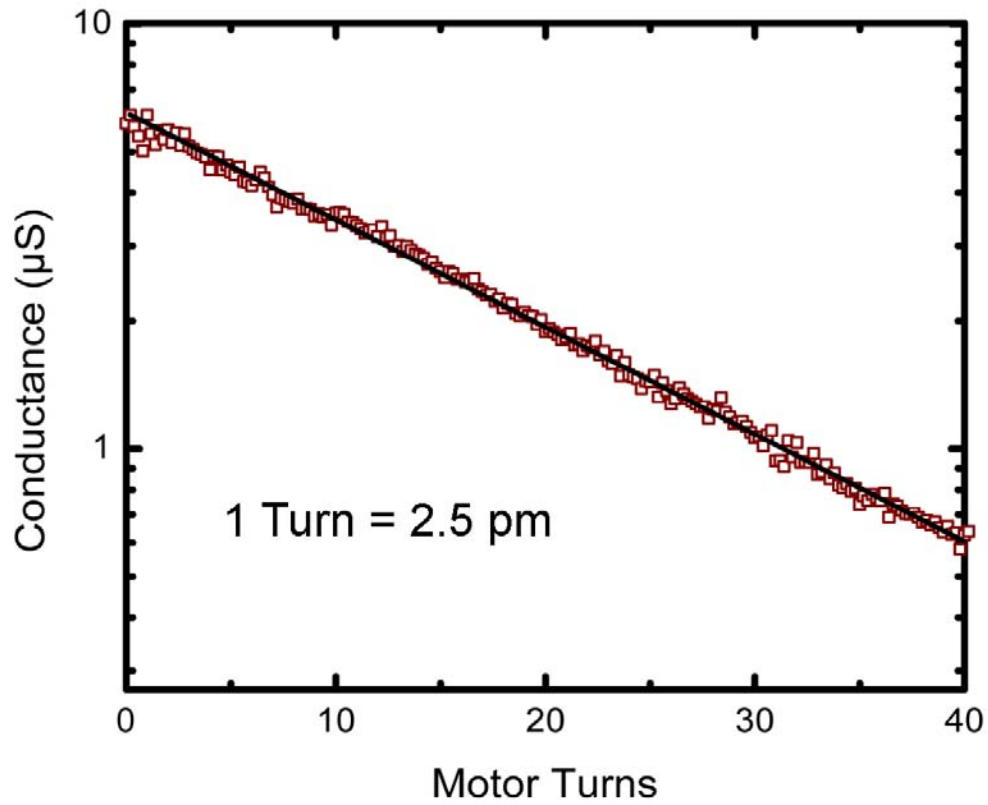


Figure 4.7: [Mechanical motion calibration (VTI fridge)] Conductance of a bare Au g-MCBJ versus source-drain displacement at 1.6 K, from which the amount of mechanical motion in the VTI can be calibrated.

the tunnel barrier height due to helium adsorbed on the electrodes. It is probable that the overall exposure to ^4He is smaller in the VTI than the 4K-fridge since the sample is never exposed to a large pressure of helium in the VTI. Nevertheless, since the calibration is reproducible, it is not a major limitation at this point.

4.4 Electronics

Most of the measurements we made were carried out at 4 Kelvin, and only required a moderate level of electronics sophistication. As we move to more refined measurements it will become more crucial to improve further the noise filtering and the grounding of our measurement electronics.

Figure 4.8 shows a diagram of the electronics we use. All output voltages are normally sourced from the computer DAQ card. By making use of a voltage divider and RC filters we reduce the noise on the output sources to order of 0.1 mV. To apply gate voltages in excess of 10 Volt, we use a Keithley 2420 source-meter. The current from a device is first pre-amplified by a Ithaco 1211 and then sent to the computer. Finally, a carefully wired BNC break-out box is used to interface the measurement setup with the sample lines.

The software used for the data acquisition was specifically written for this experiment. It was designed to handle the data transparently and be easy to upgrade. The software is called “MBJ” and can be found on a few computers around the Ralph group lab.

Now that we have described how our measurements are made, we are ready to demonstrate that g-MCBJs can be used to study electronic transport in single molecules. But before we do so, we comment on possible improvements and extensions to the g-MCBJ technique.

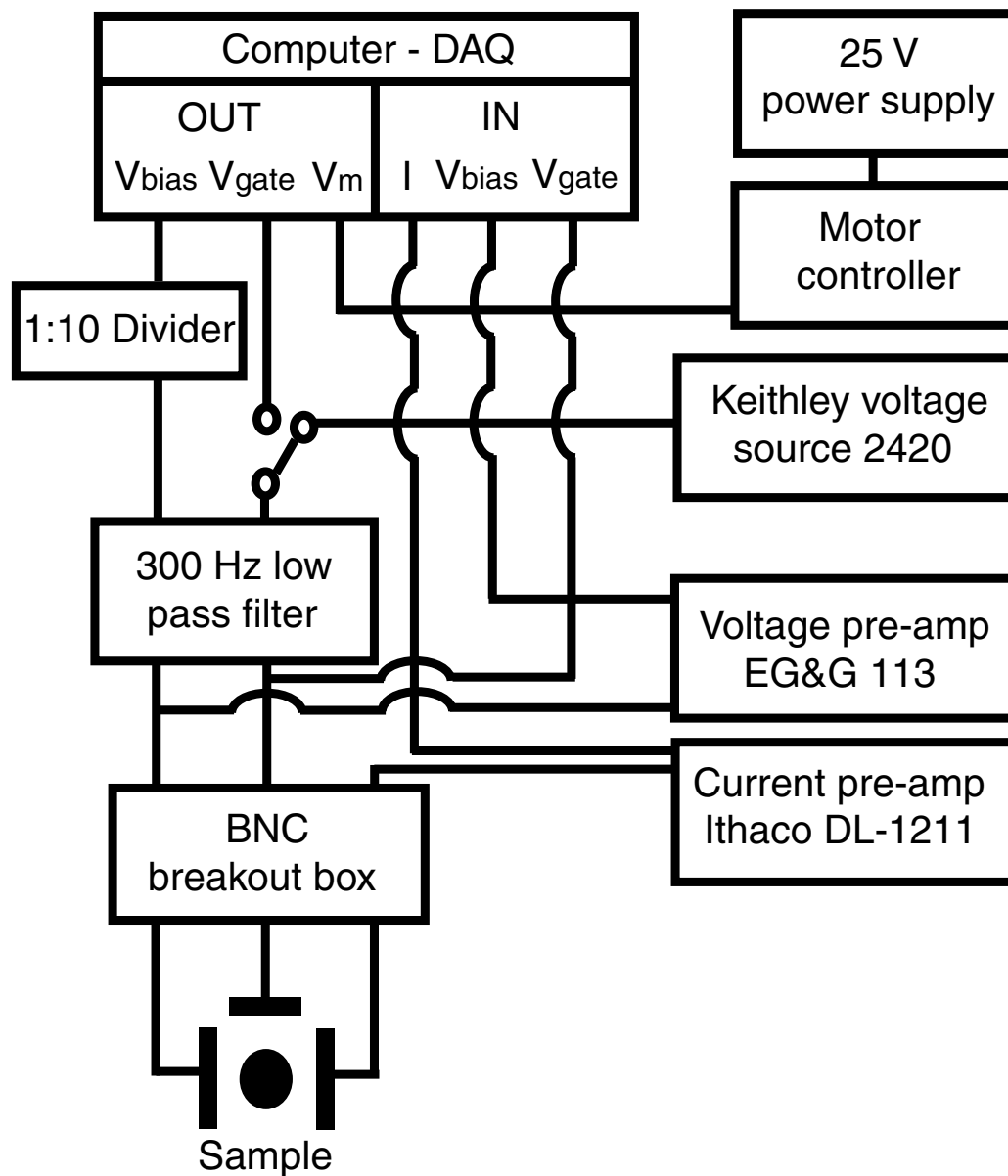


Figure 4.8: [Electronics used for measuring MCBJ samples] Schematic of the electronics.

4.5 Future improvements

The main limitation to our experiments is the relative fragility of our devices. Primarily, the Au bridges forming our MCBJs are susceptible to collapse when oxygen plasma cleaned, thermally cycled or even electromigrated. In order to circumvent these problems, we have kept the Au bridges fairly thick (32 nm) and short (500 nm). Ideally we would like to make the bridges thinner (to improve gate coupling) and longer (to increase the mechanical motion range). An increased gate coupling could allow us to reach more Coulomb threshold degeneracy points in our devices (see section 2.1.2), and an increased motion range would allow us to build conductance histograms of our devices (see section 1.2.2).

To achieve these objectives we have experimented with fabricating junctions with different metals. Namely we have used Ti, Pt, Ir, Pt-Ir alloys, and Cu. We are especially interested in materials with a Young's modulus larger than the one of Au, since we need to increase the rigidity of the bridge. All the materials we have tried are faced with some limitation: poor electromigration results, high contact resistance, or incompatibility with HF etching. The most promising material is Pt, but we need to reduce the amount of stress in Pt films we deposit since it leads to a bending of the source and drain electrodes. Iridium devices have produced interesting results, but have a large contact resistance.

Another fascinating prospect for future development is to make g-MCBJs out of silicon. It has been shown that heavily-doped Si can be electromigrated, and it should be relatively straightforward to fabricate Si devices by using SOI wafers.

BIBLIOGRAPHY

- [1] J. Moreland and J. W. Ekin, *Journal of Applied Physics* **58**, 3888 (1985).
- [2] C. Zhou, C. J. Muller, M. R. Deshpande, J. W. Sleight, and M. A. Reed, *Applied Physics Letters* **67**, 1160 (1995).
- [3] J. M. van Ruitenbeek et al., *Review of Scientific Instruments* **67**, 108 (1996).
- [4] N. Agrait, A. L. Yeyati, and J. M. van Ruitenbeek, *Physics Reports-Review Section of Physics Letters* **377**, 81 (2003).
- [5] A. R. Champagne, A. N. Pasupathy, and D. C. Ralph, *Nano Letters* **5**, 305 (2005).
- [6] H. Park, A. K. L. Lim, A. P. Alivisatos, J. Park, and P. L. McEuen, *Applied Physics Letters* **75**, 301 (1999).
- [7] H. Park et al., *Nature* **407**, 57 (2000).
- [8] J. Park et al., *Nature* **417**, 722 (2002).
- [9] R. Wiesendanger, *Scanning Probe Microscopy and Spectroscopy*, Cambridge University Press, 1994.
- [10] S. A. G. Vrouwe et al., *Physical Review B* **71**, (2005).
- [11] O. Y. Kolesnychenko, O. I. Shklyarevskii, and H. van Kempen, *Review of Scientific Instruments* **70**, 1442 (1999).
- [12] B. Ludoph, *Quantum Conductance Properties of Atomic-size Contacts*, PhD thesis, Leiden University, 1999.
- [13] O. Y. Kolesnychenko, O. I. Shklyarevakii, and H. van Kempen, *Physical Review Letters* **83**, 2242 (1999).
- [14] A. I. Yanson, PhD thesis, Leiden University, 2001.
- [15] A. I. Yanson, G. R. Bollinger, H. E. van den Brom, N. Agrait, and J. M. van Ruitenbeek, *Nature* **395**, 783 (1998).

Chapter 5

Electrostatic and mechanical control in single-C₆₀ devices

5.1 Introduction

A primary challenge in the field of single-molecule electronics [1, 2] is to develop adjustable devices that can enable well-controlled, systematic experiments. If one uses techniques that measure only a current-voltage ($I - V$) curve, it can be difficult to determine even whether a molecule is present between electrodes, because nonlinear transport across tunnel junctions or metallic shorts can easily be mistaken for molecular signals [3]. Previous efforts to overcome this difficulty have employed two separate strategies (briefly described in chapter 1) for systematically adjusting a molecular device *in situ* to make changes that can be compared with theory. Electrostatic gating permits control of electron transport through a molecule by shifting its energy levels [4, 5, 6, 7]. Mechanical adjustability, using scanning probes [8, 9, 10, 11] or mechanically-controlled break junctions [12, 13, 14, 15], enables manipulation of the device structure and the strength of bonding to electrodes. Here we report the implementation of both electrostatic gating and mechanical adjustability within the same single-molecule device [16]. This combined capability enables a detailed characterization of electrical transport in molecules, providing understanding that is not possible with just gating or mechanical adjustability separately. Our scheme for combining electrostatic gating and mechanical adjustability is to add a gate electrode to a mechanically controlled

break-junction (MCBJ). The fabrication of these devices was described in chapter 3, and the experimental apparatus used to measure them was presented in chapter 4.

In this chapter we demonstrate the devices' performance using C_{60} molecules (see Fig. 5.1 (a)). Figure 5.1 (b) shows a cartoon of one of our single molecule transistors. From this picture we expect that mechanical motion of the electrodes will modify the tunnel junctions on either side of the C_{60} molecule. Figure 5.1 (c) shows a cartoon of the band alignment between the Fermi levels of the leads and the discrete energy spectrum in the molecule (see chapter 2).

5.2 Sample preparation

To characterize the performance of the gate electrode, we must insert into the device a molecule with low-lying energy levels, which can be shifted by the gate voltage (V_g) to modulate current flow. We chose C_{60} molecules because they have been used successfully to make single-molecule transistors, and have shown a variety of interesting physics [4, 7, 17]. To fabricate C_{60} devices, we first clean unbroken Au wires in acetone, isopropanol, and oxygen plasma. We deposit a 0.2 mM solution of C_{60} in toluene on the chip, and blow it dry after 30 seconds. Then we cool to 4.2 K and perform electromigration on each device until the conductances fall below a quantum of conductance. In approximately 30% of samples, one or more C_{60} molecules bridge between the electrodes [4]. We identify these samples as the ones whose $I - V$ curves display Coulomb blockade characteristics, with non-negligible current only for $|V|$ greater than threshold values that depend on V_g . Control junctions formed from bare Au electrodes did not exhibit such Coulomb blockade characteristics. All the measurements that we will describe were conducted at 4.2

Kelvin, unless specified otherwise.

5.3 Gate and mechanical control

5.3.1 Changes in conductance and capacitances

The effect of V_g and V on conductance, at fixed source-drain displacement, is shown in Fig. 5.2 for three samples at two different source-drain distances each. Fig. 5.3 (a) and (b) show the corresponding Coulomb blockade $I - V$ curves for sample #1 at $V_g = 2.5$ V, and #2 at $V_g = 0$. The dark regions on the left and/or right of each panel in Fig. 5.2 correspond to low-current regions of Coulomb blockade. Bright regions denote large dI/dV , where the applied source-drain voltage provides sufficient energy for electrons to tunnel via the molecule and initiate current flow. The threshold required for current flow depends on V_g , which shifts the energy of the molecular states with respect to the Fermi energy of the electrodes. The energy to add an electron to a molecular level can be tuned to zero for a particular value of gate voltage $V_g = V_{deg}$.

As can be seen in Fig. 5.2, the sensitivity of the transport characteristics to V_g varies between samples. This is to be expected because the gate-molecule capacitance C_g will depend on the position of the molecule within the junction. The positive and negative slopes of the tunneling thresholds in Fig. 5.2 correspond, respectively, to the ratios $C_g/(C_g + C_d) \approx C_g/C_d$ and C_g/C_s , where C_s and C_d are the molecule-source and molecule-drain capacitances (see chapter 2 for more details). From the measured slopes in Fig. 5.2, we find ratios of C_g/C_d and C_g/C_s between 2200 and 57. Our smallest value of $(C_s + C_d)/C_g$ is 148 and the largest value is several thousands. The largest gate voltage that we can apply routinely

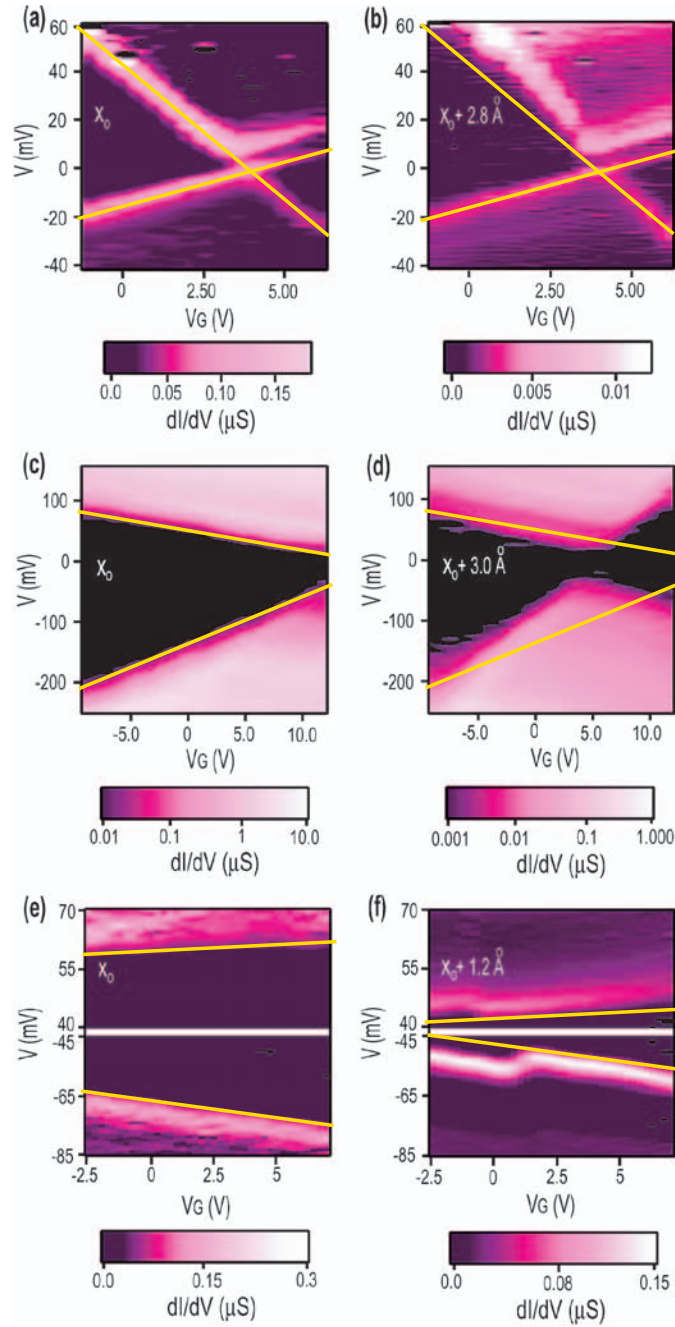


Figure 5.2: [Conductance versus V and V_g] Color-scale plots of dI/dV versus V and V_g for three C_{60} gated-MCMBJ devices at 4.2 K, each at two positions of source-drain displacement. X_0 represents the initial displacement. The relative displacements were determined using the bare-Au calibration value, 5.4 pm/turn. (a-b) Sample #1. (c-d) Sample #2. (e-f) Sample #3. Scans for samples #1, #2 and #3 were acquired every 0.16 Å, 0.27 Å and 0.11 Å, respectively, and showed a smooth evolution with motion.

is ± 12 V, after which the devices fail due to oxide breakdown under the electrode pads. Given this range of V_g , we are able to shift the quantum states on a C_{60} molecule by an energy as large as

$$\Delta E = e \frac{C_g}{C_s + C_d + C_g} \Delta V_g = 160 \text{ meV}. \quad (5.1)$$

The capability to manipulate the energy levels on the C_{60} molecules with a gate allows a detailed analysis of the changes caused by mechanical displacement, providing understanding that is not achievable with either motion or gating alone. First, note in Fig. 5.2 that mechanical motion can change the slopes of the tunneling thresholds. This is a consequence of changes in C_s and C_d . In Fig. 5.4 (a) and (c) we plot C_s/C_g and C_d/C_g for samples #2 and #3. For sample #2, both capacitance ratios change with motion, but for sample #3 only the drain capacitance varies significantly between 0 and 0.8 Å displacement, indicating that the motion predominantly modifies the molecule-drain distance. In this way, the combined capabilities of electrostatic gating and mechanical motion allow one to distinguish qualitatively different motions of the molecule within the junction during electrode displacement. A second change caused by the mechanical motion is that the overall device conductance decreases with increasing displacement (note Fig. 5.3 (a) and (b) and the color-scale changes in Fig. 5.2). In Fig. 5.4 (b) and (d), we plot as a function of displacement the conductances for samples #2 and #3 at large enough V that Coulomb blockade effects are negligible. For sample #3, for which the capacitance ratios indicated that only the molecule-drain distance changes significantly with displacement, the conductance decreases exponentially with distance, with a decay length approximately equal to that for bare Au junctions. For sample #2, for which we found from the capacitances that both the source and drain junctions change with displacement, the conductance change

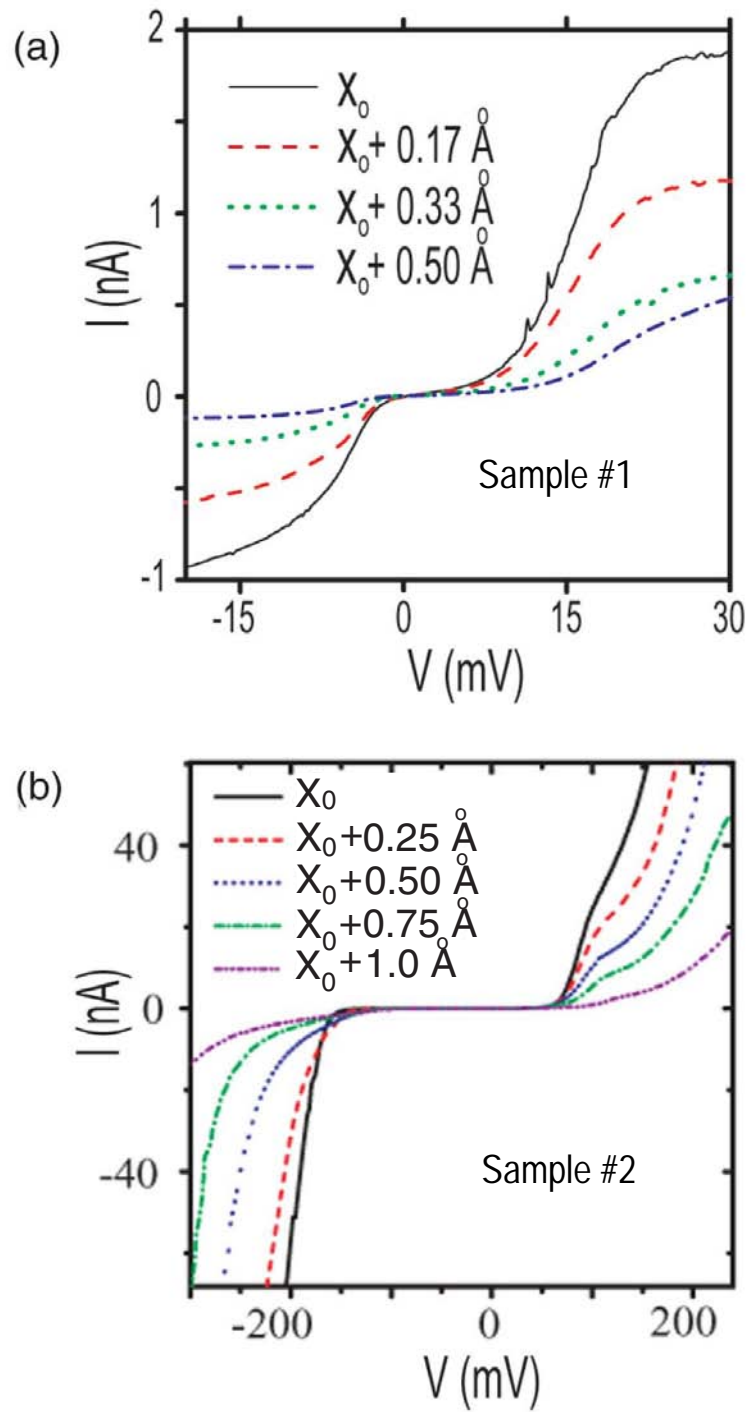


Figure 5.3: [$I - V$ characteristics] The dependence of $I - V$ characteristics has a function of mechanical displacement for (a) sample #1, (b) sample #2.

is not a single exponential and the rate of change is slower than for a bare Au junction. This is consistent with a situation in which the conductances of the two tunnel junctions are comparable and the motion is divided between both junctions. The information from gate-voltage measurements therefore provides an explanation for the different dependencies of the conductance on electrode displacement. Indeed, we can conclude that in sample #3 the C_{60} molecule is bound to the source electrode, while in sample #2 the C_{60} is more symmetrically bound to the two electrodes.

5.3.2 Changes in the gate voltage degeneracy point

A third type of change caused by the electrode displacement is perhaps less intuitive than the changes in capacitances and conductance: moving the source and drain electrodes can shift the gate voltage corresponding to the degeneracy point in the Coulomb blockade curves (see Fig. 5.2 (c) and (d) and Fig. 5.5 (a)). This effect demonstrates that the electrodes carry a charge even when $V = 0$, so that when they move, they perform work and shift the energy of the molecular states relative to the Fermi energy of the leads. Alternatively, we can think of the charge on the electrodes acting as a gate when the source and drain move with respect to the molecule. This effect is stronger in devices with a higher conductance. For sample #3 shown in Fig. 5.5 (b), the tunneling threshold V can be changed by as much as 25 mV by a displacement of 1.2 Å. A more dramatic effect is shown for another sample in Fig. 5.6, where the molecule's ground state degeneracy point can be reached by mechanical motion alone. Hence, these devices can exhibit transistor action controlled entirely by means of mechanical motion, as well as the ordinary electrostatic transistor action enabled by changing V_g . Related energy shifts have

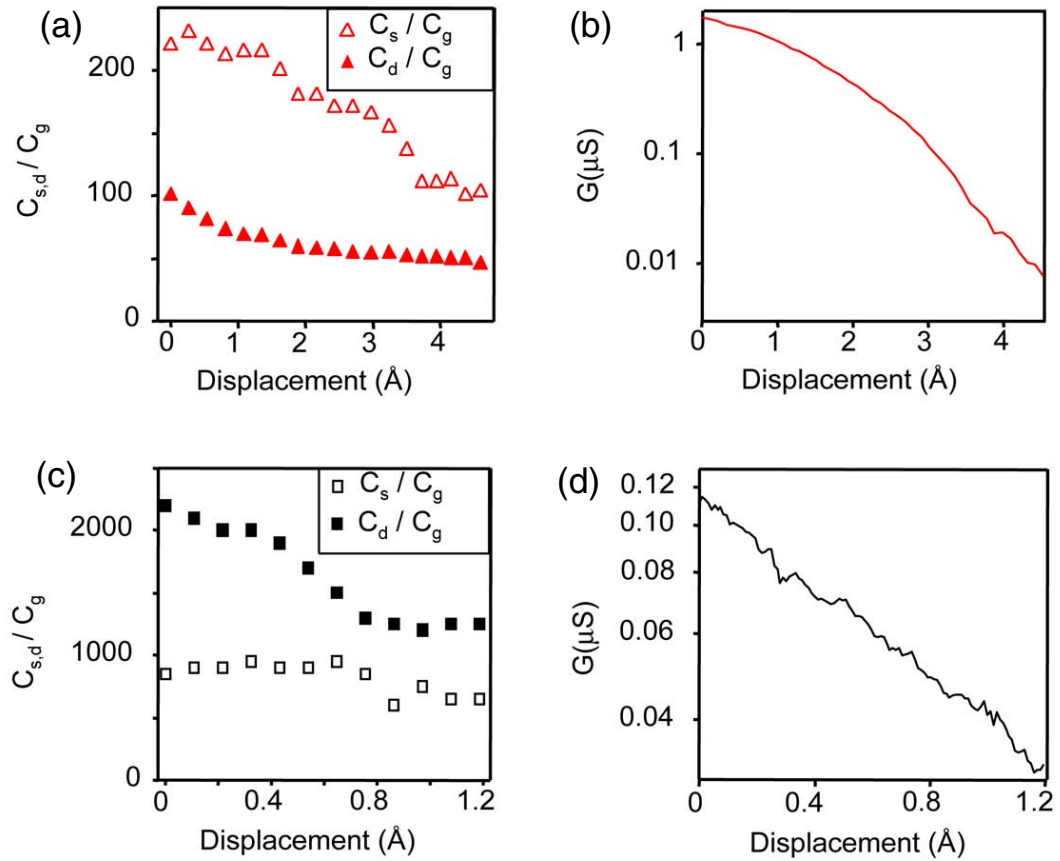


Figure 5.4: [Capacitances versus displacement] (a) and (c), capacitance ratios C_s/C_g and C_d/C_g versus displacement for respectively sample #2 and #3. (b) and (d), sample conductance $G = dI/dV$ versus source-drain displacement at large enough biases ($V = 235$ mV for sample #2, 150 mV for sample #3) that Coulomb blockade effects are not significant.

been seen in scanning tunneling microscope experiments on metal nanoparticles [18, 19], where it was suggested that they were related to a contact potential $\Delta\phi$ between the electrodes and the nanoparticle,

$$\Delta V_{\text{deg}} = \frac{\Delta\phi}{e} \left(\frac{\Delta C_s + \Delta C_d}{C_g} \right) \quad (5.2)$$

Our devices permit direct measurements of $(C_s + C_d)/C_g$, and we find that the measured values of V_{deg} would correspond to different values of $\Delta\phi$: -7 ± 5 mV for sample #1, 64 ± 3 mV for sample #2, and -29 ± 5 mV for a fourth sample. This means that V_{deg} is not determined only by an intrinsic work-function difference, but may also be influenced, for instance, by charged defects.

We have checked whether an applied gate voltage produces unwanted mechanical motion. A first indication that this deleterious effect is small can be seen in Fig. 5.2 (c) and (d). In these plots the Coulomb voltage thresholds are straight lines as a function of V_g up to 12 Volt. Since the slope of the voltage threshold is proportional to the capacitances of the device, we know that the capacitances are not strongly affected by V_g . We have shown that even a very small mechanical motion results in capacitance changes, thus we think that the gate voltage does not induce mechanical motion. Also, for both bare Au junctions and C_{60} devices with weak gate dependence, we have swept V_g in the range ± 12 V at fixed V and found less than 10% change in current, comparable to fluctuations due to charge rearrangements as we sweep V_g . Based on conductance versus displacement measurements on the same samples, this corresponds to an upper bound of 5 pm for V_g -induced displacements.

We did a simple calculation to estimate the motion of the electrodes due to gate voltage. We assumed a parallel plate capacitor to calculate the force between the

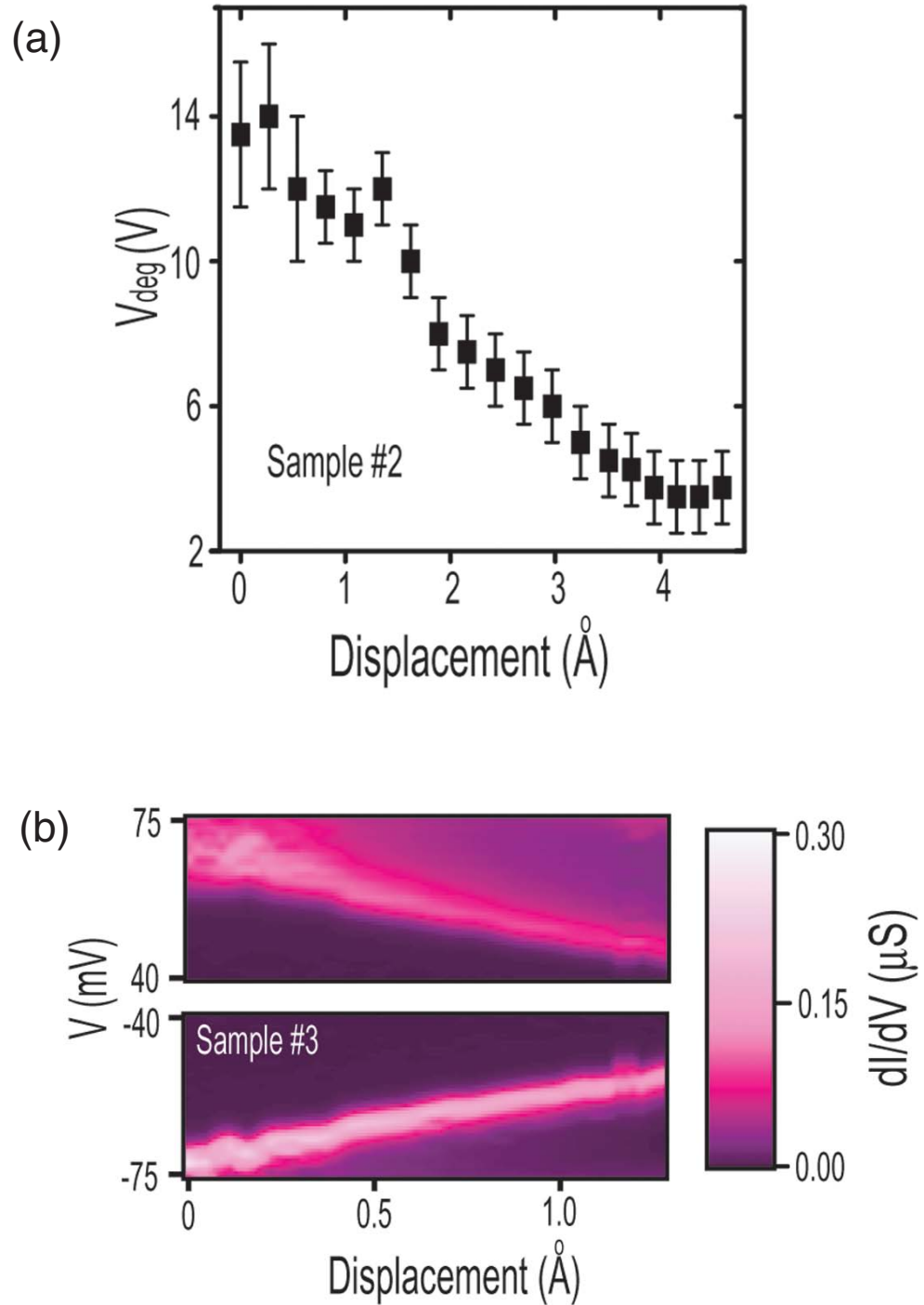


Figure 5.5: [Gate voltage degeneracy point] (a) V_{deg} as a function of mechanical motion for sample #2. (b) Color-scale plot of dI/dV versus V and source-drain displacement for sample #3, with $V_g = 0$.

bridge and substrate, and modeled the bridge as two triangular cantilever beams to obtain their spring constant¹. We find that the vertical motion of the bridge is about 4 Å and the increase in source-drain spacing is about 1.2 pm for a gate voltage of 12 V.

5.4 Conclusions

Our gated MCBJs provide the capability to make measurements on molecules with simultaneous tuning of both the spacing between electrodes (over a range of 5 Å) and the energy levels (by 160 meV on a C₆₀ molecule). We find that mechanical motion changes a molecule’s capacitances, conductance, and the Coulomb blockade degeneracy gate voltage. Gate voltage control permits detailed and mutually consistent characterizations of all three effects. We anticipate that this new experimental tool will enable systematic studies of fundamental questions such as how changes in molecular conformation affect electrical conduction, and how transport in molecules varies as one tunes between the weak-coupling Coulomb blockade and strong-coupling Kondo regimes [5]. The following chapter will detail our ongoing efforts to explore these questions.

¹The cantilever’s spring constant is: $k = \frac{1}{12} \frac{E_{Au} t^3 w}{L^3}$, where E_{Au} is the Young’s modulus of gold (110 GPa), w is the width of the base of the beam (200nm), t is the thickness (32 nm) and L is the length (250nm). The force on the beam is given by $F_Q = \epsilon_o A \frac{V^2}{d^2}$, where A is the cantilever area (25 000 nm²), V the gate voltage, and d the gate-bridge spacing (40nm).

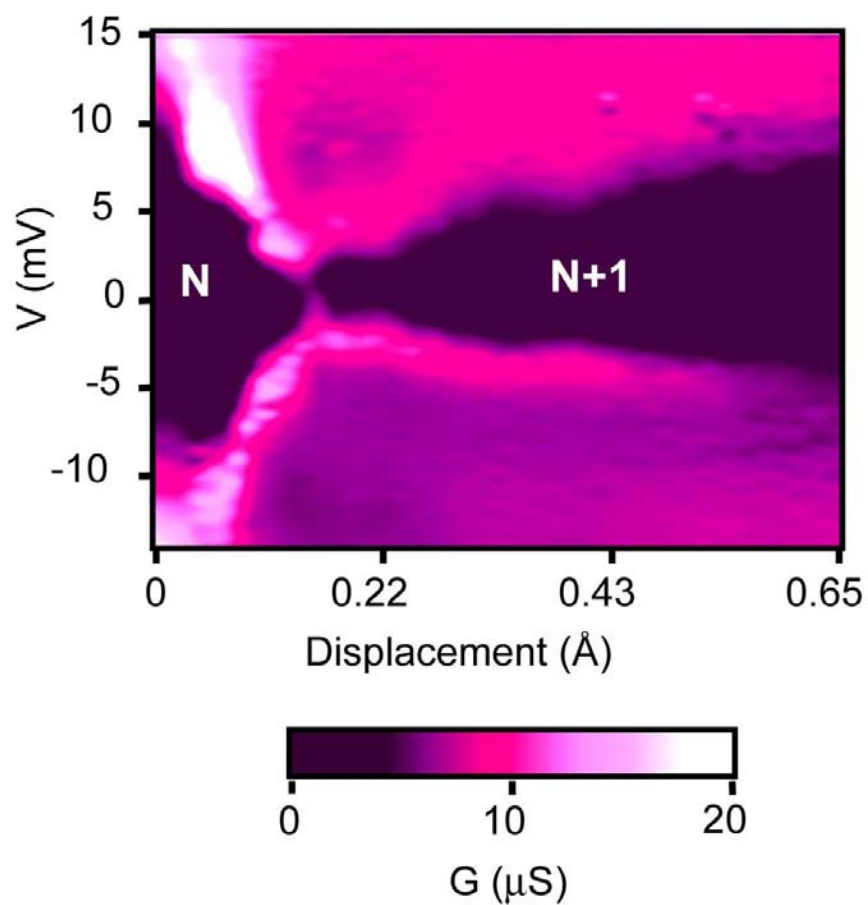


Figure 5.6: [Mechanically controlled transistor action] Color-scale plot of dI/dV versus V and source-drain displacement, with $V_g = 0$. The electron number on the molecule can be tuned by mechanical motion alone. This measurement was made at $T = 1.6$ Kelvin.

BIBLIOGRAPHY

- [1] A. Nitzan and M. A. Ratner, *Science* **300**, 1384 (2003).
- [2] J. R. Heath and M. A. Ratner, *Physics Today* **56**, 43 (2003).
- [3] C. N. Lau, D. R. Stewart, R. S. Williams, and M. Bockrath, *Nano Letters* **4**, 569 (2004).
- [4] H. Park et al., *Nature* **407**, 57 (2000).
- [5] J. Park et al., *Nature* **417**, 722 (2002).
- [6] W. J. Liang, M. P. Shores, M. Bockrath, J. R. Long, and H. Park, *Nature* **417**, 725 (2002).
- [7] L. H. Yu and D. Natelson, *Nano Letters* **4**, 79 (2004).
- [8] L. A. Bumm et al., *Science* **271**, 1705 (1996).
- [9] D. Porath, Y. Levi, M. Tarabiah, and O. Millo, *Physical Review B* **56**, 9829 (1997).
- [10] B. C. Stipe, M. A. Rezaei, and W. Ho, *Science* **280**, 1732 (1998).
- [11] X. D. Cui et al., *Science* **294**, 571 (2001).
- [12] M. A. Reed, C. Zhou, C. J. Muller, T. P. Burgin, and J. M. Tour, *Science* **278**, 252 (1997).
- [13] C. Kergueris et al., *Physical Review B* **59**, 12505 (1999).
- [14] R. H. M. Smit et al., *Nature* **419**, 906 (2002).
- [15] B. Q. Xu, X. Y. Xiao, and N. J. Tao, *Journal of the American Chemical Society* **125**, 16164 (2003).
- [16] A. R. Champagne, A. N. Pasupathy, and D. C. Ralph, *Nano Letters* **5**, 305 (2005).
- [17] A. N. Pasupathy et al., *Science* **306**, 86 (2004).
- [18] A. E. Hanna and M. Tinkham, *Physical Review B* **44**, 5919 (1991).
- [19] Z. Y. Rong, A. Chang, L. F. Cohen, and E. L. Wolf, *Ultramicroscopy* **42**, 333 (1992).

Chapter 6

Other experiments with g-MCBJs and outlook

In this chapter we discuss ongoing projects involving gated-mechanically adjustable break-junctions (g-MCBJs). These experiments will greatly benefit from the added functionality of the new measurement apparatus we just built (see section 4.3). I initiated these experiments, but as I graduate, some of them will be continued by Josh Parks. He is the one who acquired the data shown in section 6.1. All of the experiments discussed here are in their early stages, but seem to be within our experimental reach.

6.1 Kondo physics in single-molecule transistors

When a molecular quantum dot is strongly coupled to two leads it is possible for electrons to tunnel coherently across it. One such coherent tunneling process is the Kondo effect. The Kondo effect in a quantum dot manifests itself as a conductance resonance (a peak in dI/dV) at zero bias voltage (instead of Coulomb blockade). It generally arises in dots with an unpaired electron (spin $1/2$), where the unpaired electron spin scatters, via a higher-order process, electrons from the Fermi sea of one lead into the other (see Fig. 6.1). It has been observed in metallic point contacts [1], semiconducting quantum dots [2], carbon nanotubes [3], and single molecules [4, 5, 6]. A detailed discussion of the Kondo effect can be found in reference [7].

The experimental technique of g-MCBJ is ideally suited to study the Kondo

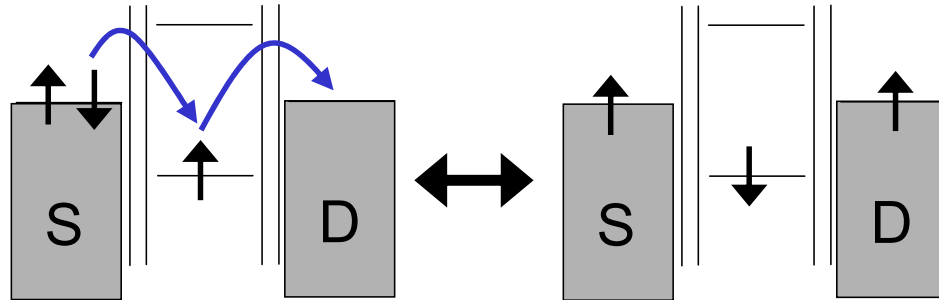


Figure 6.1: [Kondo assisted tunneling] Cartoon showing a two-step coherent tunneling event contributing to the Kondo effect in a spin-1/2 degenerate quantum dot.

effect in single-molecules for the following reason. The Kondo resonance’s strength (characterized by a “Kondo temperature” T_K) depends strongly on the electrode-molecule coupling strength (Γ), and the molecule charging energy U ,

$$T_K = \frac{\sqrt{\Gamma U}}{2} \exp\left(\pi \epsilon_o \frac{\epsilon_o + U}{\Gamma U}\right) \quad (6.1)$$

where ϵ_o is the energy of the level on the dot occupied by the unpaired electron. We have shown in chapter 5 that we can tune Γ , U , and ϵ_o in our devices. We therefore expect that we should be able to tune, via mechanical motion and gate voltage, the Kondo temperature or amount of coherent tunneling in the dot.

We have observed zero-bias conductance peaks in g-MCBIJ devices incorporating either C_{60} molecules or $[\text{Co}(\text{tpy-SH})_2]^{2+}$ molecules. Other experiments in electromigration break-junctions have characterized the Kondo effect in similar devices [5, 6]. Figures 6.2, 6.3, and 6.4 present data on the first Co-tpy device that we have fully characterized. The measurements were made at a temperature of 1.6 Kelvin, using an AC lock-in technique to reduce the noise level. Surprisingly, the data shown in these figures is not consistent with a spin-1/2 Kondo effect, but rather seems to point to a spin-1 Kondo effect. Similar data was observed before by Ahbay Pasupathy [8]. Integer spin Kondo resonances have been reported in semiconducting [9] and carbon nanotube dots [10]. The nature of the spin-1 state in our molecule is unknown [8], but may be due to two or more molecules participating in the electronic transport. In a spin-1 Kondo dot, two states (say, singlet and triplet) can provide a path for electrons to tunnel resonantly through the dot at low bias. The data shown here have not been analyzed yet, but we will give a brief description.

Figure 6.2 (a) shows the evolution of the zero-bias anomaly with mechanical

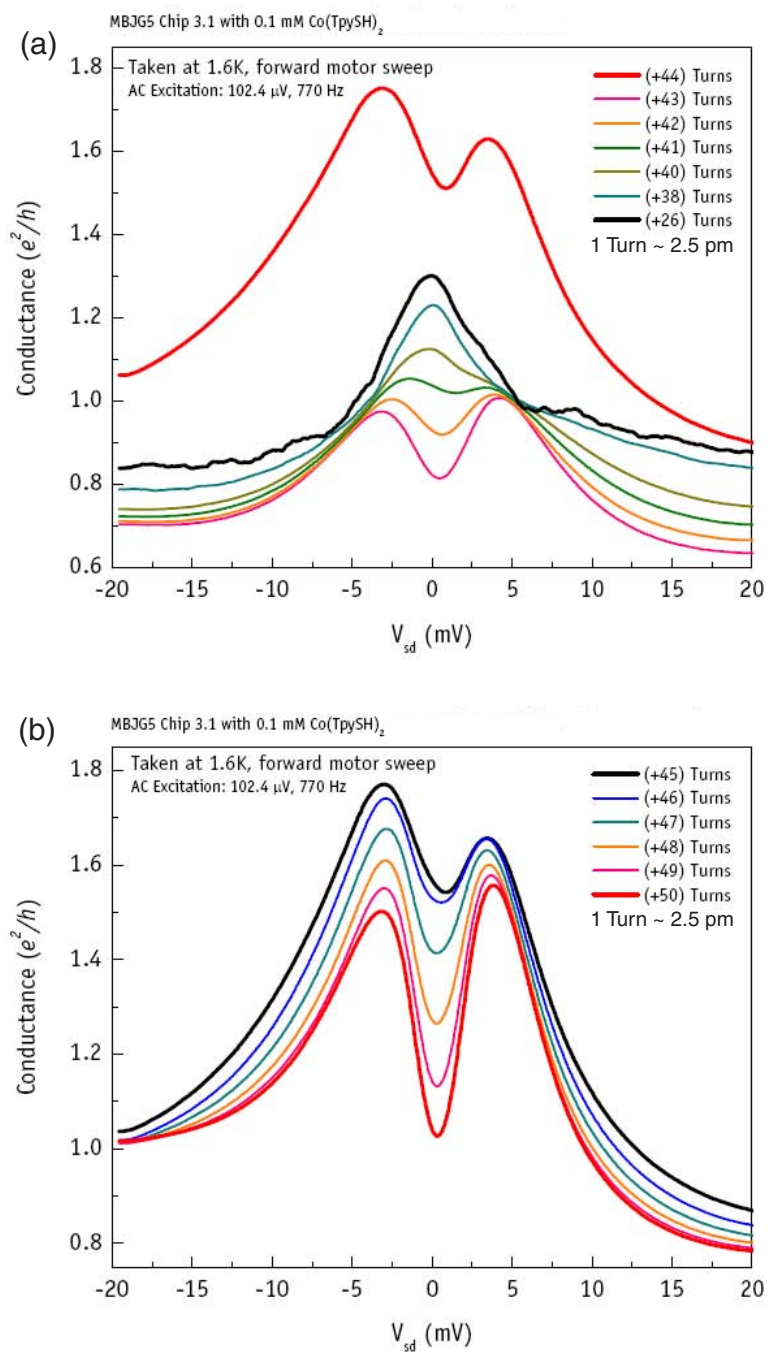


Figure 6.2: [Mechanical tuning of the Kondo resonance] (a) The evolution of the zero-bias anomaly under mechanical tuning of the source-drain electrodes' spacing. A shift in background charge caused an offset in the last curve. (b) Continuation of (a) after the shift in background charge.

displacement. The resonance starts as a single peak (position 1) and splits into two (position 2). The last curve shows a sharp jump in conductance that we associate with a jump in background charge. Figure 6.2 (b) shows the continuation of panel (a) after the shift in background charge. The resonance continues to split further apart into two well resolved peaks. It is possible that the dominant effect of tuning the source-drain distance is to change the electrostatic potential of the molecule since it was shown in section 5.3.2 that, in high-conductance samples, mechanical motion acts as a gate. Some analysis will be necessary to disentangle how much of the effect seen in Fig. 6.2 is due to a tuning of Γ and U via mechanical motion, and how much is due to a gating effect (tuning of ϵ_0).

One of the signatures of the Kondo effect is that when the degeneracy of the spin levels on the dot is lifted by a magnetic field, it leads to a splitting of the resonance. Figure 6.3 (a) and (b) show the magnetic field dependence of the resonance, respectively at mechanical positions 1 and 2. The g -factor extracted from panel (a) is close to 2, if we assume $S = 1$, and 4 if we assume $S = 1/2$. The behavior of the split resonance in panel (b) is consistent with the spin-1 picture [11, 12].

Another important feature of the Kondo resonance is that the height of the resonance decays logarithmically with increasing temperature. Figure 6.4 shows the temperature dependence of the conductance maximum at both mechanical positions 1 in (a) and 2 in (b). Again the data seems consistent with the spin-1 picture [11].

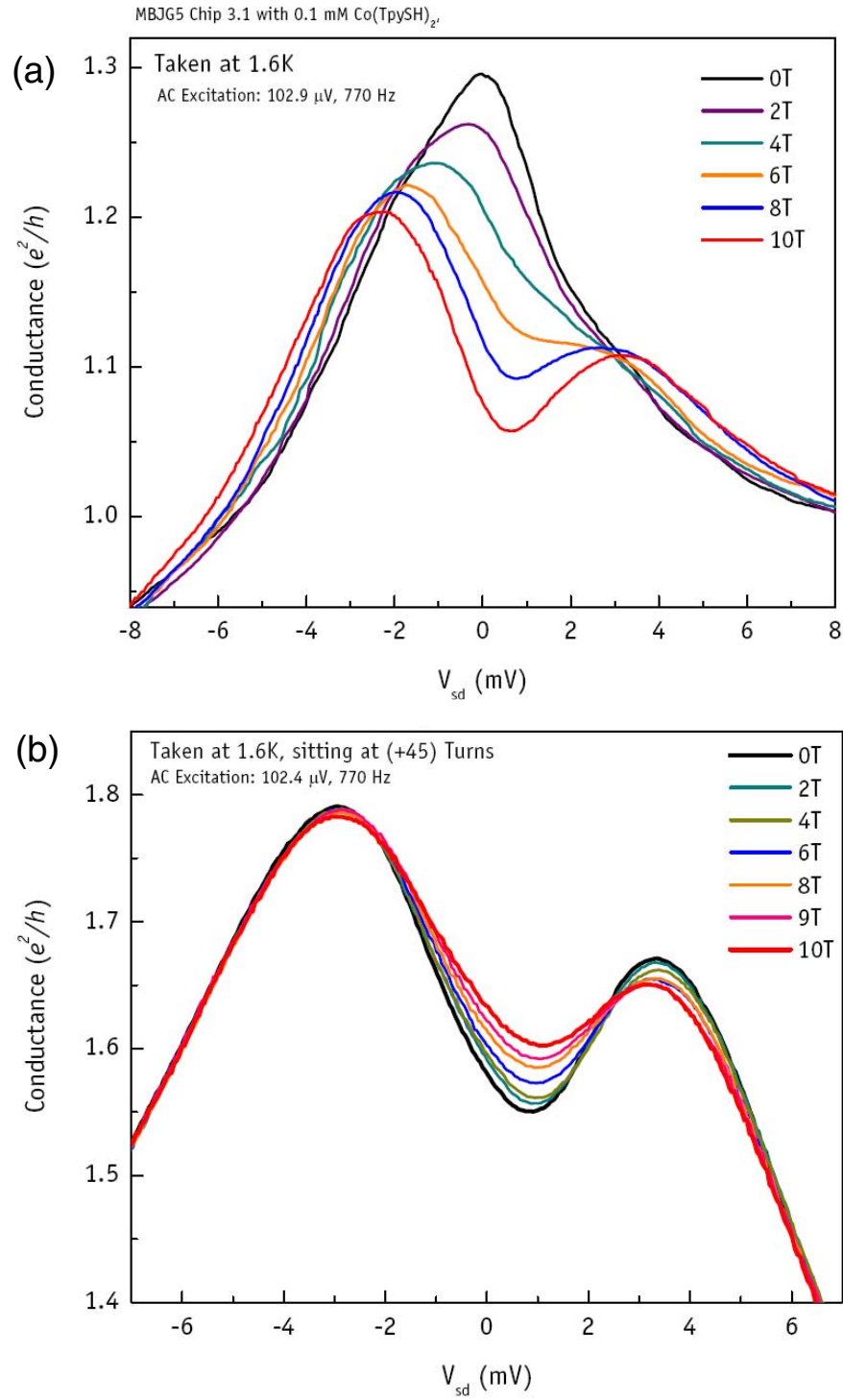


Figure 6.3: [Magnetic field dependence of the Kondo resonance] (a) B-field dependence of the single-peak resonance (source-drain position 1). (b) B-field dependence of the split resonance (source-drain position 2).

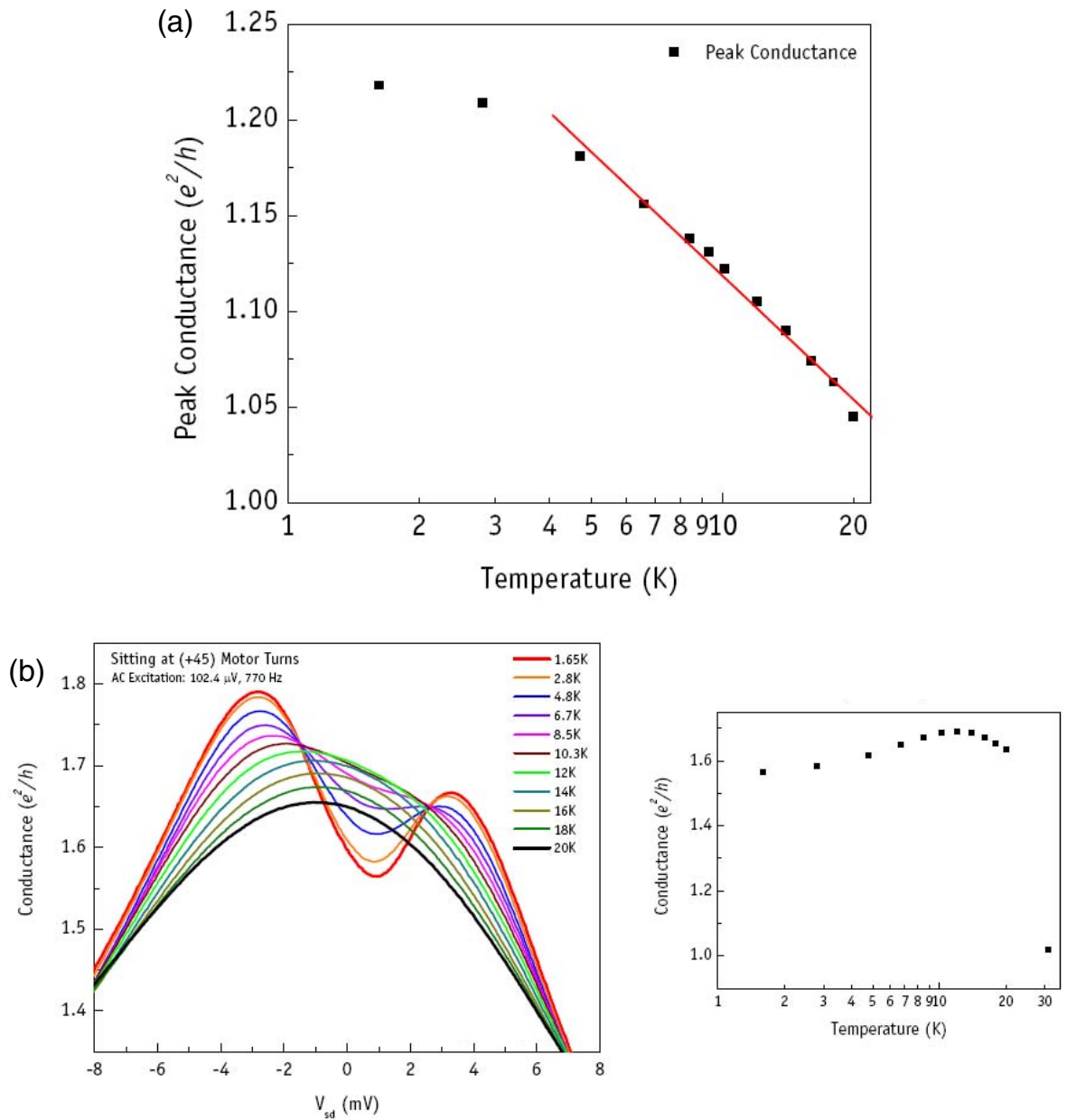


Figure 6.4: [Temperature dependence of the Kondo resonance] (a) Temperature dependence of the single-peak zero-bias resonance (at source-drain position 1) (b) Temperature dependence of the split resonance (source-drain position 2). The right hand side plot shows the conductance extracted from the left hand side plot at the position of the valley between the two peaks.

6.2 Vibrational energy levels in single molecules

Recent theoretical papers [13, 14, 15] have discussed the effect of the lead-molecule coupling on the electron-phonon coupling in a molecular SET. In single C_{60} devices (see Fig. 6.5 (a)), we have observed two excited energy levels of the molecule (see Fig. 6.5 (b) and (c)). These modes have been observed previously [16], and associated with two vibrational modes of the molecule. We hope to study how these modes (and the ones in other molecules) evolve as we either deform the molecule, or change its coupling to the leads.

6.3 Short carbon nanotubes

Carbon nanotubes (Fig. 6.6 (a)) are perhaps the most exciting molecules in physics [17]. We are interested in probing carbon nanotubes in our g-MCBJs. As a first experiment, we intend to study how the band structure of the tubes change as they are strained [18].

Figure 6.6 shows nanotube devices that were fabricated following the recipe described in chapter 3. Figure 6.6 (b) shows a single carbon nanotube wire-up between two Au electrodes spaced 100 nm apart. The nanotube is suspended above the substrate (a back-gate) and can be pulled apart by bending the substrate. Figure 6.7 (a) shows Coulomb oscillations measured in one such device. Although some faint effects of mechanical strain were recorded in these devices, it is clear that the amount of strain we can apply in this geometry ($< 1\%$) is too small for our purpose. Thus, we made devices like the one shown in 6.6 (b), where a nanotube is buried under a Au break-junction. Using electromigration, we can expose a very short section of the tube ($\approx 10\text{-}20$ nm at room temp) that can then be strained

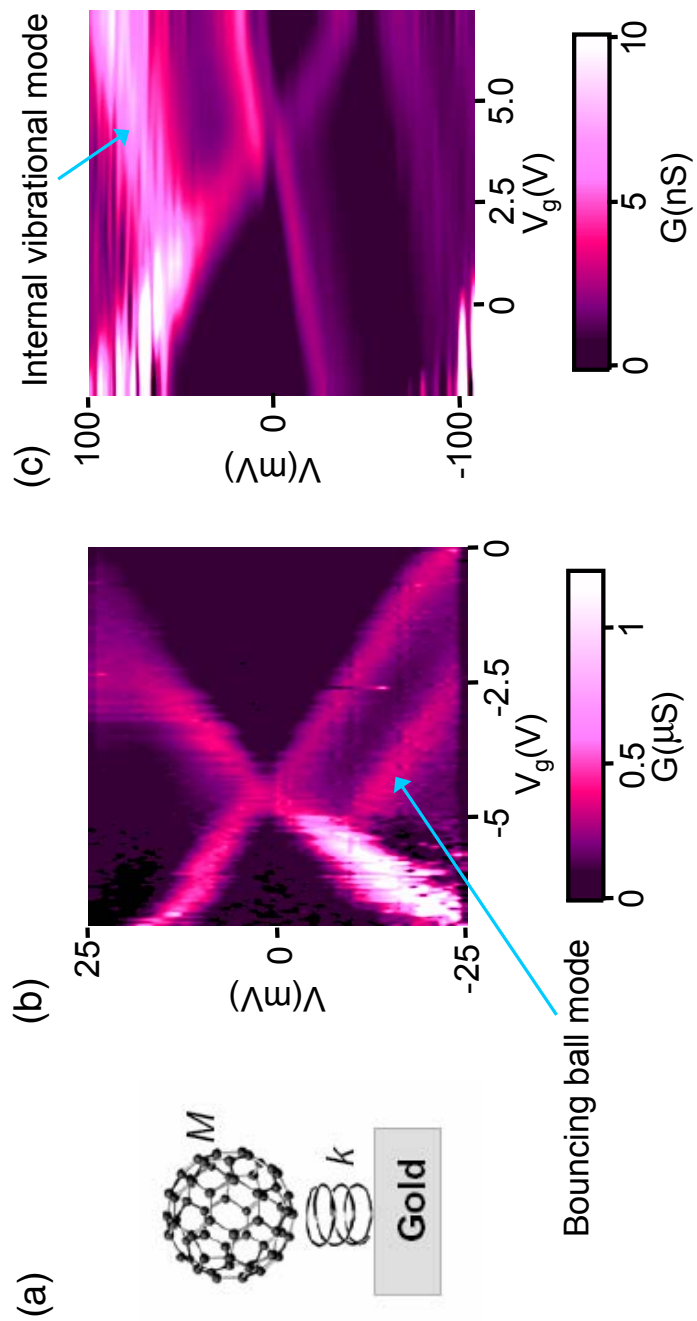


Figure 6.5: [Vibrational modes in C₆₀] (a) Cartoon of a single C₆₀ molecule bound to a Au surface by van der Waals interaction. (b) Data showing a ≈ 7 meV bouncing mode of C₆₀ molecule. (c) Data showing a ≈ 40 meV internal vibrational mode of a C₆₀ molecule.

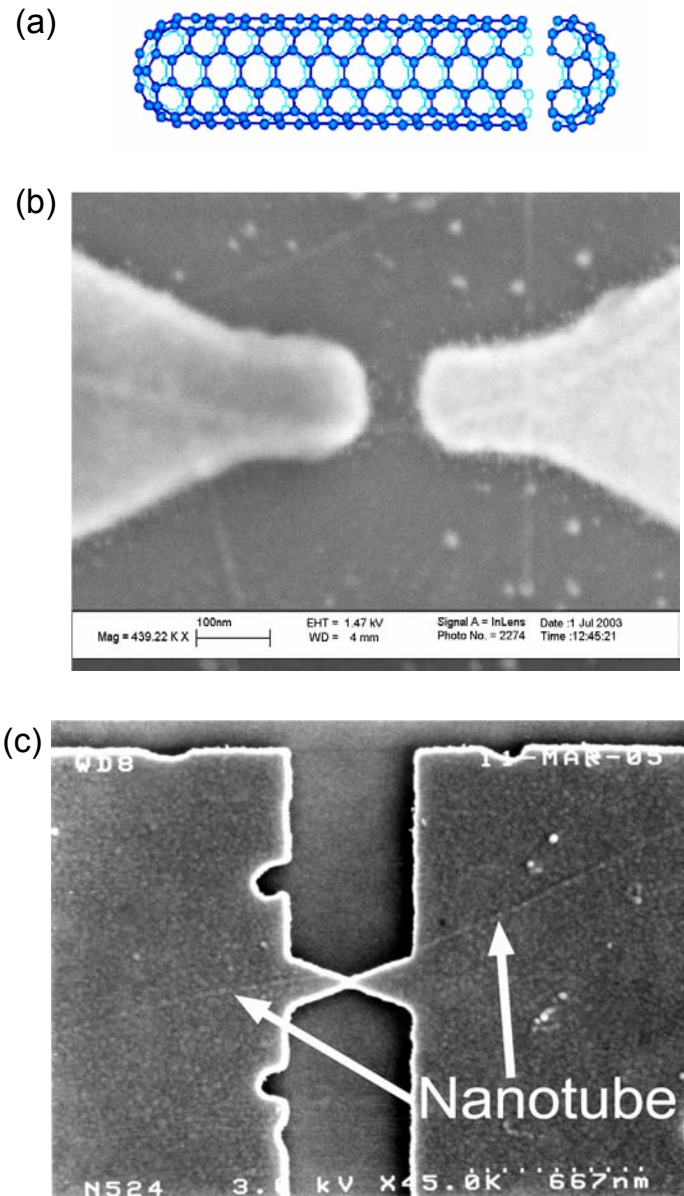


Figure 6.6: [Carbon nanotube g-MCBI] (a) A cartoon of a single wall carbon nanotube. (b) A suspended carbon nanotube in a 100-nm gap junction. (c) A single nanotube in a g-MCBI.

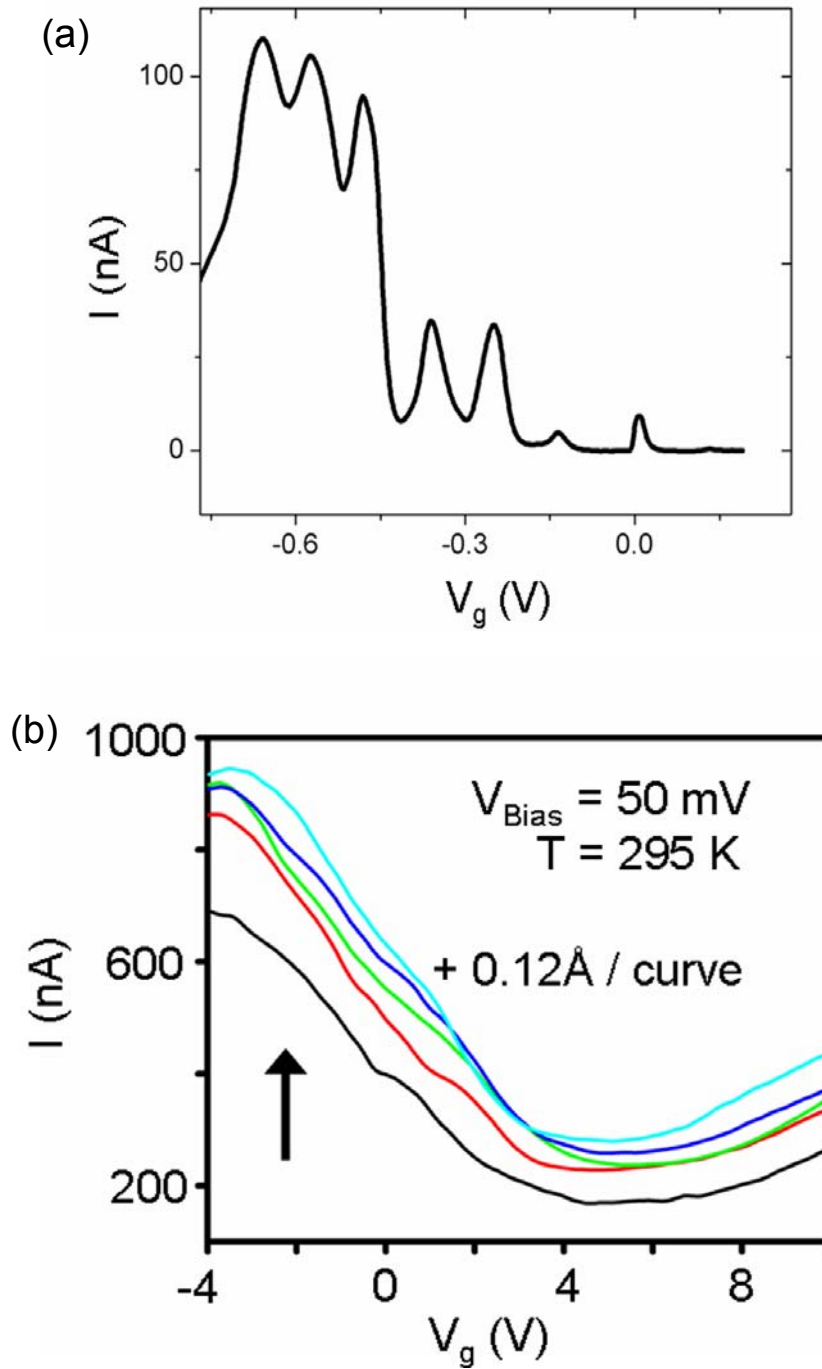


Figure 6.7: [Carbon nanotube tuning] (a) Gate-induced Coulomb oscillation in a 100 nm-gap junction carbon nanotube. (b) Modulation of the band gap of a semiconducting nanotube in a g-MCBJ at room temperature.

up to a few %. Figure 6.7 (b) shows data taken at room temperature for one of these devices. We can see a small modulation of the semiconducting band-gap as a function of the applied strain. The fabrication of these devices needs to be optimized to achieve a higher yield, if these studies are to be successful.

6.4 Metallic dots

The g-MCBIJ technique we developed is not limited to studying organic molecules. It can also be used to study nanograins of metal. Figure 6.8 (a) shows a metallic-dot g-MCBIJ device. The device is an electromigrated iridium bridge on top of which Au particles were evaporated following a recipe developed by Kirill Bolotin and Ferdinand Kuemmeth [19]. Iridium was selected as a material because it produces small gaps when electromigrated at room temperature. Figure 6.8 (b) shows an $I - V$ characteristic of a device taken at 4.2 Kelvin (acquired by Ferdinand Kuemmeth). Experiments to probe the dependence on the source-drain spacing of magnetoresistance and spin-blockade in ferromagnets are being pursued by Kirill Bolotin.

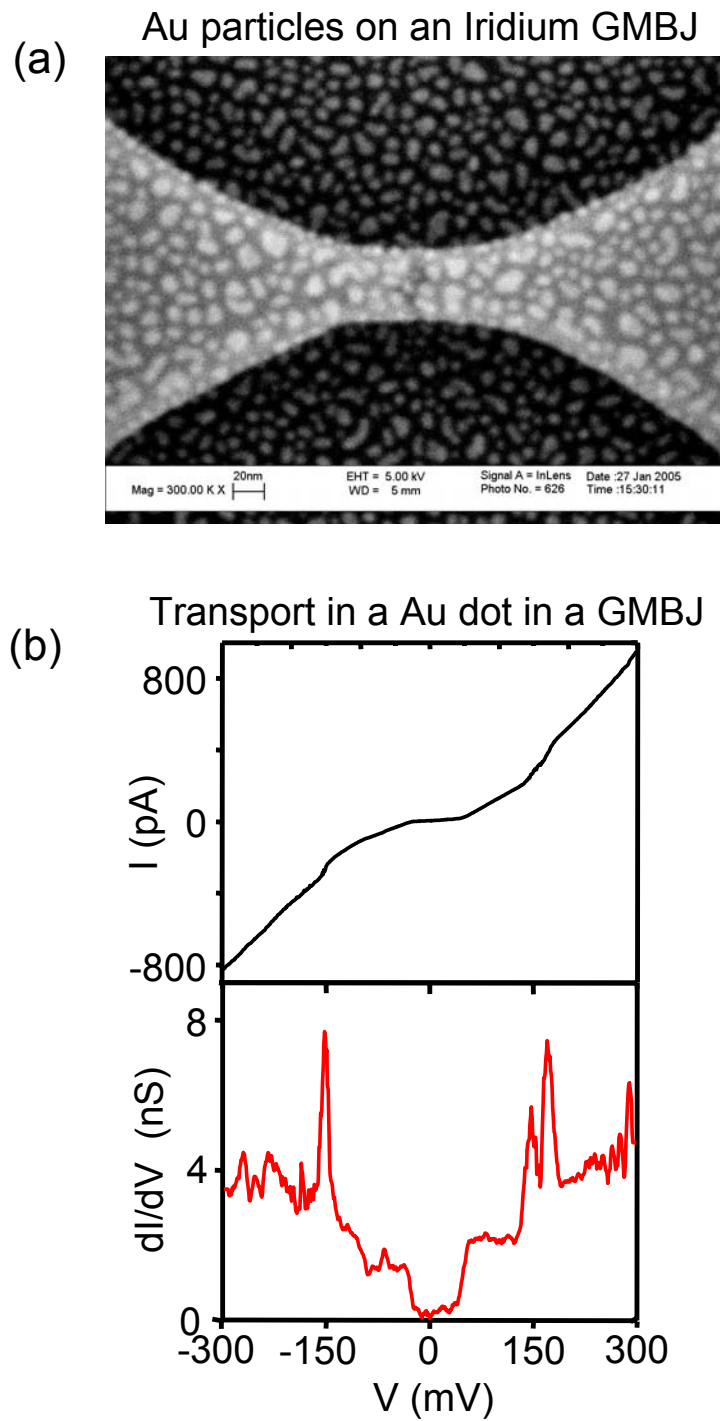


Figure 6.8: [Metallic particles in g-MCBJs] (a) An SEM image of an electromigrated Ir g-MCBJ, on top of which Au nanoparticles were evaporated. (b) $I - V$ characteristics of a device similar to the one in (a).

BIBLIOGRAPHY

- [1] D. C. Ralph and R. A. Buhrman, *Physical Review Letters* **72**, 3401 (1994).
- [2] D. Goldhaber-Gordon et al., *Nature* **391**, 156 (1998).
- [3] J. Nygard, D. H. Cobden, and P. Lindelof, *Nature* **408**, 342 (2000).
- [4] W. J. Liang, M. P. Shores, M. Bockrath, J. R. Long, and H. Park, *Nature* **417**, 725 (2002).
- [5] J. Park et al., *Nature* **417**, 722 (2002).
- [6] A. N. Pasupathy et al., *Science* **306**, 86 (2004).
- [7] G. Gruner and A. Zawadowski, *Report on Progress in Physics* **37**, 1497 (1974).
- [8] A. N. Pasupathy, PhD thesis, Cornell University, 2004.
- [9] B. Su, V. J. Goldman, and J. E. Cunningham, *Surface Science* **305**, 566 (1994).
- [10] S. Sasaki et al., *Nature* **405**, 764 (2000).
- [11] W. G. v. d. Wiel, S. D. Franceschi, J. M. Elzerman, S. Tarucha, and L. P. Kouwenhoven, *Physical Review Letters* **88**, 126803 (2002).
- [12] P. Jarillo-Herrero, J. Kong, H. S. J. v. d. Zant, C. Dekker, and L. P. Kouwenhoven, *cond-mat/0504059* (2005).
- [13] S. Braig and K. Flensberg, *Physical Review B* **68**, (2003).
- [14] S. Braig and K. Flensberg, *Physical Review B* **70**, (2004).
- [15] Z. Z. Chen, R. Lu, and B. F. Zhu, *Physical Review B* **71**, (2005).
- [16] H. Park et al., *Nature* **407**, 57 (2000).
- [17] C. Dekker, *Physics Today* , 22 (1999).
- [18] E. D. Minot et al., *Physical Review Letters* **90**, 156401 (2003).
- [19] K. I. Bolotin, F. Kuemmeth, A. N. Pasupathy, and D. C. Ralph, *Applied Physics Letters* **84**, 3154 (2004).

Chapter 7

A custom Atomic Force Microscope (AFM) for fabricating high-resolution scanning probes

7.1 Introduction

In section 1.3 we briefly reviewed the principles of atomic force microscopy (AFM) and how it can be used to measure the topography of a surface with nanometer-scale spatial resolution. We also mentioned how an AFM tip can be “functionalized” by adding nanostructures at the apex of the tip to measure other physical quantities (so called scanning-probe microscopy (SPM)) on the surface, such as the magnetic field, electrostatic field, the density of energy levels, etc ... In order to achieve high sensitivity and spatial resolution measurements of the interactions between these SPM sensors and structures of interest, it is necessary to build very small structures at the end of AFM tips.

In this chapter we discuss the machinery built to implement a method to fabricate SPM sensors on AFM tips using nanofabricated stencil masks [1, 2, 3]. The fabrication of devices on the sharp apex of an AFM tip presents a challenge since standard lithographic processes require flat substrates. In section 7.1.1 we give an overview of a few methods that have been used in the past to fabricate high-resolution SPM sensors (also referred to as SPM tips). We argue the need for a new fabrication method in order to build structures with a feature size below 100 nm on AFM tips. In section 7.1.2 we describe a stencil mask method (see Fig.

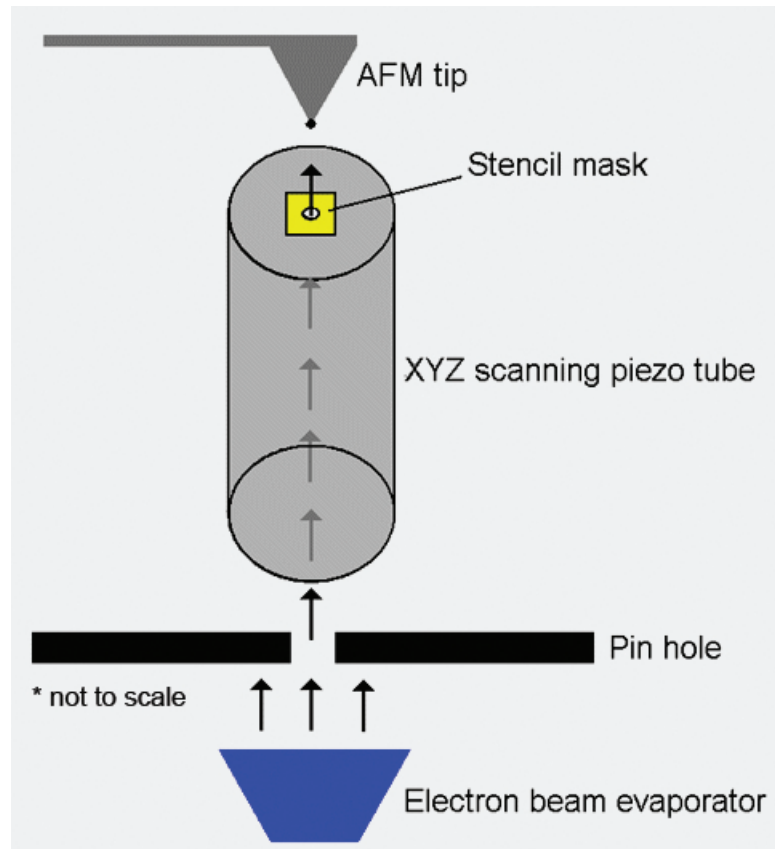


Figure 7.1: [Stencil mask lithography] A cartoon of how to use stencil mask evaporation to build high resolution sensors at the end of AFM tips.

7.1) that we have developed to achieve lithography on AFM tips with a feature size down to 10 nm.

The main body of the chapter is section 7.2 where the different apparatus and technologies developed to implement the technique are described. Namely, we built a customized atomic force microscope (AFM) that can be operated inside an evaporation chamber. Aaron Couture and the author made equal contributions to the work reported in this chapter.

7.1.1 Review of some fabrication processes used to make scanning probes

Here we give an overview of a few state-of-the-art methods to fabricate high-resolution SPM probes. This overview is very far from exhaustive and only intends to provide the reader with the background necessary to appreciate the motivation to develop a new fabrication technique for SPM tips. After this overview, we hope that it will be clear to the reader that there is a need for a technique that would allow us to: fabricate any kind of SPM tip, rather than only one type like most other techniques, and achieve a minimum feature size of 10 nm, as opposed to the ≈ 100 nm possible by other methods.

Although it is difficult to write directly onto AFM tips using electron-beam lithography, it is not impossible. At least one research group [4] has developed the technology to do high-resolution (> 50 nm) direct e-beam lithography on the top of **flat** AFM tips (See 7.2). The first challenge they overcome is the impossibility to “spin” resist on a tip. instead of spinning, they use a “float coating” technique where a solid film of resist is deposited on the tip by evaporating a water film on which the resist is floating. The alignment on the tip is also difficult because tips

are defined by a wet etch that yields large tip to tip variation in position. They solve this problem by fabricating their own tips and etching alignment marks at the same time the tips are etched. Still, in order to be successful they need a large flat region ($\approx 1 \mu\text{m}^2$) at the top of the tip where they can build their devices. This flat area has some serious drawbacks for imaging a surface.

A flat tip is very poor at imaging rough surfaces and has low topographical imaging resolution (AFM imaging). Since these tips cannot acquire a high-resolution topographical image simultaneously with the SPM imaging, it will be very difficult to disentangle the van der Waals force contribution from the SPM signal resulting in poor “functional” imaging resolution. The advantage of this technique over some of the other ones [5, 6, 7] is that it can build any type of devices at the end of a tip rather than a single type. In Fig. 7.2 taken from [4], a 100 nm junction Hall probe magnetometer is shown in (a), a single-turn electromagnetic coil (for magnetic field sensing) is shown in (b) and (c), and a metal (Pd) constriction serving as a heater and temperature sensor is shown in (d).

To fabricate small devices at the end of sharp AFM tips, one must use non-standard fabrication methods. To the extent of the author’s knowledge, no one such method (except the one to be introduced later in this chapter) allows the transfer of a pattern of arbitrary shape onto the end of a tip. Nevertheless, many impressive devices have been built. Here we restrict our attention to two types of devices, namely magnetic force microscopy (MFM) tips and gated scanning tunneling microscope tips (g-STM). Figure 7.3 (a) shows a method to build MFM tips developed in [6]. Their fabrication process involves depositing a carbon mask at the apex of a tip coated with a magnetic film and subsequently etching the magnetic film away, leaving only the portion covered by carbon. This method can

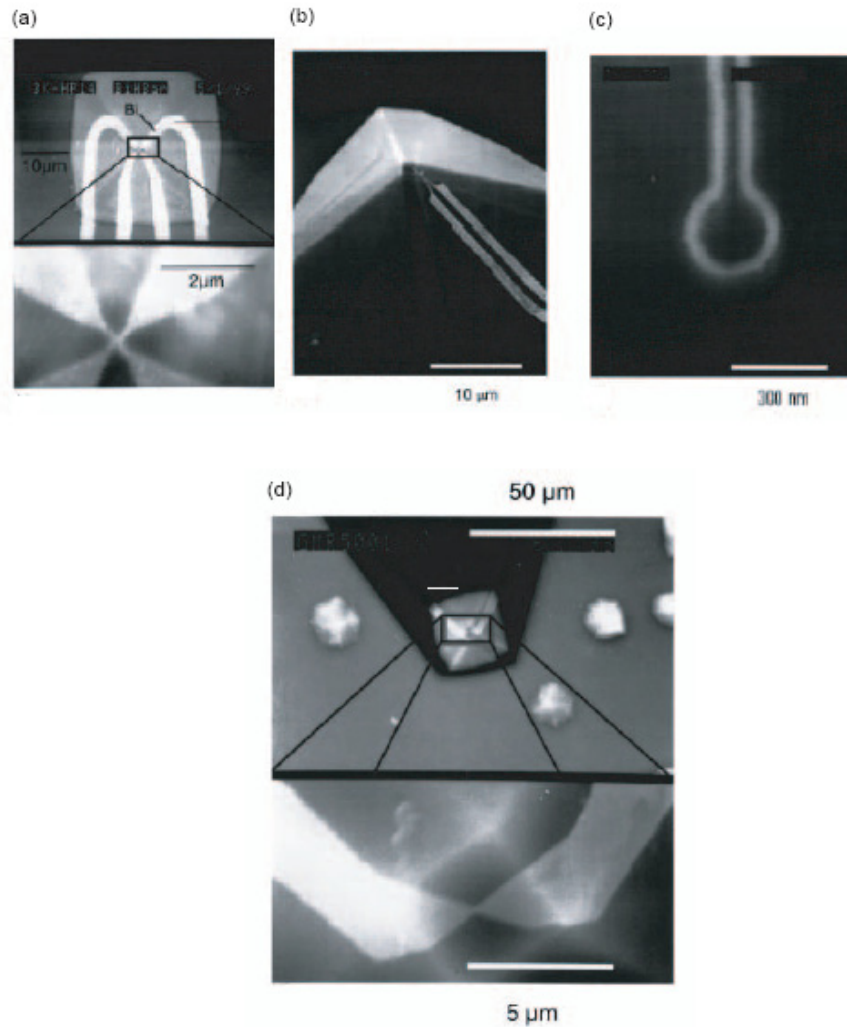


Figure 7.2: [E-beam lithography on AFM tips] Taken from [4] (a) A 100 nm junction bismuth Hall probe magnetometer fabricated on a blunt silicon AFM tip. (b) An electromagnetic Hall probe consisting of a single-turn coil at the apex of a tip. (c) Close-up of (b). (d) A constriction in a Palladium wire at the apex of a tip which can serve as a heating element and a thermometer.

confine the magnetic moment on the tip to a region down to about 50 nm in diameter (Fig. 7.3 (b)). Although this experiment did not demonstrate high-resolution imaging, another experiment with a similar approach has shown a magnetic signal spatial resolution in 2-d down to 37 nm [5].

In Fig. 7.3 (c) a g-STM tip built by Gurevich *et al.* [7] is shown. These tips are fabricated from a Si wafer on which a “sandwich” $\text{SiN}_x\text{-SiO}_2\text{-SiN}_x$ film is grown. The wafer is back-etched leaving the sandwich film freely suspended. The edges of the suspended thin films of SiN_x act as the gate and tunneling electrodes, while the SiO_2 film acts as an insulating spacer. Building this device is much more involved than building an MFM sensor since it is necessary to build two active elements (tip and gate) as well as electrical connections from the tip to the outside world. Because of these requirements the fabrication imposes restrictions on the tip-gate spacing. The tip-gate spacing achieved in ref. [7] is to our knowledge the smallest in literature, but is still in excess of 200 nm. This distance seriously limits the amount of gate coupling available, therefore limiting the spectroscopic measurements on the sample. Another drawback of the device is that it is a non-standard tip (not a floppy cantilever) which may limit its compatibility with commercially available microscopes.

While many of the SPM sensors that have been built are impressive, high-resolution functional probes are still confined to proof of principle experiments because of their numerous limitations. We would like to develop a technique to fabricate SPM probes that would consistently produce **practical** high-resolution probes. In short we would like to develop a fabrication technique that would allow us to build devices:

1. of any kind (shape or size)

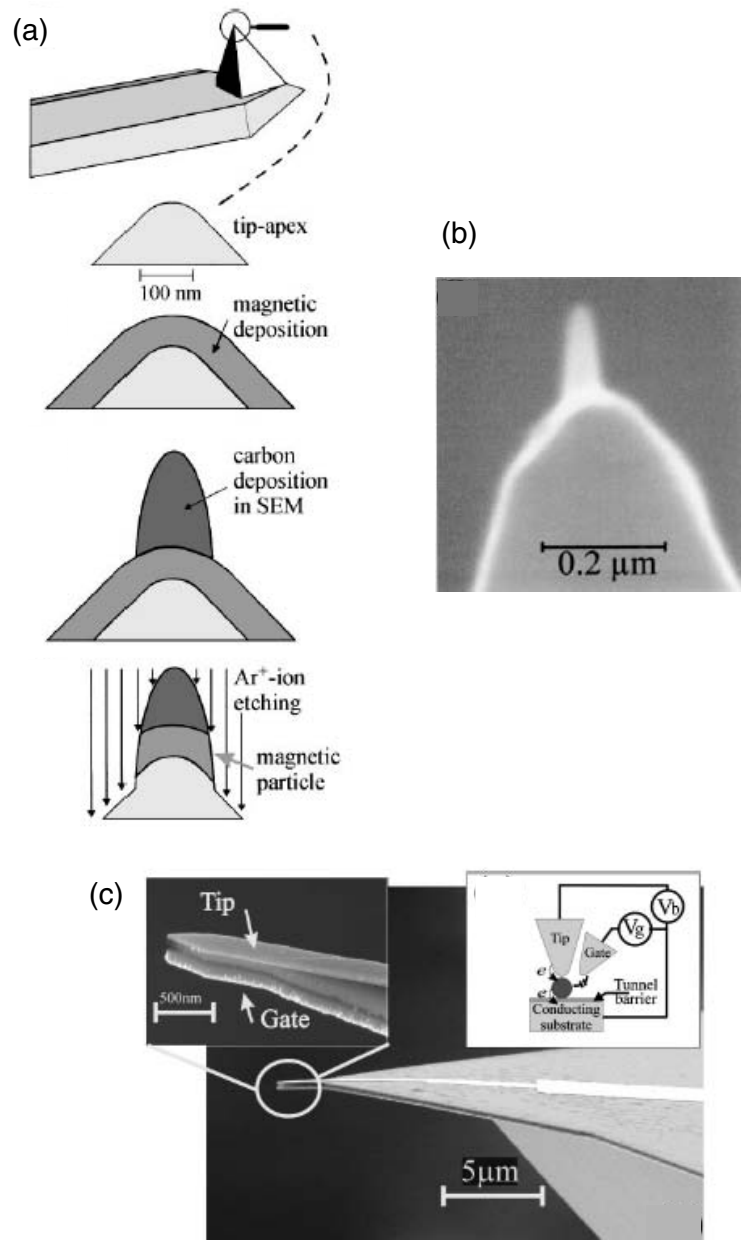


Figure 7.3: [Other SPM tips fabrication methods] (a),(b) Taken from [6]. (a) Fabrication steps to build MFM tips where the magnetic film is confined down to a diameter of 50 nm. A tip made this way is shown in (b). (c) Taken from [7], shows a gated-STM tip with a ≥ 200 nm tip-gate spacing.

2. at the end of sharp AFM tips
3. with a small minimum feature size $\ll 100$ nm
4. on commercially available tips (for compatibility purposes)

7.1.2 Pattern transfer on AFM tips using a stencil mask: technical requirements

In this section we discuss what is required to implement the stencil lithography technique shown in 7.1 while satisfying the four requirements listed above.

The first obvious need is to built an AFM assembly that will be able to do imaging inside a metal evaporation system. This means that the vibrational isolation of the assembly needs to filter out all the vibrations arising from the pumping system (cryo-pump) of the evaporator. It is essential to maintain a good alignment between the AFM tip and the stencil mask during the evaporation. Thus, care must be taken to ensure minimal thermal drift of the scanning assembly due to the heat associated with the electron-beam melting the metallic source. Another concern is to shield the AFM from the electronic noise generated by the electron-beam used to melt the source. This is not an easy task considering that the beam is in close proximity to the AFM wiring and the beam current and voltage are respectively 100s of mA and several kV.

The feedback mechanism of an AFM usually relies on a laser beam bouncing from the backside of the AFM tip. Using interferometry, it is then possible to measure the vertical displacement of the tip. The main difficulty with this method is to ensure proper alignment of the laser with the tip while moving the microscope in and out of the evaporation system. Vibrational isolation and thermal drift are

also concerns for a laser feedback. To avoid these problems we monitor the tip-sample distance by making use of a tuning fork feedback system. This only requires us to track the current flowing in a quartz tuning fork to which the tip is mounted. Details concerning the tuning fork feedback mechanism will be given in section 7.2.3. The challenge with a tuning fork feedback is to optimize the tuning fork and tip mounting so as to achieve the large quality factor necessary for imaging. It is also important to be able to dismount the tip from the tuning fork without damaging it, so that the tip can subsequently be used in other microscopes.

The subject of the following section is to describe the AFM, tuning fork feedback and electronics that were built to meet the above requirements.

7.2 Instrument design

The first step in designing the microscope is to decide which evaporation chamber it will fit in. A picture of the evaporation system and a drawing of the evaporation chamber we use are shown in 7.4 (a),(b). We first describe the characteristics of the chamber itself, then turn to the microscope, and finally discuss the electronics needed to operate it.

7.2.1 The evaporation system

The evaporation chamber (see Fig. 7.4) is cryo-pumped and has a base pressure in the low 10^{-8} Torr range. The chamber was modified to host the microscope. A top flange of 9.5 inch was added to allow top loading of the microscope. Also, view ports were added to permit some coarse alignment of the microscope while inside the chamber. The evaporation system consists of an e-beam gun with a four-pocket hearth (where the metal sources sit), allowing four evaporation sources to

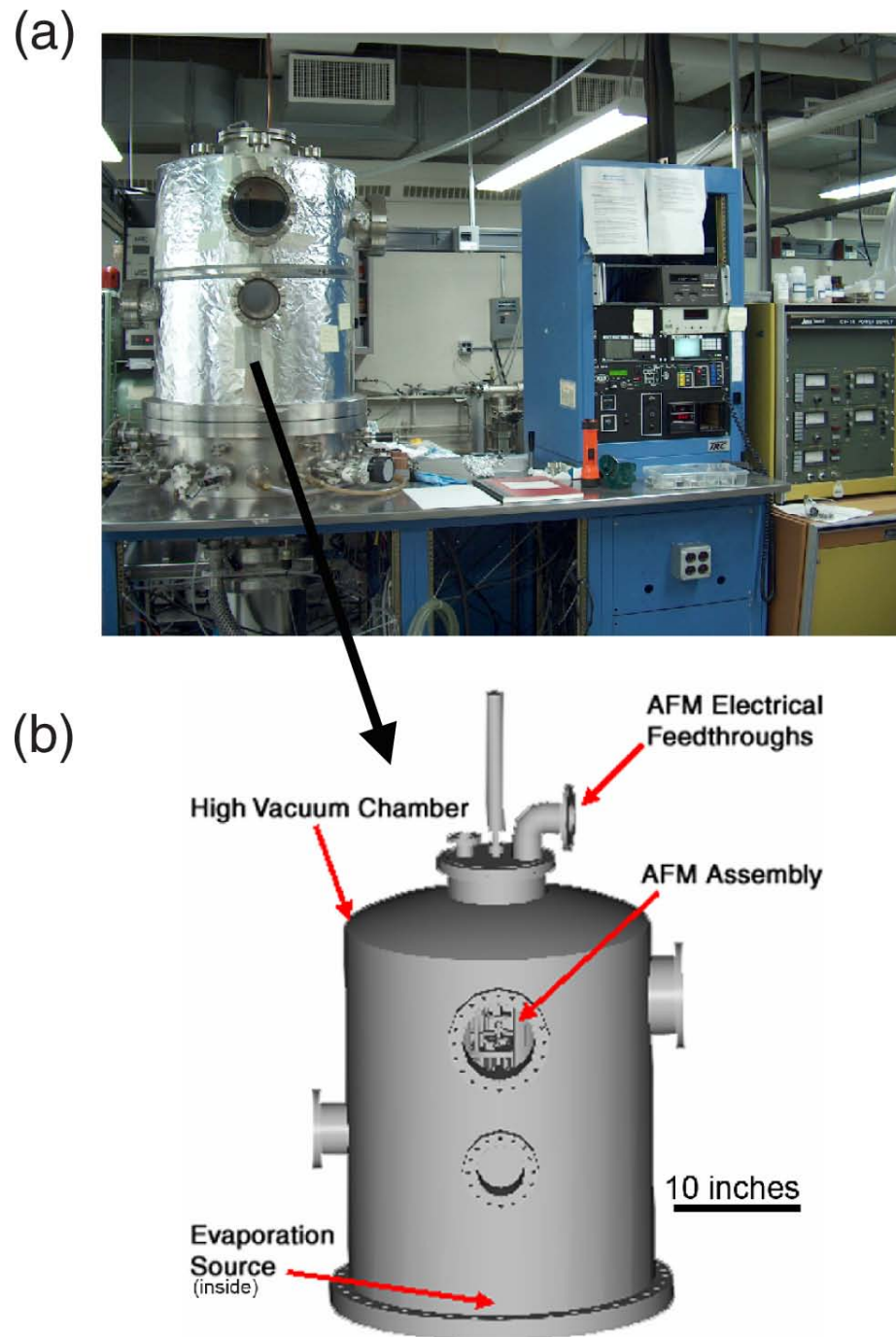


Figure 7.4: [The evaporation chamber] (a) The evaporation system used for pattern transfer. (b) The high-vacuum evaporation chamber inside of which the AFM is used to transfer patterns from stencil masks to the apex of AFM tips.

be loaded at once. The hearth is precisely aligned with the center of the chamber. This allows a direct line of sight between the metal source, stencil mask and tip, no matter what the rotational position of the microscope is. A thermal evaporation source is also available and is mainly used for evaporating a sticking layer (Cr) when necessary.

7.2.2 The microscope

A sketch of the microscope we built to transfer metallic patterns on AFM tips is shown in Fig. 7.5 (a), and a photograph of the entire microscope is shown in Fig. 7.5 (b). The microscope consists of three main parts: a vibration isolation system, a coarse XYZ positioning system and a scanning tube used for imaging.

Vibration isolation

To achieve high resolution imaging and to avoid damaging the tip during imaging it is very important to suppress vibrations that can couple to the AFM. The vibration isolation is ensured by two features of the microscope: a rigid AFM assembly and a damped spring suspension.

The AFM assembly (parts holding the scanning tube and AFM tip) is made compact and very rigid. This ensures that low-frequency vibrations (below ≈ 1 kHz) do not couple effectively into the AFM assembly. Indeed, for a rigid assembly, low frequency vibrations cause the sample and tip to move in sync, causing no disturbance to the imaging. The assembly is made of super-Invar alloy, which is rigid and has extremely low thermal expansion ($0.6 \times 10^{-6} / ^\circ C$). This low thermal expansion prevents any drift of the tip with respect to the stencil mask during the evaporation.

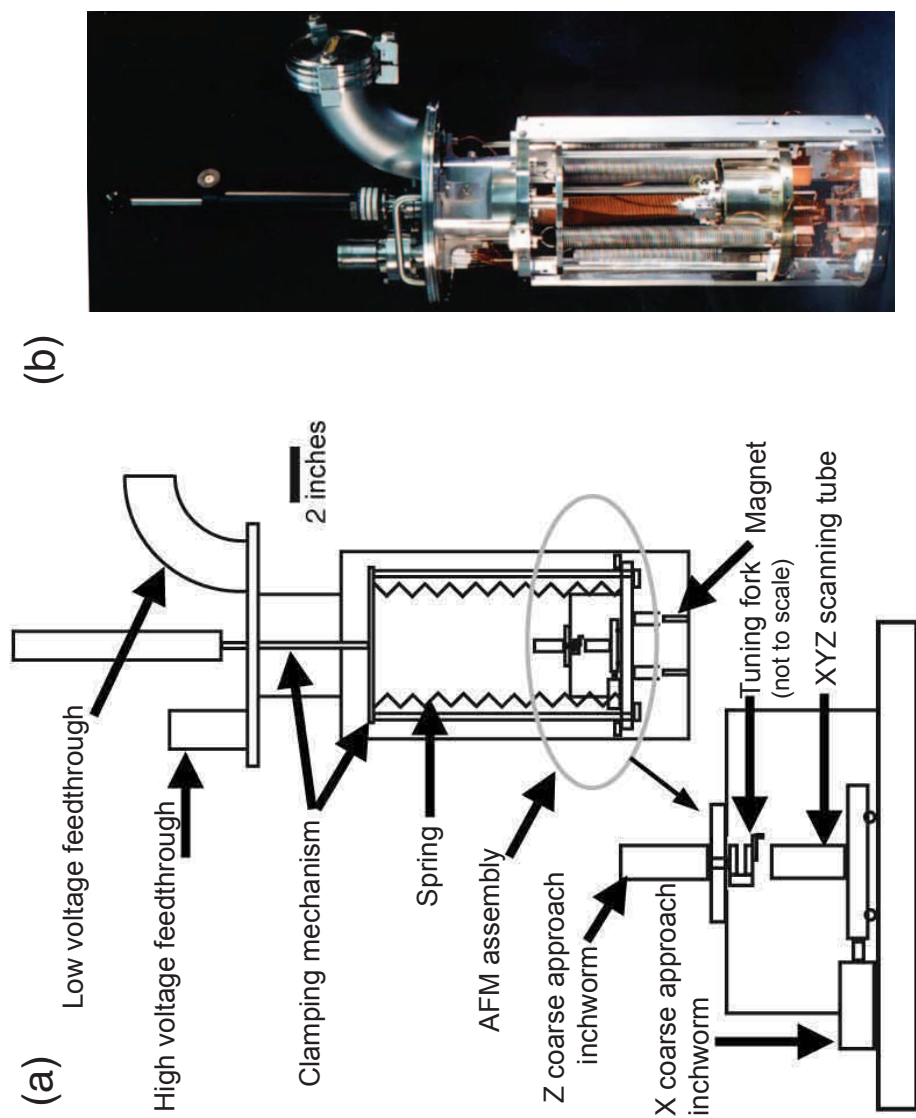


Figure 7.5: [AFM used to do stencil lithography on tips] (a) Sketch of the main components of the AFM (b) Photograph of the AFM.

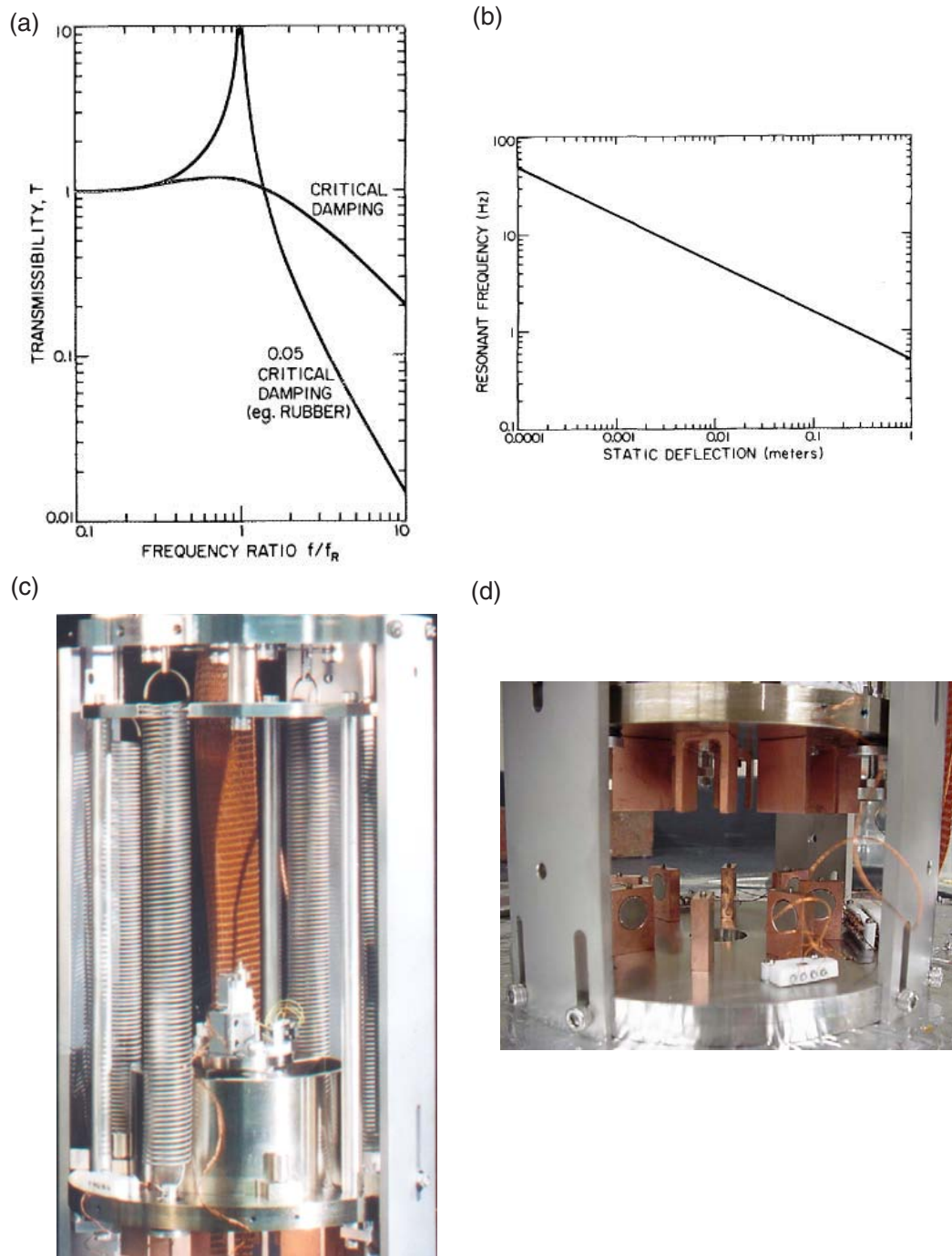


Figure 7.6: [Vibration isolation] Panels (a),(b) are taken from [8]. (a) Transmissibility of vibrations across an isolation oscillator as a function of frequency. (b) The resonance frequency of an oscillator as a function of its static displacement due to its load. (c) The clamping system and vibration isolation springs of the AFM. (d) The magnets and copper fins (overlapping when in use) that provide eddy current damping for the vibration isolation system.

To both eliminate further vibrations at low frequencies and reduce vibrations at frequencies above 1 kHz (where the scanning piezo tube has resonances), we use springs (See Fig. 7.6). Figure 7.6 (a),(b) taken from [8] show respectively the transmissibility across an oscillator as a function of frequency, and the resonance frequency of the oscillator as a function of its static deflection due to its load. Since we want to achieve a large suppression of building vibrations (≈ 20 Hz), it is important that the resonant frequency of our system is well below 20 Hz. The resonant frequency for a loaded oscillator shown in Fig.7.6 (b) is given by [8]:

$$f_R = 0.5Hz\sqrt{\frac{1}{\Delta(\text{in meters})}} \quad (7.1)$$

When our AFM assembly is floated on its four springs, the static displacement of the springs is 4 cm, which corresponds to a 2.5 Hz resonant frequency. As can be seen from Fig. 7.6 (a) the amplitude of the resonance and the slope of the subsequent roll-off are determined by the amount of damping in the system. The damping in our system is provided by eddy current damping. Figure 7.6 (d) shows samarium cobalt magnets and copper fins used for eddy current damping. The damping time of the assembly is ≈ 1 second, which means that the amount of damping in the system is about 0.4 times the critical damping. The damping coefficient and resonant frequency of the assembly permit a sufficient suppression of vibrations to achieve high resolution imaging. Yet, one must still be careful about acoustic noise which can couple into the system. A simple sound proofing box can eliminate such disturbances. Another issue is the vibrations coming from the electrical wiring of the microscope. To minimize this, wires are kept short and small in cross-section.

The microscope is also equipped with a linear translation mechanism that allows us to clamp down the AFM assembly instead of floating it on its four springs. With

the AFM assembly clamped down, we can move the microscope around without disturbing the tip-sample alignment. Therefore, we can align the tip to the stencil mask outside the evaporator, then clamp down the assembly while we load the microscope inside the vacuum chamber. The clamping system can be seen in Fig. 7.6 (c) as an aluminium frame holding up the AFM assembly.

Coarse positioning

The AFM has three piezoelectric inchworms that provide a XYZ coarse alignment of the tip to the stencil mask. The inchworms (UHVM-050, Burleigh Inst. [9]) have a travel distance of 10 millimeters and a motion resolution of about 10 nanometers. Figure 7.7 (a) shows the XY positioning system and the scanning tube. The translation stage, on which the scanning tube is mounted, slides on top of a polished sapphire disk to ensure a smooth motion. Three retainer posts prevent any tilting of the translation stage during motion.

Figure 7.7 (b) shows the Z coarse approach inchworm (in white). In panel (c) we can see the tuning fork and tip (sitting at the end of the inchworm) above a stencil mask chip. The stencil mask sits on top of the scanning tube which is covered by an aluminium shield.

The XYZ coarse positioning is used to align the tip above the stencil mask (a silicon-nitride membrane about $100 \times 100 \mu\text{m}$ in size). During the alignment the stencil mask and tip are imaged using an optical microscope equipped with a CCD-camera. The microscope was built with optical components from Optem [10] and has a magnification factor up to 28, a very long working distance ($\approx 15 \text{ cm}$) and a long depth of focus. Using the coarse alignment and optical microscope, the tip is centered on the stencil and kept about $10 \mu\text{m}$ away in Z. At this point the

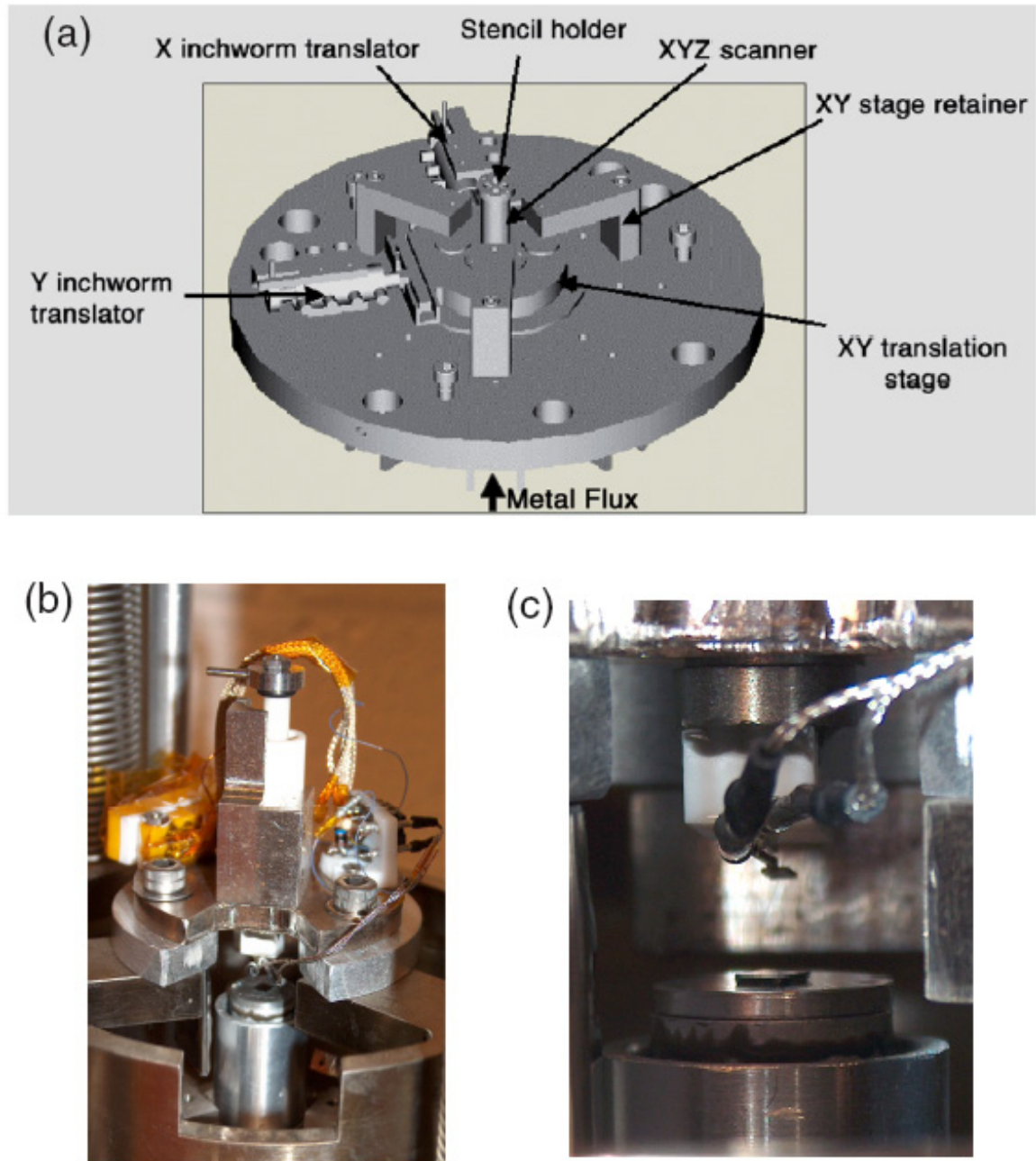


Figure 7.7: [AFM assembly] (a) The XY coarse alignment system and the XYZ scanning tube. (b) The Z coarse alignment inchworm motor (white) and pre-amp for the tuning fork signal (c) The tuning fork and tip above a stencil mask mounted on the XYZ scanning tube (inside an aluminium shield).

microscope is ready to start the final approach routine, and later the imaging of the stencil mask.

Scanning tube

The AFM imaging is done using a piezoelectric tube manufactured by Staveley Sensors [11] (see Fig. 7.8 (a)). The tube is made of EBL #3 and is coated with nickel electrodes. The inside of the tube is a single electrode, called Z, used to adjust the vertical extension of the tube. The outside of the tube is divided in four quadrant electrodes, called X+, X-, Y+, Y-, that are used to steer the tube in the XY plane. We filled the gaps between the X and Y electrodes with an insulating epoxy to avoid breakdown between the electrodes. We mounted the tube to a macor base with a UHV compatible epoxy, and made electrical connections to the electrodes using a silver epoxy. We also attached an aluminium sample mount to the top of the tube. The sample mount has two small screw holes that can be used to fasten a sample holder to the scanning tube. A sample holder (on which a sample is mounted) is shown in Fig. 7.8 (b).

The tube's inner electrode is covered by a thin sheet of mylar. This prevents the evaporated metal, which goes through the tube during the pattern transfer process, from shorting the Z electrode of the tube to other parts of the assembly.

The tube's dimensions are $1.00'' \times 0.388'' \times 0.025''$, and its scanning range is about $5 \mu\text{m}$ in Z and $20 \mu\text{m}$ in X and Y for applied voltages of $\pm 220 \text{ V}$ on the tube's electrodes. Every piezoelectric tube behaves differently; has different amounts of non-linearities in motion versus applied voltage and cross-talk between the X, Y, Z axes. These variations arise from the fabrication and mounting of the tube. In order to correct for such imperfections in the tube's behavior, the tube

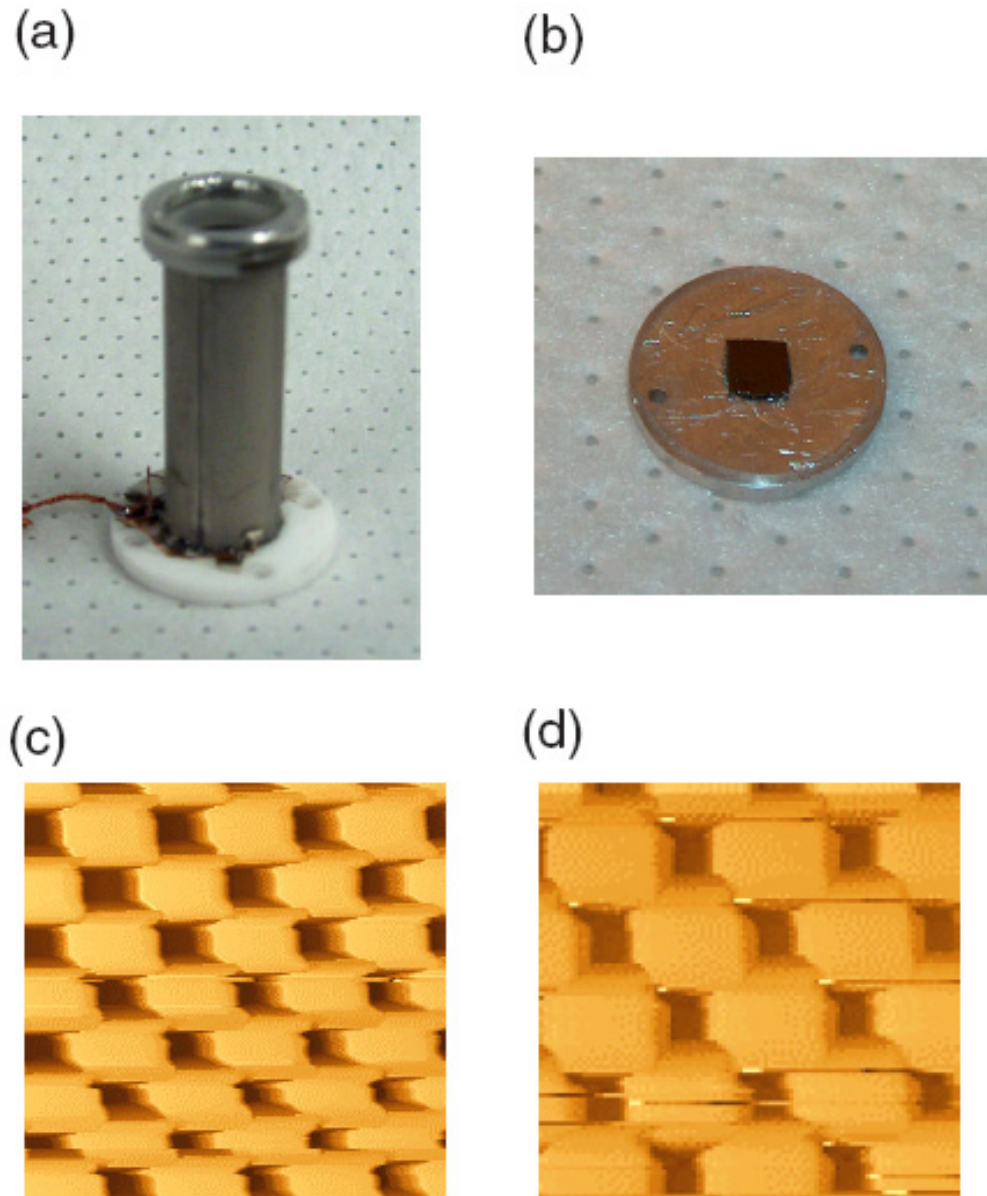


Figure 7.8: [AFM scanning tube and sample holder] (a) The piezoelectric scanning tube used for AFM imaging. (b) A sample holder that mounts on top of the scanning tube. (c) An AFM scan of a calibration grating before calibration and (d) after calibration.

must be properly calibrated using a sample consisting of a periodic array of known dimensions. Once this surface is imaged, the non-linearities and cross-talk effects can be corrected by the imaging software. The software also uses the dimensions of the calibration array to calibrate the XYZ displacements (i.e. how much deflection is produced by a given voltage applied to the tube's electrodes). Figure 7.8 (c) and (d) show the images of a calibration grating acquired with the scanning tube before calibration (c), and after calibration (d). The scan area is $7.5 \times 7.5 \mu m$ for the calibrated image.

7.2.3 Tuning fork feedback, electronics and software

We have discussed how the microscope ensures that the scanning assembly has good vibrational isolation and how it enables the AFM tip to be both coarsely aligned and finely raster scanned above a sample. We now turn to how the distance between the tip and sample can be controlled to provide a topographic map of the sample on a nanometer scale.

Tuning fork feedback

To control the distance between the AFM tip and the sample's surface we make use of a piezoelectric quartz tuning fork feedback [12, 13, 14]. The tuning forks we use have a sharp resonance at 32.768 kHz and are commercially available [15]. When purchased, the forks come individually packaged inside a vacuum can and with two leads attached to them. It is important to be very careful when removing the forks from their packaging since any small damage to the forks will disrupt their resonance.

The idea of tuning fork feedback is simple. If an AFM tip is solidly attached to

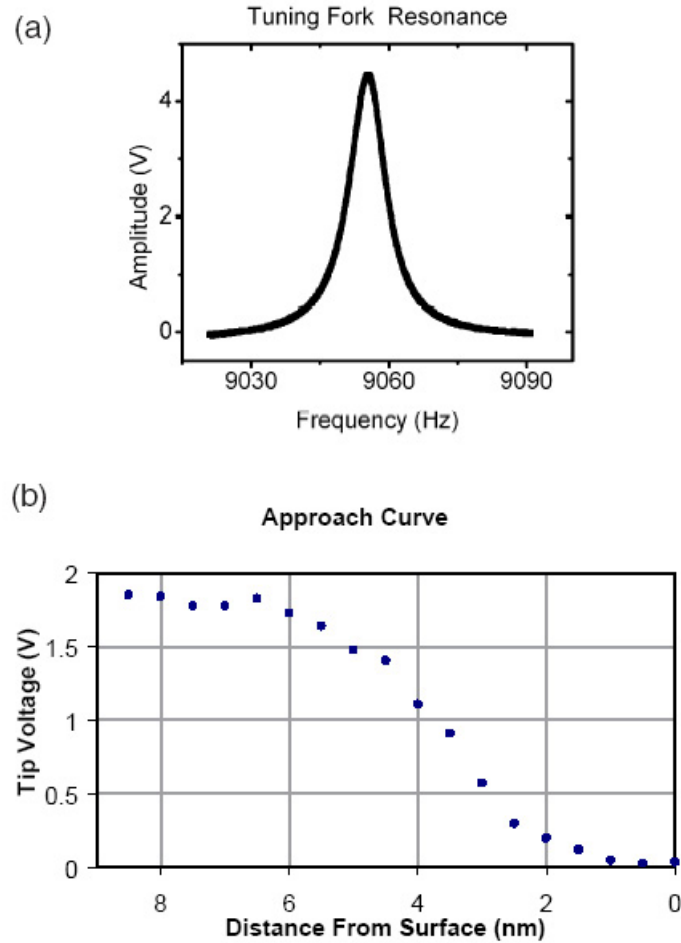


Figure 7.9: [Resonance of a tuning fork] (a) Amplitude of the output of the lock-in amplifier measuring the amplitude of current oscillations in a tuning fork versus the driving voltage frequency. (b) Approach curve showing the amplitude of the lock-in output versus the distance between the tip and surface. The tuning fork is driven at its resonance frequency when far from the surface. As the tip approaches the surface, the resonance frequency of the fork changes and its vibration amplitude drops.

the fork, the fork's resonance will remain sharp (see Fig. 7.9 (a)). This resonance can be observed by exciting the tuning with a sinusoidal voltage of a few mV, while measuring its output current (order of a few nA) using a lock-in amplifier. When the AFM tip mounted on the tuning fork approaches within a few 10's of nm of a surface, the tip's van der Waals interaction with the surface modifies the spring constant of the tuning fork and therefore its resonant frequency. The shift in resonant frequency for our fork-tip assemblies is a few 10's of Hz. Thus, we can use either the frequency or amplitude of the tuning fork oscillations to monitor the distance between the tip and surface. A typical approach curve of an AFM tip to a surface is shown in 7.9 (b), where the fork is excited at a constant frequency and drive amplitude (no feedback). As the oscillator's resonant frequency gets shifted due to tip-surface interactions, the amplitude of the oscillation is reduced since the fork drive is now off resonance. The AFM electronics control the scanning tube Z-electrode voltage so as to maintain a constant fork amplitude as the sample is scanned. The XY map of the Z-electrode voltage corresponds to the topography of the sample. When we use tips that are equipped with a cantilever, it is important to select cantilevers with a resonant frequency quite different from the final fork resonant frequency (around 10 kHz).

We mount tuning forks on small blocks of macor (ceramic) that are themselves mounted on permanent magnets. The magnet holds the fork assembly on the Z coarse approach motor. The fork and magnet are mounted with a very rigid epoxy available in auto parts stores (JB weld). The macor pieces are machined with a 13 degree angle which emulates the angle of scanning heads used in commercial AFMs. This is done to ensure that the location of the tip's apex is the same whether we use a tip in our microscope or in a commercial machine. This ensures

the portability of the tips we fabricate.

We mount commercially available AFM tips [16] onto magnet-macor-fork assemblies using a jig shown in Fig. 7.10 (a),(b). The jig has three axes of motion that permit proper alignment between the tip and fork. During the mounting and curing period of the epoxy (5 minute epoxy, that can be easily broken off later on) the tip is held in place by a small vacuum hole on the mounting jig (pumped on with a mechanical pump). The resulting holder-fork-tip assembly is shown in 7.10 (c). When the assembly is completed, the quality factor of the tuning fork can be up to 500 in air and 2000 in high-vacuum (see Fig. 7.9 (a)). This range of quality factor is optimal for imaging, providing high-sensitivity and a reasonable response time.

Electronics and software

A simplified diagram of the AFM electronics is shown in 7.11. The electronics serve four main functions. They control the XYZ coarse approaches, they drive the tuning fork and measure its amplitude, they feedback on the tuning fork amplitude to control the Z-extension of the piezo tube, and they raster scan the sample surface to create an image. The two former functions are controlled by a custom-made software (see Fig. 7.12), while the two latter are controlled by a commercial software from TopoMetrix.

In order to optimize the tuning fork electronics it is important to understand the equivalent electrical circuit (LRC circuit) of the tuning forks we use [17]. Like any piezoelectric element, when a tuning fork changes shape (vibrates) it develops a voltage across its electrodes. Associated with this voltage is a current which depends on the tuning fork impedance, and is strongly frequency dependent. We

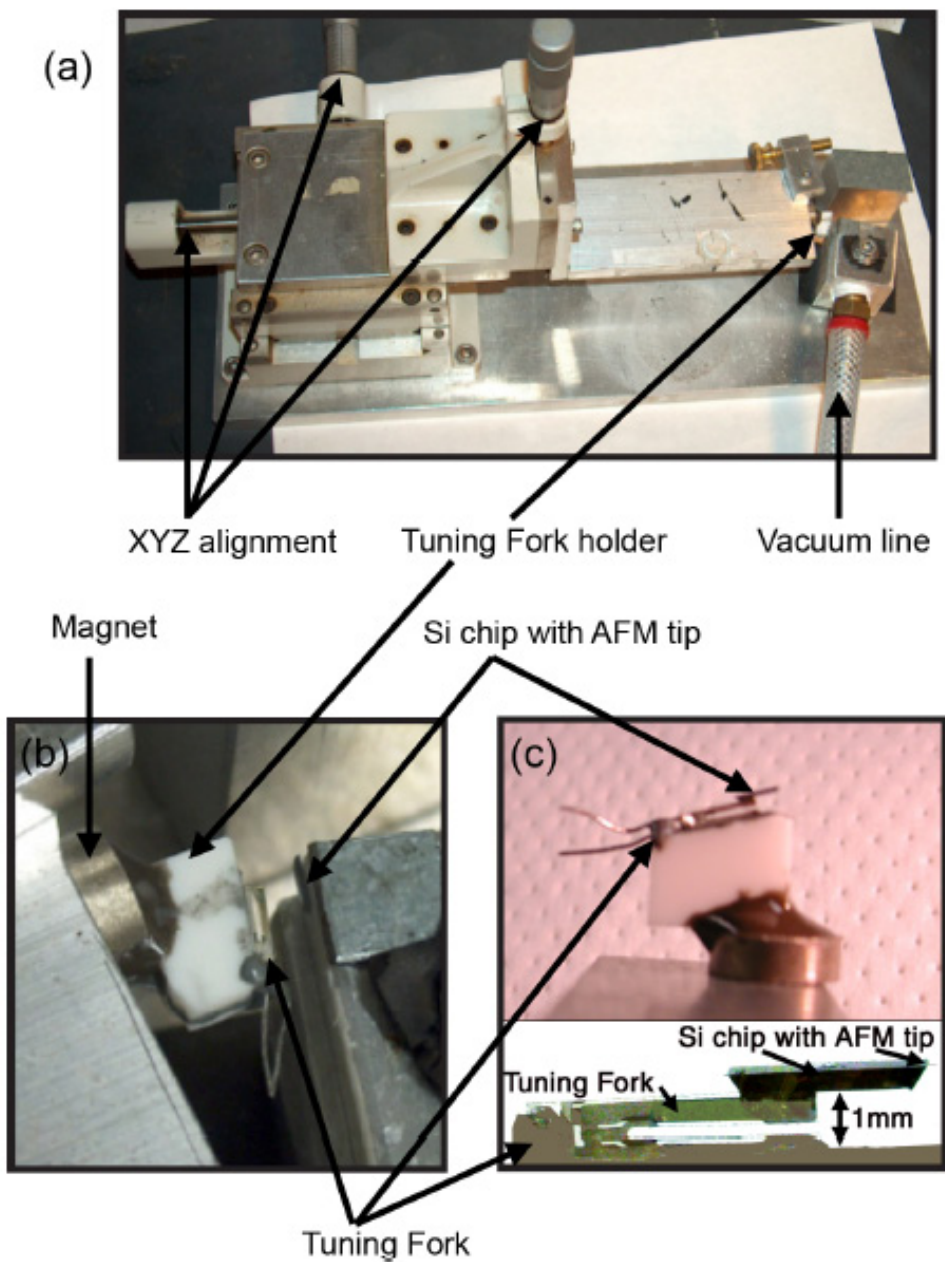


Figure 7.10: [Mounting an AFM tip on a tuning fork] (a) The jig used to mount commercially available AFM tips on quartz tuning forks. (b) Zoom of the tuning fork holder, tuning fork, and AFM tip. (c) A mounted AFM tip.

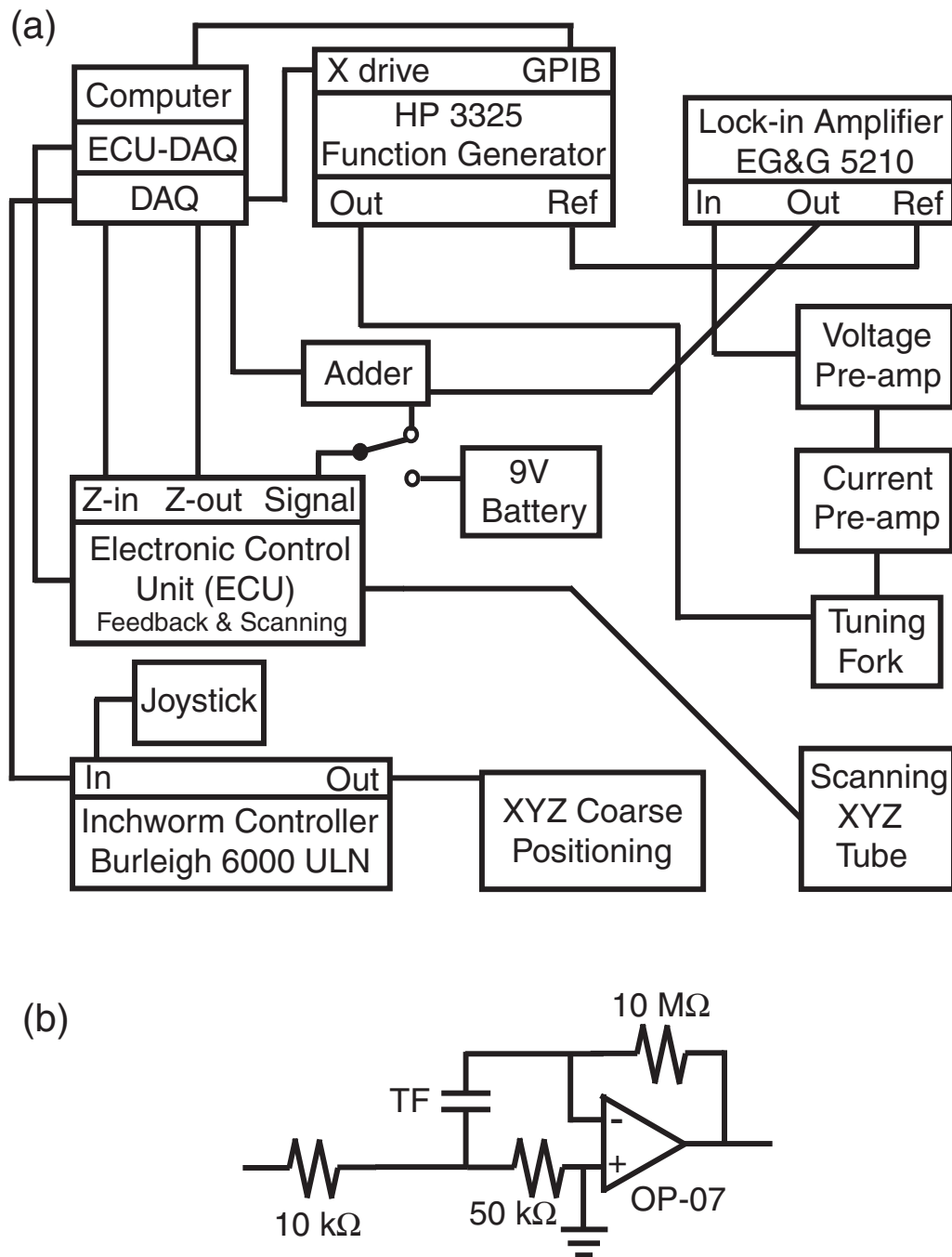


Figure 7.11: [AFM Electronics Overview] (a) Simplified diagram of the AFM electronics. (b) The tuning fork pre-amp which is located directly on the AFM assembly.

drive the tuning fork with a sinusoidal waveform between 1 and 10 mV in amplitude using a HP 3325 function generator. The current generated by the motion of the tuning fork is converted to a voltage by a small pre-amplifier, see Fig. 7.11 (b). The measured voltage is then further amplified and sent to a lock-in amplifier (EG&G 5210) with a time constant of 1 msec. The output of the lock-in is then sent to the input signal of the TopoMetrix ECU (Electronic Control Unit). Before approaching the surface for imaging, we scan the drive frequency of the tuning fork to find its resonant frequency (see Fig. 7.9 (a) and 7.12 (b)). The drive frequency is then set on resonance with enough amplitude to give a lock-in output of a few volts. The driving frequency of the tuning fork is kept constant and we monitor the amplitude of oscillation rather than the frequency. In theory, the shift in resonant frequency of the fork is more sensitive and has a faster response than the amplitude change [18]. In practice, an amplitude feedback works just as well [14]. The first reason for this is that in our case the frequency shift is large, providing a large amplitude-change signal. Second, we are not interested in a response time faster than 1 kHz both because the scanning tube's response becomes sluggish above such a frequency and because of the lock-in time constant.

The coarse positioning in XYZ uses a Burleigh 6000 ULN inchworm controller. The controller is either operated with a hand-held control pad or via the computer DAQ card. The fine Z approach is done jointly via the computer DAQ card and the ECU. We modified the ECU so that we can add an arbitrary voltage to the ECU's piezo tube Z-electrode output voltage. The Z final approach is then controlled by a custom-made LabWindows software, see 7.12 (c). The software proceeds as follows: it retracts the scanning tube fully ($V_z = -220$ V), takes steps (about $3 \mu\text{m}$ distance) in the Z-coarse approach inchworm, then ramps up the piezo tube until

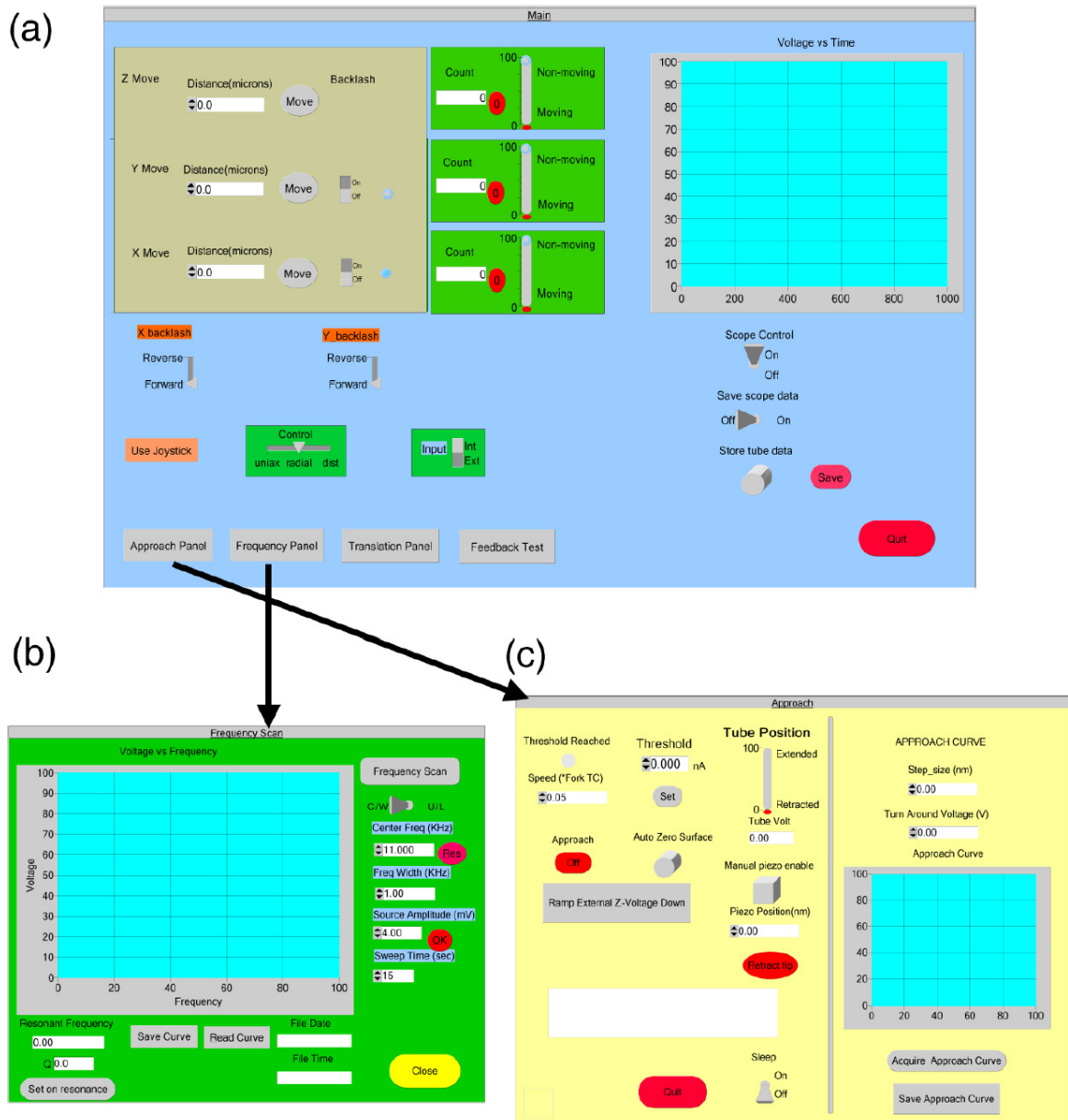


Figure 7.12: [Approach and tuning fork control software] Custom designed software that operates the XYZ approaches, and drives the tuning fork. (a) Main panel, used for XYZ coarse positioning. (b) Frequency panel, used to find the tuning fork resonance. (c) Approach panel, used for the final Z approach.

it finds the surface (when the tuning fork amplitude changes). If the surface is not found, the cycle is repeated. Once the surface is found, the software uses the coarse approach motor to center the surface around $V_z = 0$ V to ensure a maximum Z imaging range.

After the approach procedure, the control of the scanning tube is insured by the TopoMetrix ECU unit and software (except during pattern transfer). The ECU uses the tuning fork amplitude measured by the lock-in and a PID feedback to maintain the tip-sample distance during the imaging. The feedback parameters can be optimized by adding externally a small square wave onto the V_z of the piezo. The parameters are then adjusted until the ECU voltage faithfully follows the disturbance. Once this is done, the imaging is controlled via the ECU software similarly to any commercial AFM. In Fig. 7.13 we show several images acquired with the microscope. Typically the noise level in Z height can be reduced to about 1 nm when imaging on a suspended membrane. The XY resolution is strongly dependent on the tip used but is usually of the order of 10 nm. When imaging suspended membranes it is crucial to use small feedback parameters and a small tuning fork driving voltage to avoid “bouncing” the tip on the membrane.

In this chapter, we have described our custom made AFM microscope and its technology. In the next chapter we will discuss how it can be used to do nm-size lithography on AFM tips and build functional SPM probes.

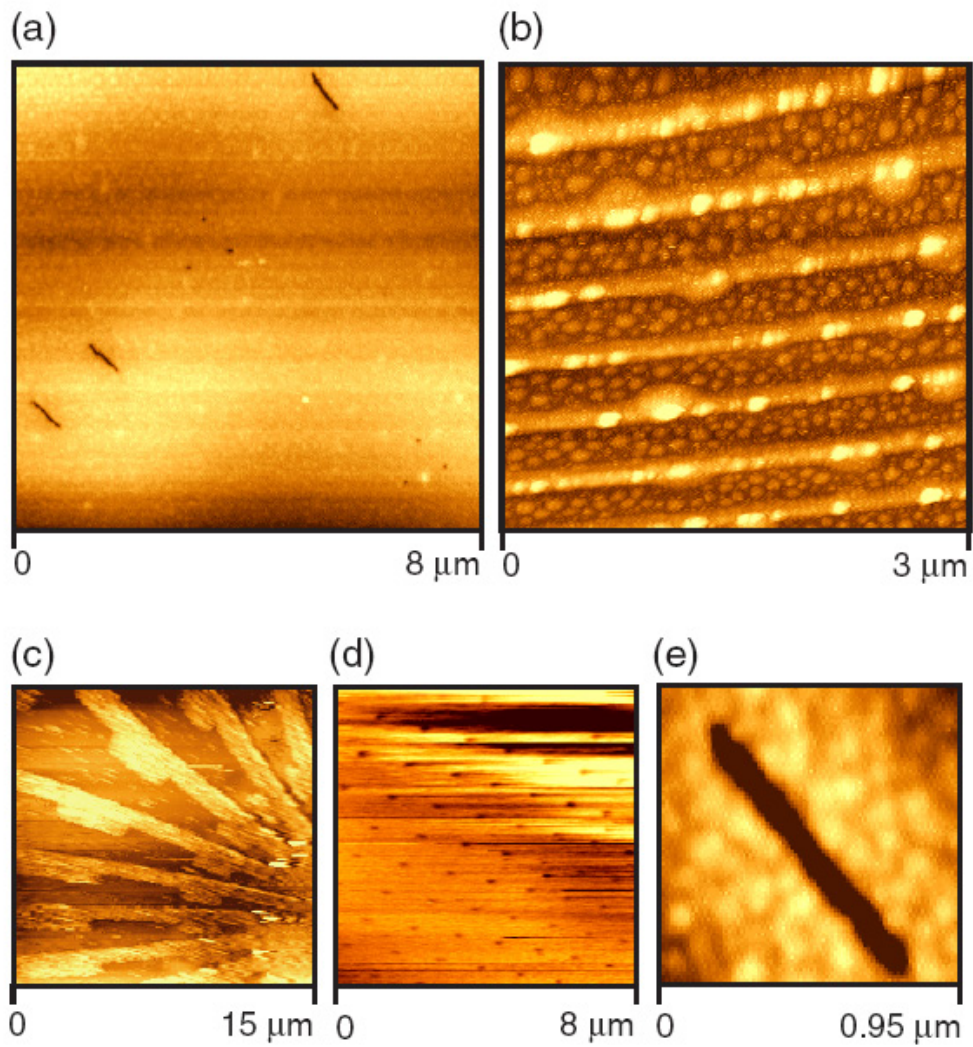


Figure 7.13: [AFM scans] A few AFM images acquired with our microscope. All images are taken on suspended 50 nm-thick silicon nitride (Si_3N_4) membranes. (a) An image of etched lines and dots. The color scale is 25 nm. (b) An image of gold lines and particles. The color scale is 45 nm. (c) An image of an e-beam defined Au pattern. The color scale is 150 nm. (d) An image of an array of holes. The color scale is 72 nm. (e) An image of a single etched line. The color scale is 10 nm.

BIBLIOGRAPHY

- [1] M. M. Deshmukh, D. C. Ralph, M. Thomas, and J. Silcox, *Applied Physics Letters* **75**, 1631 (1999).
- [2] A. R. Champagne, A. J. Couture, F. Kuemmeth, and D. C. Ralph, *Applied Physics Letters* **82**, 1111 (2003).
- [3] A. R. Champagne, A. J. Couture, F. Kuemmeth, and D. C. Ralph, (In preparation for RSI).
- [4] H. Zhou et al., *Journal of Vacuum Science & Technology A - Vacuum Surfaces and Films* **17**, 2233 (1999).
- [5] G. D. Skidmore and E. Dan Dahlberg, *Applied Physics Letters* **71**, 3293 (1997).
- [6] U. Hartmann, *Annual Review of Materials Science* **29**, 53 (1999).
- [7] L. Gurevich, L. Canali, and L. P. Kouwenhoven, *Applied Physics Letters* **76**, 384 (2000).
- [8] P. K. Hansma and J. Tersoff, *Journal of Applied Physics* **61**, R1 (1987).
- [9] Exfo, <http://www.exfo.com/en/burleigh.asp>.
- [10] Thales-Optem, <http://www.thales-optem.com>.
- [11] Staveley, <http://www.staveleyndt.com>.
- [12] K. Karrai and R. D. Grober, *Applied Physics Letters* **66**, 1842 (1995).
- [13] H. Edwards, L. Taylor, W. Duncan, and A. J. Melmed, *Journal of Applied Physics* **82**, 980 (1997).
- [14] R. D. Grober et al., *Review of Scientific Instruments* **71**, 2776 (2000).
- [15] Newark, <http://www.newark.com>.
- [16] Mikromasch, <http://www.spmtips.com>.
- [17] Y. Tomikawa, H. Miura, and S. B. Dong, *IEEE Transactions on Sonics and Ultrasonics* **25**, 206 (1978).
- [18] T. R. Albrecht, P. Grutter, D. Horne, and D. Rugar, *Journal of Applied Physics* **69**, 668 (1991).

Chapter 8

Nanometer-scale scanning probes built using stencil lithography

In this chapter we describe how the apparatus introduced in chapter 7 can be used to accomplish high-resolution (10 nm) lithography at the end of AFM tips to make SPM probes [1, 2].

First, in section 8.1 we present the fabrication procedure to make the stencil masks needed for pattern transfer. We also discuss the requirements for these stencils.

Second, we discuss in section 8.2 the procedure to transfer the features between the stencil masks and the AFM tips. Figure 8.1 shows the AFM tips used and the pattern transfer geometry. The lithographic capabilities of this technique are described in section 8.3.1. The fabrication and characterization of MFM sensors is discussed in 8.3.2, and the progress toward making g-STM sensors in 8.3.3.

We conclude this chapter by addressing the potential of this technique to build other types of probes, and what technical challenges must be met to do so.

8.1 Stencil Mask Fabrication

The stencil masks we use to do lithography determine the ultimate resolution we can achieve. To make high quality probes we must fabricate stencils on which:

1. e-beam lithography and etching can be used to make small features (≈ 10 nm)

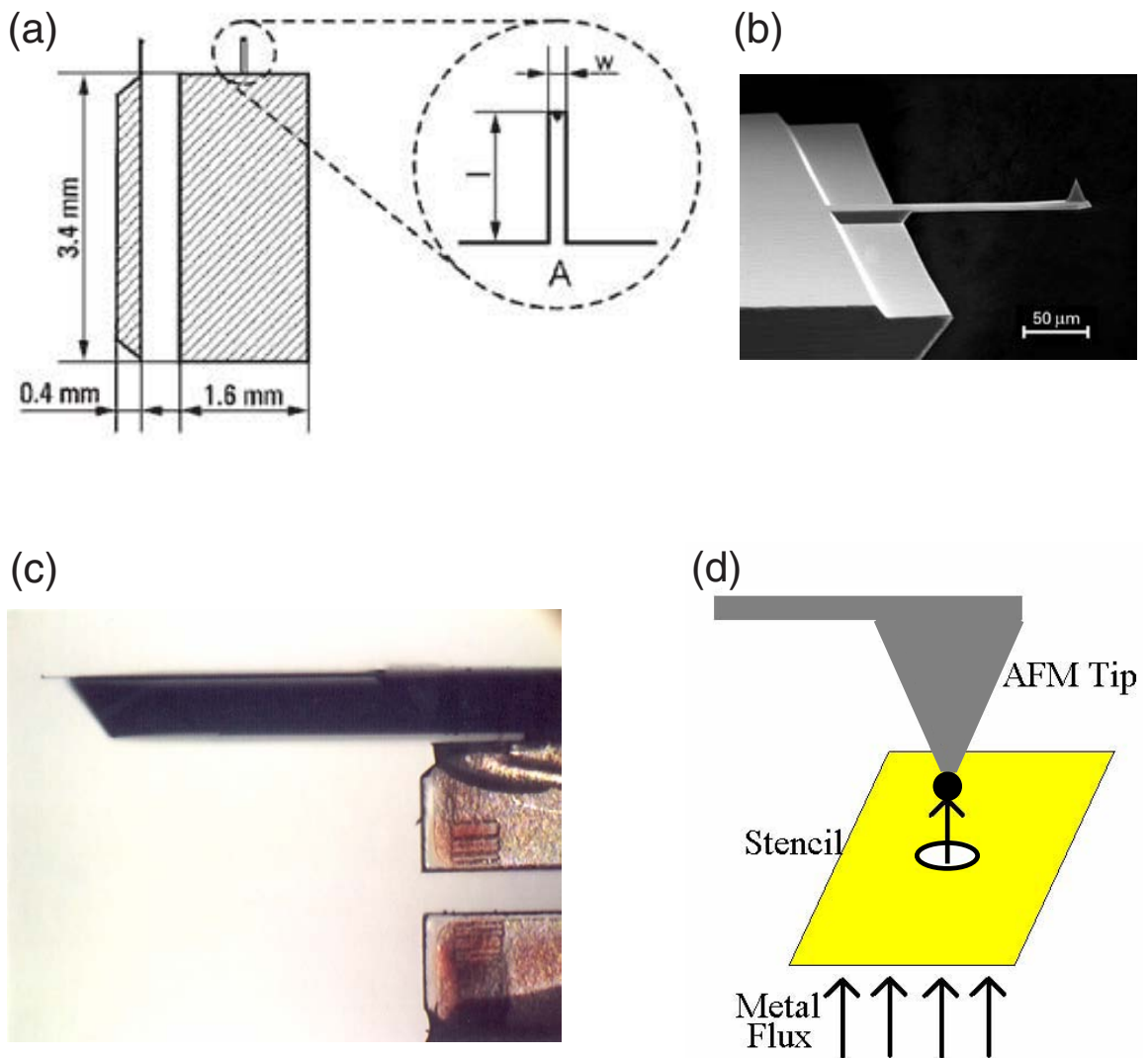


Figure 8.1: [Commercial AFM tip] (a)-(b) taken from [3] (a) Cartoon of a commercially available silicon chip on which are microfabricated a cantilever and an AFM tip, $l = 125 \mu\text{m}$ $w = 35 \mu\text{m}$. (b) An SEM image of the cantilever beam and tip. (c) An optical image of an AFM Si-chip mounted on a quartz tuning fork used for feedback. (d) The stencil mask pattern transfer technique.

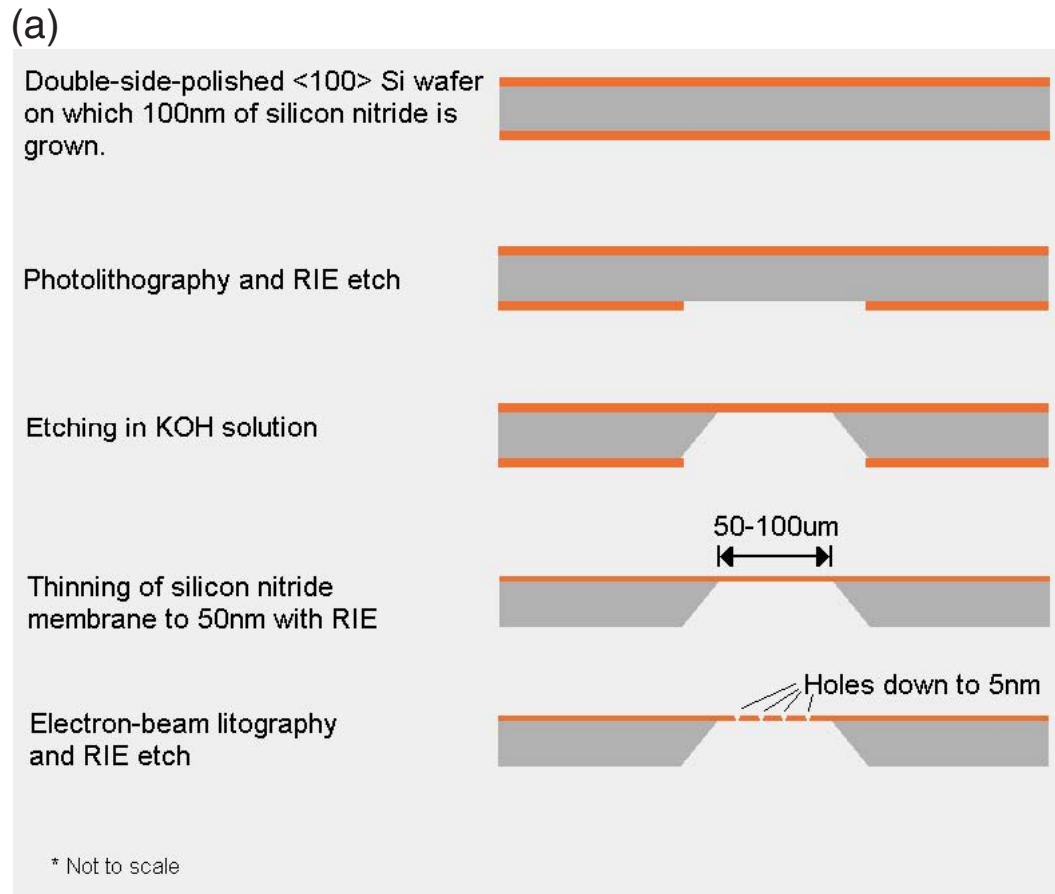
2. the feature size is uniform everywhere on the stencils' surface
3. the features can rapidly and reliably be located with the AFM
4. there is no surface contamination

This section describes the design, fabrication and characterization of stencil masks that meet these requirements.

8.1.1 Fabrication steps

We set out to fabricate a large number of chips containing a thin suspended silicon nitride membrane on which features down to 10 nm in size can be etched. The fabrication process was first developed by Kristin Ralls *et al.* [4] and later adapted by Dan Ralph *et al.* [5] to make metallic point contacts. An almost identical fabrication process to the one we use was described in great detail by my predecessors [6, 7, 8]. Therefore, we will only outline the fabrication steps and mention in **bold any modification made to the original fabrication method**. The fabrication process makes use of the equipment available at the Cornell Nanofabrication Facility (CNF) and in our labs in Clark Hall. Figure 8.2 provides a short pictorial summary of the fabrication steps.

1. We start our fabrication process with double-side polished $\langle 100 \rangle$ 3-inch wafers (usually a batch of 25). The first step consists in MOS cleaning the wafers and growing a low-stress **125 nm-thick film of silicon nitride** on the wafers using low pressure chemical vapor deposition (LPCVD) at 850 °C.
2. Next we do photolithography using the HTG contact aligner on the back side of the wafers (usually I process in batches of 8 wafers) to define the breaklines



(b)

Photolithography can be added on the membrane to help locate the ebeam features during the AFM imaging

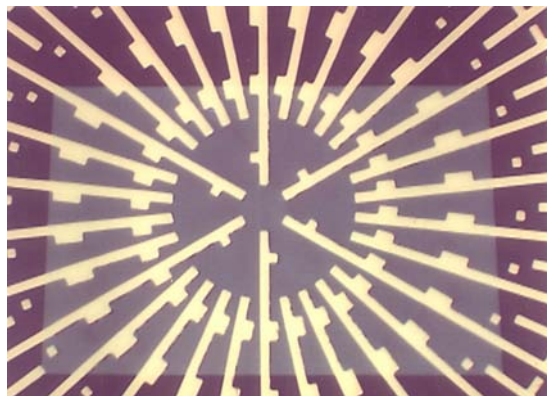


Figure 8.2: [Stencil fabrication steps] (a) An outline of the main steps involved in making suspended Si_3N_4 membranes. (b) An optical image showing a top view of a membrane on top of which an extra step of lithography was done.

and the stencil windows. The mask used is shown in Fig. 8.3. The mask exposes an array of **11 × 11 windows** plus four extra windows to be used for alignment purposes during the e-beam lithography. This step is crucial since the size of the exposed squares on the back of the wafer will determine the final size of the stencil windows. The wafer will be etched along its $\langle 111 \rangle$ plane (35.26° to the normal) later in the fabrication process. This means that the wafer thickness will influence the final size of the stencil masks. Thus, a new photolithography mask must be designed for each batch of wafers (if their thickness is different). The photolithography mask window size to be used is given by the following equation:

$$\text{mask size} = 100 \mu\text{m} + 2 \times (\text{thickness of wafer}) \times \tan(35.26^\circ) - 40 \mu\text{m} \quad (8.1)$$

where the **100 μm** is the desired size of the stencil windows, and the **40 μm** is the estimated amount of undercut during the Si etch process. Similarly the width of the mask's breaklines must be calculated so that their depth after the KOH is limited to about 1/3 of the wafer's thickness.

3. After the photoresist has been developed, the exposed silicon nitride on the back of the wafer is etched in an RIE with CHF_3 and O_2 gases. See Fig. 8.2 (a).
4. Then, the Si wafers are etched with a warm ($95 - 100^\circ\text{C}$) solution of KOH. A temperature at the lower end of this range will result in a slower etch rate, but most importantly a more uniform etch rate across the wafers. The KOH etch rate for Si is much greater than for Si_3N_4 , which permits to etch the backside trenches all the way through the Si wafers. The etch is stopped by the silicon nitride film on the front of the wafers, leaving suspended membranes of silicon

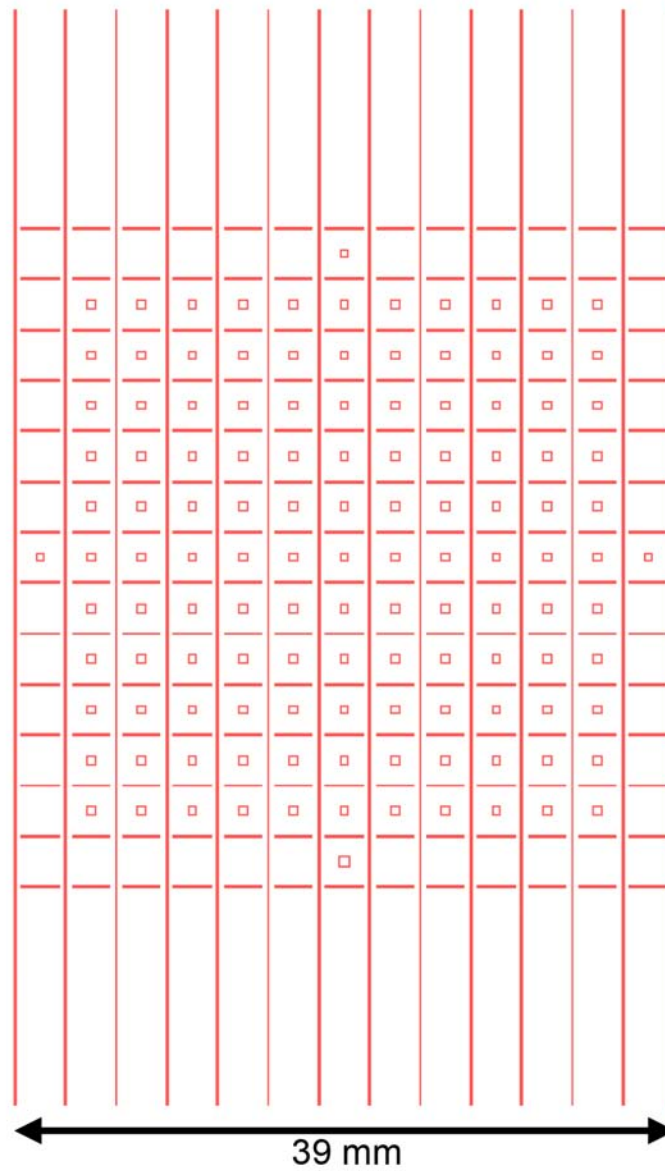


Figure 8.3: [Photolithography mask used for fabricating stencils] The CAD design of the contact lithography mask used to expose the back side of 3-inch wafers to make stencil masks. Each die is 3×3 mm. The thick lines are breaklines, and the small squares define the suspended membranes.

nitride. This etch generally takes about three hours and must be followed by a thorough rinsing to remove any leftover KOH.

5. We measure the front side silicon nitride thickness by interferometry for each wafer. After this, each wafer's front silicon nitride is thinned down to a precise thickness using a RIE ($\text{CHF}_3 / \text{O}_2$) etch. It is important to etch the membranes of each wafer to a standard thickness since this will determine the reproducibility of the e-beam lithography. Depending on what features will be exposed on our membranes we thin them down to either **50 or 100 nm**. Figure 8.4 (a) shows an optical picture of a full wafer with etched windows, and panel (b) and (c) show respectively a top and bottom view of a single stencil.

6. We are now ready to define the features to be etched in the stencils using e-beam lithography. All of the stencils we use are exposed using the Leica VB6 at CNF. The main difference between our exposures and the ones done by our predecessors [6, 7, 8] is that **we expose patterns of various shapes and sizes which are repeated everywhere on the stencil, rather than a single hole in the center of the stencil**. The purpose of exposing all of the membrane is to facilitate the location of the features when scanning with the AFM. For some wafers we restricted the area over which the stencil was e-beam exposed by adding an extra layer of photolithography (coordinate system) on the stencil prior to the e-beam exposure (see Fig. 8.2 (b)). Although this approach can be useful in specific circumstances (it increases the rigidity of the membrane), it is best to be avoided since it gives rise to a series of fabrication and AFM imaging complications. **In section 8.1.2**

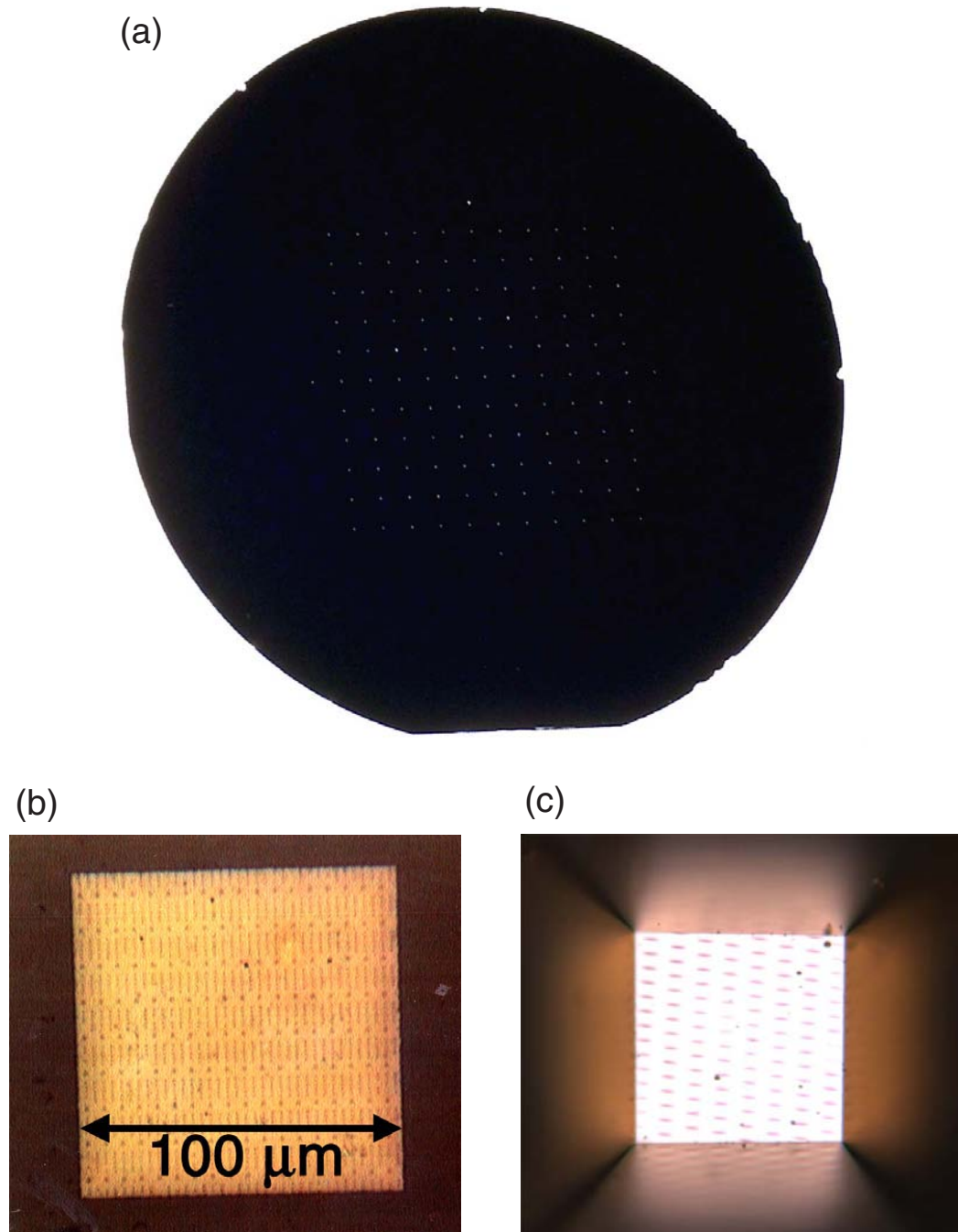


Figure 8.4: [Stencil masks] (a) A full 3-inch wafer on which an 11×11 array of stencil was fabricated. (b) Top view of a single stencil on which a pattern was written using e-beam lithography. (c) Looking from the back side of the wafer through a stencil mask.

we will discuss what rules should be followed when designing a pattern to be exposed on a membrane. Examples of job files (.COM) and patterns files (.FRE) used for such exposures are available on the VB6 machine in the directory: VB.USERS.RALPH.ALEX.BLIMPIE.

7. Once the features have been exposed, they can be etched using the Applied Materials RIE at CNF. We make use of a bottom fed gas flow (non-linear mode) and CHF_3 / O_2 gases. The timing of the etch is crucial to achieve small features (below 30 nm). Figure 8.5 shows a number of different patterns etched in stencils.
8. The wafers must now be diced into single $3 \text{ mm} \times 3 \text{ mm}$ chips. This is facilitated by the break lines that were etched in the wafer. Strips of chips can be diced by pressing the front side of the wafer over a sharp edge that is aligned with the breakline (or with your fingers). Individual chips can then be diced using a sharp edge or with a special jig.

This completes the fabrication of our stencil masks. Since we usually fabricate the masks in large batches, care must be taken to store the stencil under vacuum to avoid contamination over time.

8.1.2 Stencil design and characterization

There are restrictions as to what kind of patterns can be transferred onto a thin suspended membrane of silicon nitride. Another set of restrictions is necessary so that the features etched in a membrane can be imaged rapidly and without damaging the AFM tip. We also need a reliable way to characterize our stencil masks prior to pattern transfer. These issues are briefly discussed here.

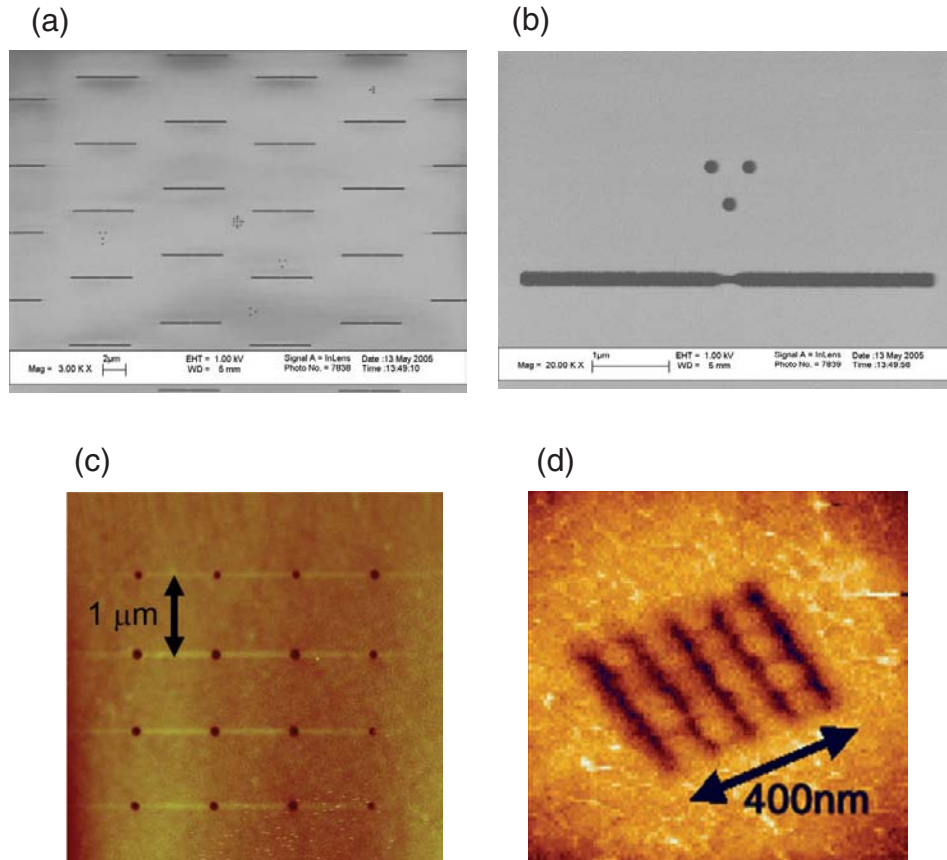


Figure 8.5: [E-beam lithography on stencils] (a) An SEM image of a membrane on which an array of lines was etched. The lines have a constriction in their middle and are used to make gated-STM tips. (b) Zoom of (a). (c) An AFM image of an array of holes etched in a stencil. (d) An AFM image of lines written on a stencil.

The most stringent limitation on what patterns can be etched in a thin (50-100 nm) membrane concerns lines. If multiples lines are etched on a stencil, they must not be lined up. Even with a spacing between lines several times larger than the lines' length, there is a probability that the stresses in the membrane will create cracks along the lines direction. This can easily be avoided by offsetting the lines with respect to each other by as little as a few hundreds of nm. A single line's length should not exceed 10 μm for a 50-nm-thick membrane and 15 μm for a 100-nm-thick membrane. Circular holes should be spaced apart by at least 100 nm to avoid the nucleation of defects on the membrane. Making a membrane thicker (100 nm) helps a great deal in making it sturdier. Extra thickness helps to prevent cracking of a membrane on which closely spaced features have been exposed, and also helps make the membrane more resistant to AFM imaging and evaporated metal. The advantage of thinner membranes (50 nm) is that they can transfer smaller features, down to 10 nm in size, as compared to about 20 nm for 100 nm-thick membranes. Thin membranes have proven sufficiently robust for evaporating small arrays of features, but for transferring large contact leads it is safer to use thick membranes. Another variable that determines the strength of a membrane is its size. We have made and used successfully membranes up to 200 μm on their side. Such membranes are difficult to image if they are 50 nm-thick because they tend to "ripple" due to the stress in the nitride film. When imaging such large membranes it is crucial to optimize the feedback parameters of the AFM to avoid "bouncing" the tip on the stencil. The advantage of larger membranes is the ease with which the AFM tip can be aligned with the stencil. We have found that membranes $\geq 100 \mu\text{m}$ on their side can be aligned with ease.

When an AFM is used to image a stencil with holes in it, the AFM tip tends

to “fall” into the holes. What prevents the tip from going all the way through the membrane is the tip’s width. If the holes etched in the membrane are wide, the tip cannot be scanned rapidly across the surface without hitting the edges of the holes. This risks not only of damaging the tip, but also ripping apart the membrane. Therefore, it is unreasonable to scan holes more than 200 nm wide with a sharp tip. To be able to scan a sharp tip rapidly and without worrying, the holes have to be kept to about 100 nm in size (diameter for circular holes, width for line-shaped holes). Much larger holes can be scanned with blunt tips.

We have found that the only reliable way to characterize the size of the features etched in a stencil mask is with a Transmission Electron Microscope (TEM). Previously, point contact metallization was used for characterizing the size of holes in stencils. We found that the resistance of such point contacts reflects the cross-section of the metallic bridge formed during evaporation and not necessarily the size of the hole in the stencil. In any case this method cannot be used for stencils with multiple holes. In Fig. 8.6 (a) we show a TEM image of a hole about 10 nm in diameter that is etched across a membrane. In panel (b) of the same figure we show a hole that has not been etched all the way across the membrane. In Fig. 8.6 (c) we show what a dirty stencil looks like. Such stencils cannot be used, because even though the holes in the stencil are well defined, an AFM tip would pick-up large amounts of dirt when scanning the stencil. Finally, in panel (d) we show an SEM image of a test Au pattern deposited on a flat silicon surface using stencil mask lithography. These test depositions are used to determine how well the stencils resist to the stress arising from a metal film being deposited on them, and how fast the stencil’s features clog up.

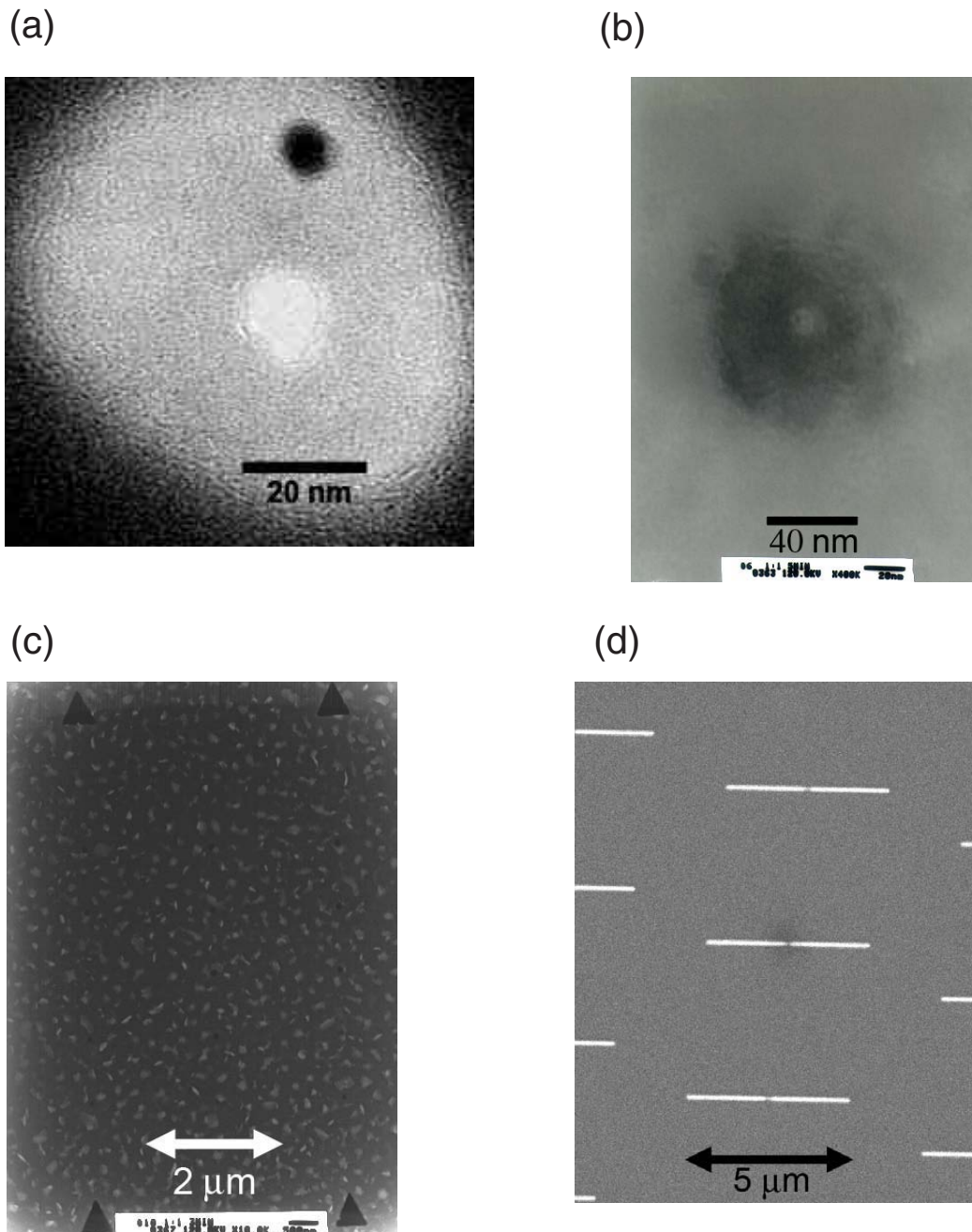


Figure 8.6: [Stencil mask inspection] Transmission electron microscope (TEM) images of (a) a single hole etched through a membrane, (b) a hole not etched all the way through, (c) a stencil with surface contamination. (d) An SEM image of a test pattern deposited on a flat Si surface using a stencil mask.

8.2 Pattern transfer procedure

We now describe how we use stencil masks and our custom AFM (see chapter 7) to transfer nm-size patterns onto commercially available AFM tips. The process consists of three groups of procedures: tip preparation, alignment and evaporation.

8.2.1 Tip preparation

Before launching into the process of doing lithography on an AFM tip, we must make sure the tip is of high quality. A large portion ($\geq 50\%$ in my experience) of commercially available tips are delivered with some form of defect. While such defects may not be harmful when the tip is used to do routine AFM imaging, they can cause deleterious effects to our lithographic process. The most common defects are: surface contamination, large surface roughness, poorly defined apex and poor or non-existent cantilever resonance.

We characterize our candidate tips with high resolution SEM imaging. This imaging allows us to select tips that are clean, smooth, and have a sharp apex (when desired). Figure 8.7 shows in panel (a) a large scale image of a clean tip and in panel (b) a zoom of the apex shows that the tip has a radius of curvature under 20 nm. For some applications it is desired to make blunt tips. For instance, only a small section of a sharp tip can be focused in an SEM, which makes it difficult to characterize the lithographic capabilities of our technique. Furthermore, we can imagine some SPM probes (for instance NSOM bow-tie antennas) which would require large devices (100s of nm) to be built at the end of tips. Such devices would have to be built on very blunt and smooth tips. We developed a process to controllably blunt tips. A large number of processes were attempted, but the

best results were obtained by combining a RIE (Applied Materials, 20 mTorr, 20 sccm SF₆ + 2 sccm O₂, 65 W) with a subsequent evaporation of SiO₂ on the tip. A longer etch time (to blunt the tip) and a larger amount of oxide evaporated (to smooth the tip) give a tip with a larger radius of curvature. For instance, the tip shown in Fig. 8.7 (c) was etched for 5 minutes and capped with 400 nm of SiO₂, giving an apex roughly 500 nm across.

The next step is to verify that the cantilever beam, on which the tip sits, has a sharp resonance. We can do this by loading the tip in a commercial AFM and using the standard procedure to scan the cantilever's response in the frequency domain. Although we do not make use of the cantilever's resonance in our AFM (we use a tuning fork), we need the cantilever to be functional since we intend to build SPM probes that can later be used in any commercial machine.

Finally, once a good tip is selected, it is mounted onto a tuning fork holder as was described in section 7.2.3. If the resonance of the AFM tip-tuning fork assembly is sharp, then we are ready for the next step.

8.2.2 Alignment procedure

The desired stencil mask, which has been characterized as described earlier (section 8.1.2), is loaded onto the piezoelectric scanning tube. We load the AFM tip-tuning fork holder in the microscope. We must now properly align the AFM tip, stencil mask, and the evaporation pinhole used to collimate the evaporated metal.

Figure 8.8 shows a cartoon (not to scale) of the pinhole alignment setup. We make use of a small light source placed at the bottom of the microscope to align the evaporation pinhole with the scanning tube and stencil mask. The pinhole is roughly 3 mm across to prevent any metal from depositing on the inside wall

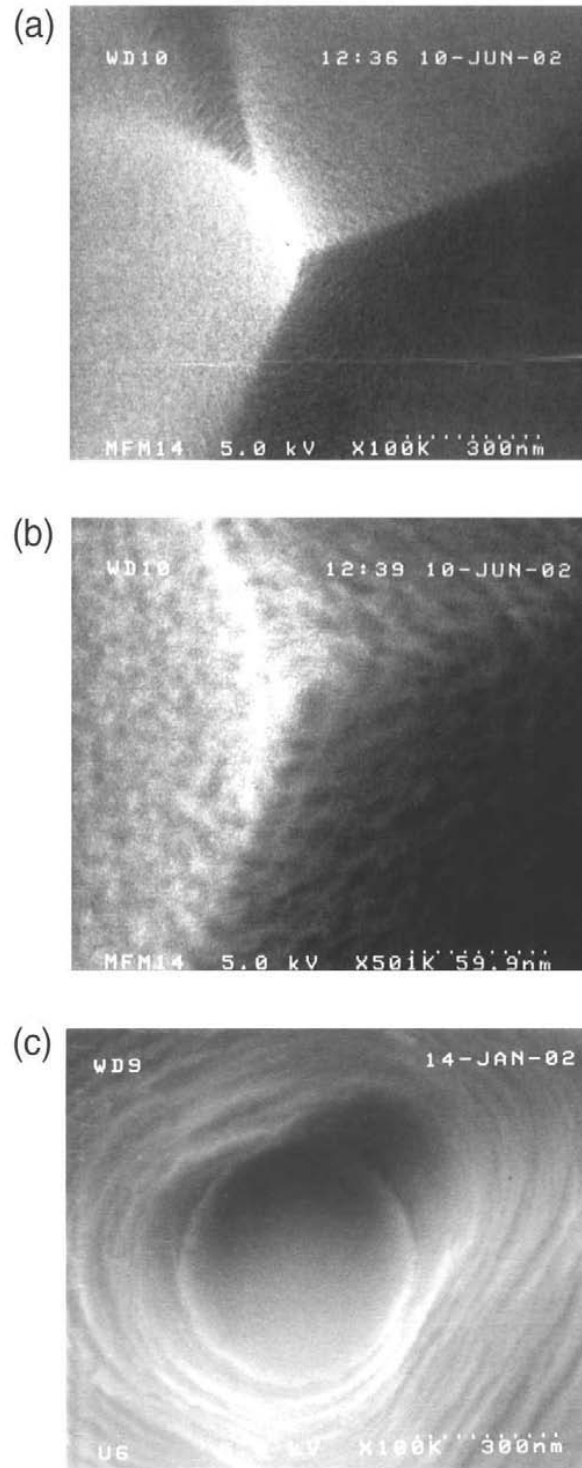


Figure 8.7: [AFM tip inspection] SEM images of (a) a clean and smooth AFM tip, (b) with a sharp apex, (c) a tip which has been purposely blunted to give a large and smooth apex.

of the scanning tube. The pinhole is mounted by three screws which allow some adjustment of its position. The position of the pinhole is coarsely aligned (light hits the back of the stencil chip) by hand, then tightened down. The microscope's XY coarse position system is then used to precisely center the pinhole on the stencil mask (since the mask is centered on the scanning tube, the tube is also aligned with the pinhole). We then align the AFM tip with the center of the stencil mask. The tip is first coarsely aligned by hand, then precisely centered on the mask with the XY positioning system. This last step results in a slight misalignment of the pinhole, but if care is taken at every step, the misalignment is small and poses no problem.

We use the AFM microscope to scan the stencil mask over (see chapter 7) a large area (usually about $(15 \mu\text{m})^2$). This way we verify that the features of interest are within scanning range, that the tip is above the stencil (an experienced user can tell the difference between imaging on and off a stencil mask) and that all the microscope components are working properly. Once this is done, the tip is retracted about $50 \mu\text{m}$ in Z, and the AFM assembly is clamped down. The microscope can now be moved to the evaporator room.

Before proceeding with placing the microscope under vacuum, great care must be taken to align properly the vibration isolation system. Once inside the chamber, the microscope will be exposed to a large amount of vibration and any problem with the spring-damping assembly may cause the pattern transfer to fail. We release the AFM assembly of its four springs and use the screws mounted at the end of each spring to carefully level horizontally the AFM assembly (using a leveling bubble). We also adjust the XY position of the springs' anchor points so as to avoid any contact between the AFM assembly flange and the pick-up system.

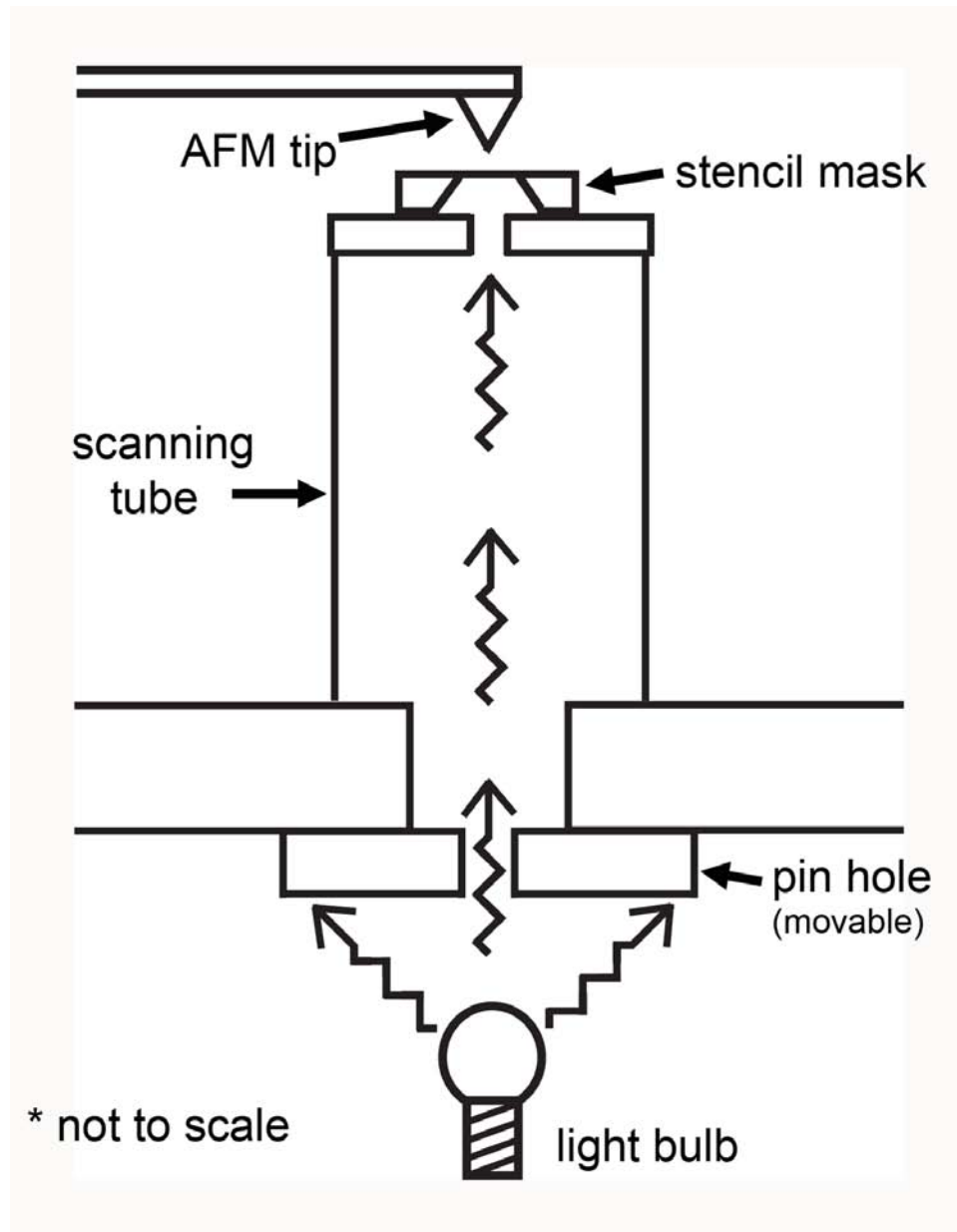


Figure 8.8: [Evaporation pin hole alignment] A diagram (not to scale) of the geometry used for aligning the evaporation pin hole with the scanning tube and stencil mask.

Similarly we also align the springs so that all the magnets in the damping system line-up properly with their respective copper fins. This process can be tedious, but is crucial. Once a proper alignment is achieved, the AFM assembly is clamped and the microscope is loaded in the evaporation chamber. We use the Big Blue evaporation system in Clark Hall. The loading process is made difficult by the weight of the microscope (> 50 pounds) and the tight fit of the microscope through the top flange of the evaporator. It can be done by one experienced person, but safety suggests that two people should be available for the loading procedure. We are now ready for business.

8.2.3 Evaporation

Table 8.1 summarizes the main steps of the transfer process. We have already discussed steps #1 through #7. The evaporation process we will now describe covers steps #8 through #17.

Once the microscope is loaded in the evaporator, we pump down the vacuum chamber to a pressure of $\approx 5 \times 10^{-7}$ Torr. The AFM assembly is then unclamped and suspended on its four springs. A large scale $(15 \mu\text{m})^2$ AFM image of the stencil mask is acquired to locate the structures of interest. We begin zooming on the features we want to transfer onto the tip. As soon as we take scans smaller than $\approx (5 \mu\text{m})^2$, we shift to a “constant height” scanning mode. To do this we retract the tip about 50 nm away from the surface and disengage the feedback system. The commercial imaging software that we use does not allow this, so we resorted to our own software and modified the TopoMetrix ECU (see section 7.2.3) to achieve constant height scanning. By adding an external voltage to the scanning electronics, we are able to “fool” the software into thinking that the tube is fully

extended while in actuality it is not. We then set the feedback parameters such that the tube wants to extend further (even though it cannot) which prevents the tube from retracting, thus effectively disabling the feedback system. We can then retract the tip 50 nm away from the surface by applying the appropriate voltage to the scanning tube. Once this is done, the surface is scanned as usual. The only difference is that now we cannot acquire information from the voltage applied to the scanning tube by the feedback system. Instead we acquire a topographic image of the stencil by monitoring the amplitude of the tuning fork (see section 7.2.3).

We need to use constant height imaging for two reasons. First, we find that scanning repeatedly the holes etched in the membrane for a long period of time (necessary to get rid of drift) deposits some dirt in the holes. Most likely the dirt is scooped in the holes by the tip. By using constant height imaging we protect both the stencil and the tip from unnecessary wear. Second, when the evaporator's e-gun is turned on, a lot of noise is generated by the electron beam and the associated heat. This noise, although filtered by our electronics, can occasionally result in a spike in the tuning fork signal. If the feedback electronics are engaged, this invariably causes the tip to crash in the stencil mask, destroying both the tip and stencil.

When scanning repeatedly the same small area, the scanning tube's deflection for a given voltage slowly settles to a precise value. Once the drift of the tube has been reduced to less than 1 nm/min or so, we turn on the e-gun filament and start to melt the metallic source. After the metallic source is melted, we position the AFM tip directly above the features to be transferred and retract the tip by a distance of 100 nm in Z. This extra distance is to prevent the tip from crashing because of the thermal drift during the pattern transfer. We shift the

Table 8.1: Pattern transfer procedure for stencil lithography on AFM tips

step	
#1	align the evaporation pin hole with the stencil
#2	align the tip with the stencil
#3	approach the tip to the surface
#4	afm the stencil to check everything is ok
#5	retract tip about 50 μm
#6	level afm assembly and align springs
#7	load the afm in the vacuum chamber
#8	pump down the vacuum chamber
#9	afm the stencil (tapping mode)
#10	zoom in on features (constant height mode)
#11	get rid of the scanning piezo drift's (wait)
#12	turn on e-gun and melt source
#13	aim tip above the mask and retract 100 nm
#14	lock the scanning tube position
#15	turn off the tuning fork drive
#16	evaporate metal
#17	back the tip away (200 μm)
#18	dismount afm tip from the tuning fork
#19	inspect the tip in a sem
#20	use the tip for SPM imaging

“fake” signal we use to hold the scanning tube in place to a battery source. This is necessary because when we open the evaporation shutter a very large amount of noise couples into the signal lines. In this environment, the large and quiet voltage of a 9 V battery provides us with a steady signal and prevents the scanning tube from moving during the evaporation. We proceed to turn off the tuning fork driving voltage (we are out of feedback). The drive voltage causes the fork and tip to oscillate with an amplitude of a few nm, and would smear the transferred features if we left it on.

We open the shutter and fire away. As soon as the desired film thickness has been deposited, we retract the tip 200 μm away from the stencil. We can now unload the microscope and tip. The tip is easily dismounted from the tuning fork by using narrow tweezers and some caution. To assess the success of our lithography, we use a SEM to image the deposited features (if the metal used as a good contrast). If the result is satisfactory, the tip is now ready to be used as a SPM probe. In the next sections we discuss how we characterize the resolution of our lithography on tips, and the SPM probes we fabricated.

8.3 Results

This technique works very well. In this section we show that we can do high-precision (10 nm) lithography on tips, even multiple layer lithography. We present results obtained with the first type of SPM probe we made, MFM tips. We also describe our progress toward making another type of probe, gated-STM tips.

8.3.1 Lithographic capabilities

To demonstrate the lithographic capabilities of this technique we use erbium (Er) as our deposition layer because it offers a good contrast in a SEM and sticks well to the tips. As discussed above (see section 8.2.1), in order to obtain tip surfaces suited for a demonstration of lithographic resolution we purposely blunt the tips.

Figure 8.9 (a) shows a SEM image of a 5×5 array of 20-nm-diameter erbium dots deposited at the apex of a tip. The interdot spacing in Fig. 8.9 (a) is 100 nm and a thickness of 50 nm of metal was evaporated. According to a previous study by Mandar Deshmukh *et al.* [2] it is possible to deposit a thickness of Er about 1.5 times the diameter of the holes etched in a stencil mask before these clog; thus we expect that the holes in the stencil used for Fig. 8.9 (a) became clogged during the deposition. Figure 8.9 (b) shows a pattern of five Er lines 20 nm wide and 400 nm long deposited on another tip. The line spacing is 100 nm and the thickness deposited is 40 nm. The features in Figs. 8.9 (a) and (b) are sharp down to a few nanometers, indicating minimal drift of the tip during the evaporation.

In Fig. 8.9 (c) we show a SEM image demonstrating our ability to align two separate layers of lithography on the same AFM tip, a procedure which can be required to make complex devices. First we deposited the 20-nm-wide, 30-nm-thick Er line using the procedure described above. Without breaking vacuum, we then repositioned the AFM tip over a perpendicular line-shaped hole etched in the same silicon nitride membrane and deposited the 10-nm-wide Er line at a right angle to the previous one. The second line-shaped hole is narrowed from its original width of 40 nm due to partial clogging during the first evaporation. Only a short section of the lines are displayed in Fig. 8.9 (c) due to the rounding of the tip (radius < 100 nm). This tip needed to be sharper than the ones displayed in

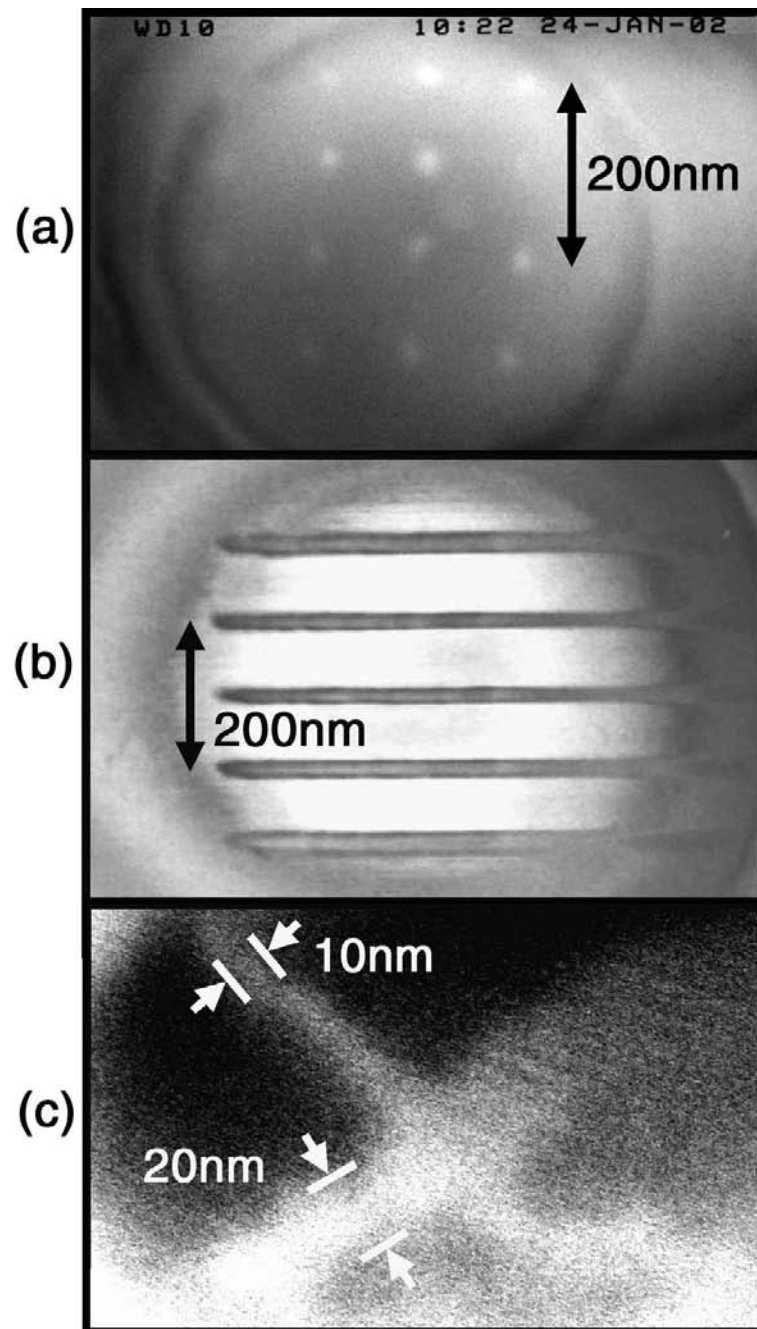


Figure 8.9: [Lithography on AFM tips] Test patterns made by depositing metal on AFM tips (a) A 5×5 array of 20-nm-diameter Erbium dots. (b) A pattern of five 20-nm-wide Er lines. (c) Two aligned layers of lithography at the end of one AFM tip, a 20-nm-wide Er line crossing a 10-nm-wide line.

panels (a) and (b) in order to achieve a good alignment between the two layers of lithography.

8.3.2 Magnetic probes

As a first application of the stencil technique for making functional SPM probes, we have deposited magnetic nanostructures on tips to serve as high spatial resolution magnetic force microscope (MFM) sensors. MFM is a technique widely used by the scientific community to image magnetic fields at surfaces, but has been limited to a spatial resolution of the order of 100 nm [9]. The MFM imaging technique was briefly explained in section 1.3. In short, to acquire a MFM image, an AFM tip covered with a magnetic film is scanned above a sample to record its topography, then the tip is retracted by some distance (few 10's of nm) and is scanned over the sample following the topography just recorded. This way the tip is always kept at a constant distance from the surface which means that any force due to van der Waals interaction is constant (and weak because of the distance). Thus the main contribution to the image contrast recorded during the second scan, by measuring the phase of the cantilever, is due to the interaction between the magnetic tip and the fields at the sample's surface.

Typically, commercial MFM tips are coated with a continuous ferromagnetic film. However, both the spatial resolution of MFM and the degree to which magnetic samples are perturbed by the tip can be improved by limiting the magnetic material to a small volume near the apex of the tip [9]. It has been shown that tips with a magnetic dot as large as 500 nm have an improved spatial resolution compared to similar tips coated with a continuous film [10]. A variety of different strategies have been pursued to make improved-resolution MFM tips

[9, 10, 11, 12, 13, 14, 15, 16]. The best clearly-demonstrated spatial resolution is to our knowledge a full width at half-maximum (FWHM) of 20 nm, which was achieved with AFM tips to which a carbon nanotube is attached [16]. The drawback of such tips is that they cannot be controllably fabricated, and only very few of them work well. For controllably fabricated tips, the best resolution demonstrated is 37 nm in two dimensions [12] and about 30 nm in one dimension [15].

The first step in fabricating our MFM probes is to determine what is the optimal magnetic material to deposit on our tips. We selected cobalt as our material of choice, because it can be evaporated easily, has a large magnetization, and only forms a thin oxide layer when exposed to air. A pure Co film has a very small coercivity which prevents us from knowing with confidence its magnetization direction. To improve the film coercivity we alloy Co with Cr [17]. Figure 8.10 shows the magnetization curves we measured for 50 nm thick films of Co, $\text{Co}_{90}\text{Cr}_{10}$, $\text{Co}_{80}\text{Cr}_{20}$, and a film of 50 nm of Co capped with a 20 nm film of Cr. We made these measurements using a vibrating sample magnetometer (VSM) in the laboratory of Prof. Yuri Suzuki. Figure 8.10 clearly shows that an optimal combination of magnetization and coercivity is obtained for the $\text{Co}_{90}\text{Cr}_{10}$ alloy. Due to a difference in vapor pressures of Co and Cr the composition of the mixture placed in the evaporation crucible is different from the composition of the film deposited by e-beam evaporation. The composition of the alloys of the film we deposited was measured using the JEOL 8900 Electron Microprobe available through CCMR.

To make MFM probes, we deposited single dots of $\text{Co}_{90}\text{Cr}_{10}$ alloy ranging in diameter from 140 nm to 25 nm at the end of sharp (unblunted) AFM tips using the stencil technique. We used commercially available tips [3] with a resonant frequency of 160 kHz and a spring constant of 5 N/m. We chose these relatively

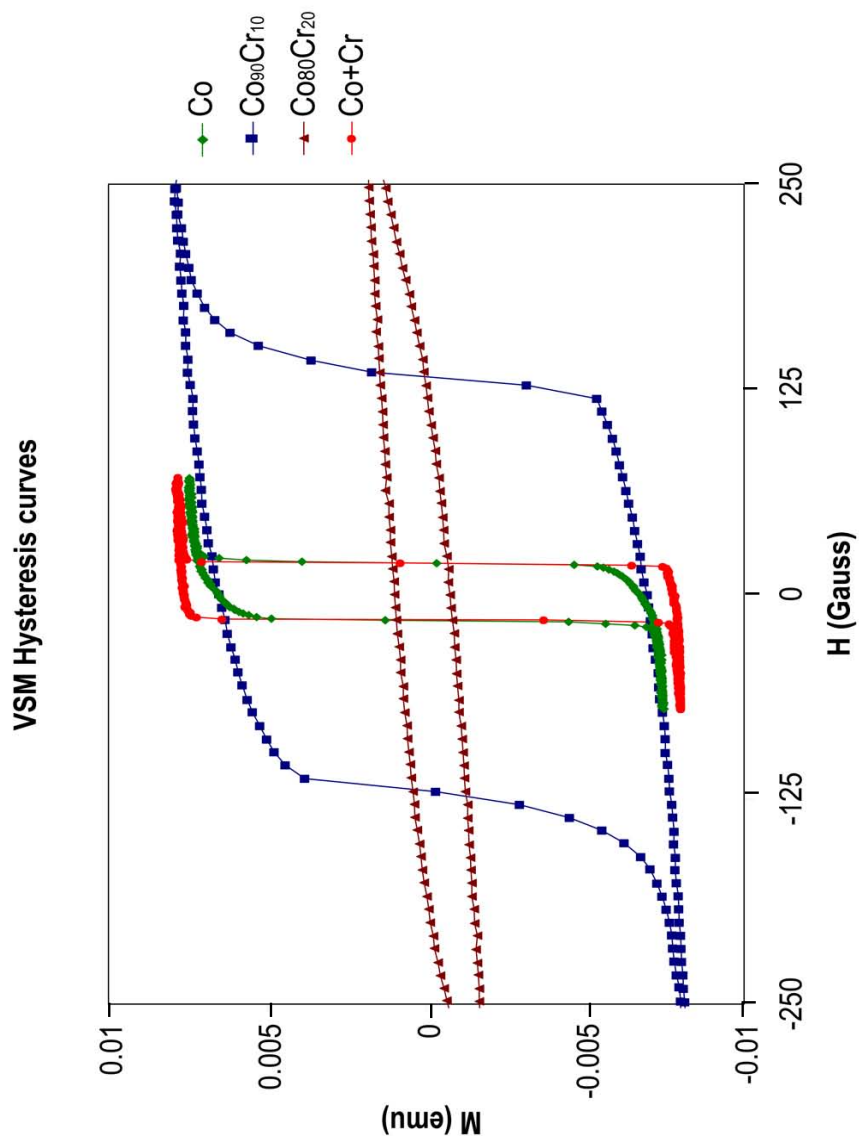


Figure 8.10: [Magnetic film characterization] Vibrating sample magnetometer (VSM) magnetization curves for different candidate films to be used on MFM probes: Cobalt, Cobalt + a capping layer of Chromium, $\text{Co}_{80}\text{Cr}_{20}$ alloy and $\text{Co}_{90}\text{Cr}_{10}$ alloy.

stiff cantilevers compared to the state of the art [18] because we performed our MFM testing in air, and therefore needed to avoid having capillary forces from adsorbed water disrupt the MFM imaging [19]. We found that the stiffness of the cantilever limited our force gradient sensitivity so that we could not sense magnetic signals with our smallest deposited structures. The use of floppier cantilevers in vacuum [20] would be necessary to test the full capabilities of the stencil technique. Nevertheless, even with relatively large deposited structures, our magnetic-dot tips exhibited resolution comparable to the best results reported previously [12].

As a first test of our tips we imaged a magnetic recording tape. Figure 8.11 (a) and (b) show respectively the topography and the magnetic signal phase contrast of the tape as recorded by one of our tips using a commercial microscope [21].

To test in more detail the performance of our MFM tips, we imaged 10 nm thick cobalt nanopillars with dimensions of 85 by 60 nm (Fig. 8.11 (c)) [22]. We fabricated these pillars using electron-beam lithography (VB6), and magnetized the pillars by exposing them to a large (600 mT) field parallel to their easy axis. Figure 8.11 (d) displays a magnetic phase contrast image of the magnetic dipole signal from one nanopillar, obtained using a tip with a stencil-fabricated 140-nm diameter CoCr dot, deposited with a normal-incidence thickness of 50 nm on the end of a tip with a nominal radius of curvature of 20 nm. The tip-sample spacing during the MFM imaging was approximately 25 nm. The FWHM resolution in Fig. 8.11 (d) is 42 nm, limited by the lateral extent of the magnetic source. With commercial MFM tips [23], we achieved at best a FWHM resolution of 60 nm.

The main advantage of the stencil technique over other approaches is that even better performance is possible. By using cantilevers with smaller spring constants,

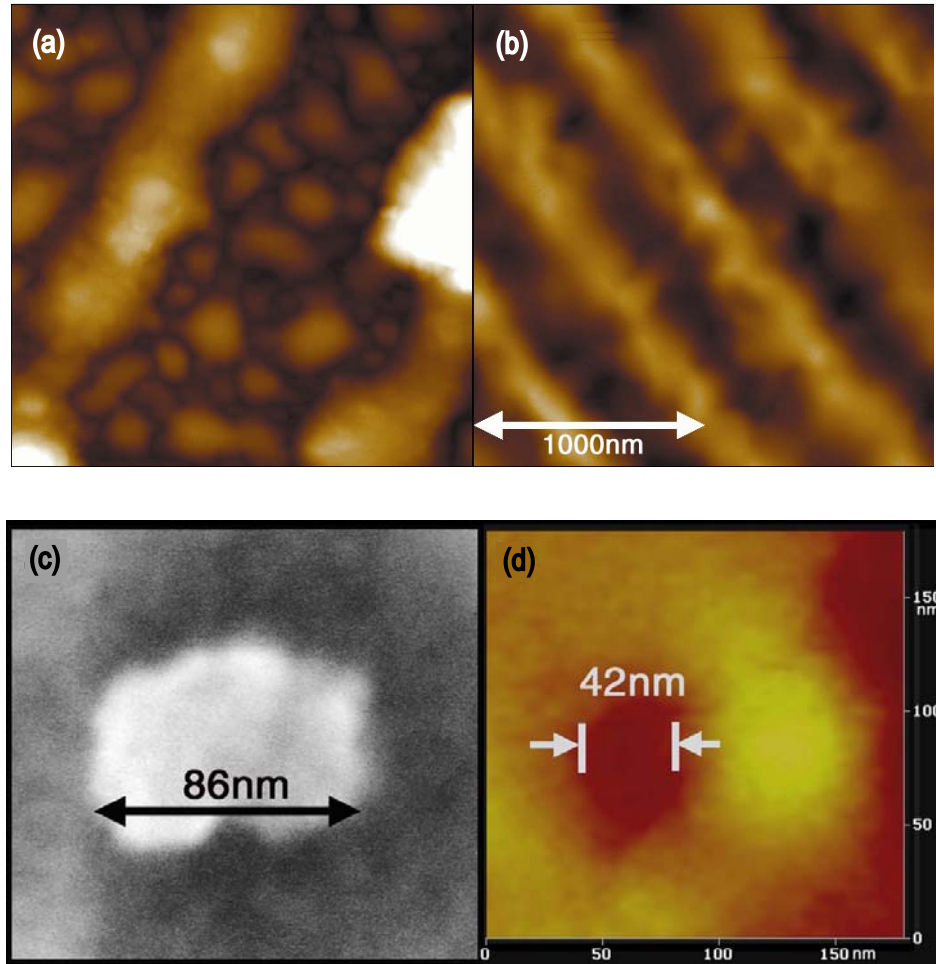


Figure 8.11: [Magnetic force microscopy with our sensors] MFM images acquired with an AFM tip at the apex of which a CoCr dot was stencil-deposited. (a) Topographic and (b) magnetic force images of a magnetic recording tape. (c) A SEM image of a cobalt nanopillar used for testing our MFM resolution and (d) a magnetic force image of a similar nanopillar.

the force gradient sensitivity can be enhanced by as much as a factor of 1000¹ [18], meaning that magnetic dots potentially as small as 10 nm, approaching the paramagnetic limit, might be used as MFM sensors. Furthermore, because the stencil allows us to pattern the shape of the deposited metal down to the 10 nm scale, the magnetic structure of the tip could be controlled to be a well-oriented dipole, making quantitative analysis of MFM images more straightforward [24]. The stencil technique also has the potential to produce many other types of functional SPM tips. Next we discuss progress toward making gated-STM tips.

8.3.3 Progress toward making strong coupling gated-STM probes

We want to make gated-STM (g-STM) tips with a gate-tip spacing of the order of 10 nm. This would greatly increase the sample-gate coupling [25], and allow us to perform spectroscopy on quantum dots (metallic grains, molecule, 2-DEG) on surfaces. The advantage of probe microscopy over other techniques used to study quantum dots is the possibility to image the object being studied.

In this section we describe the fabrication process for g-STM tips, but before we go into details, let us quickly overview the main fabrication steps. The first step in making g-STM tips or most other functional probes we would like to build, is to fabricate electrical leads that connect features deposited at the apex of the tip with the outside world. Once this done, we proceed to deposit at the apex of the tip a single line of Au with a narrow constriction at its center. We carefully

¹The force gradient sensitivity of a cantilever is proportional to $\sqrt{\frac{k}{Q\omega}}$, where k is the spring constant, Q is the quality factor and ω is the resonant frequency of the cantilever.

line up the Au line constriction with the tip apex and make sure that the Au line makes contact to the electrical leads connecting to the outside world. The next step would consist in using an electromigration process described in section 3.3 to open a gap in the constriction of the Au line. By performing electromigration on Au lines on flat substrates, we found that gaps of the order of 10 nm can be opened routinely. The two sides of the gap opened could then be used as a gate and tunnel electrode, making a g-STM tip. We have gone a long way in developing the technology necessary to build such probes.

Making electrical leads on AFM tips

We want to make two large electrical contacts on commercially available AFM tips. The two contacts should cover the silicon chip on which the tip is mounted so that wirebonding can be used to connect to them. The two contacts should also be centered on the AFM tip apex and have a small spacing ($< 10 \mu\text{m}$) so that they can easily be bridged by features deposited by stencil mask lithography.

To achieve these requirements we align a narrow ($< 10 \mu\text{m}$) tungsten wire above the apex of an AFM tip and use it as a shadow mask to deposit Au contacts on the tip. The tungsten wire cross-section is etched down using a KOH electrochemical etch. To align the wire precisely above the AFM tip (in close proximity), Ferdinand Kuemmeth fabricated a jig shown in Figure 8.12 (a). The wire is placed on the jig, and a series of fine screws can be used to align the tip under the wire. The jig was designed to fit under an optical microscope to facilitate the alignment (see 8.12 (b)). Once a satisfactory alignment is achieved, we load the jig inside the Sharon evaporator and deposit 150 nm of Au. Some commercial AFM tips are made of doped Si and are conducting. For these tips, we evaporated a layer of

SiO₂ 50-nm thick over the entire AFM-tip silicon chip before the Au evaporation. This prevented any shorting of the two evaporated Au electrodes.

Figure 8.13 shows SEM images of Au electrodes deposited on a tip. Panel (a) shows how the contacts go all the way down the cantilever beam and reach the Si chip, where they can be wirebonded. Panel (b) and (c) show respectively a side view and top view of the AFM tip. The last step in fabricating our Au contacts is to make sure that when we deposit features using stencil lithography, only the features at the tip apex will be connected to our contacts. Because our stencil masks are covered with many copies of the features we want to transfer, it is possible to short our Au electrodes somewhere on the cantilever part of the tip during the evaporation. To avoid this, we cap the Au electrodes on the cantilever with a layer of SiO₂. This method produces high quality contacts on AFM tips that meet all our requirements for building SPM probes.

Making a g-STM tip

Starting with a tip on which electrical leads have been deposited (see Fig. 8.13 (c)), we use a stencil mask similar to the one shown in Fig. 8.5 (b) to transfer a single line of Au on the apex of the tip. The line's length is such that it contacts the two macroscopic contacts on the tip. Furthermore, a narrow constriction in the center of the line is precisely aligned with the apex of the tip during the pattern transfer. This constriction can later serve to define the gate and tunnel electrodes by making use of electromigration.

Figure 8.14 (a), (b) show a top view of our first attempt to make a g-STM tip. We achieved a very good alignment of the line with the tip apex, and a good overlap with the Au contacts (see the side view in Fig. 8.14 (c)). Yet, we were not

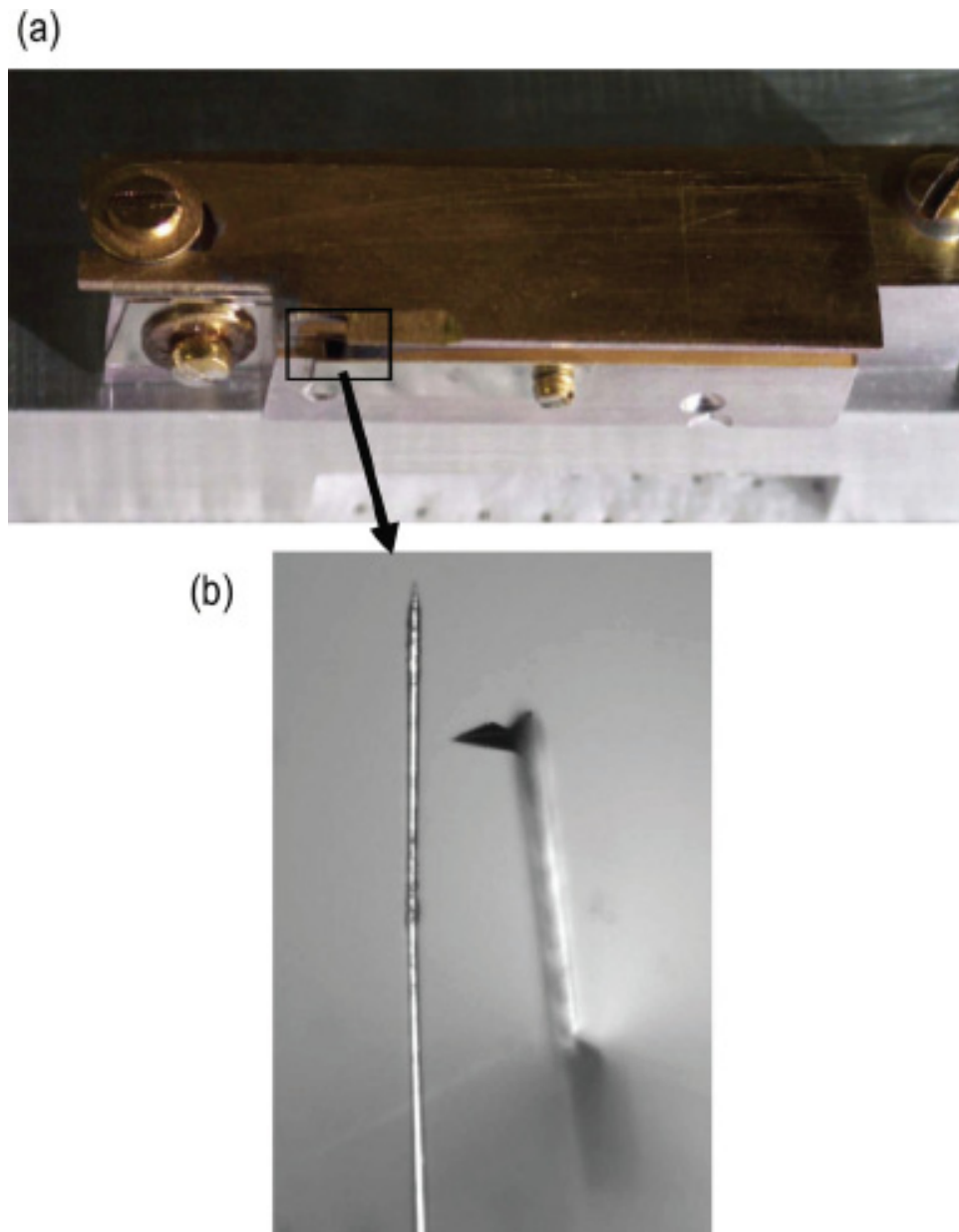


Figure 8.12: [Making macroscopic electrodes on AFM tips] (a) The jig used to deposit contacts onto AFM tips (this jig was made by Ferdinand Kuemmeth). (b) A close-up view showing the tungsten wire used as a shadow mask and an AFM tip.

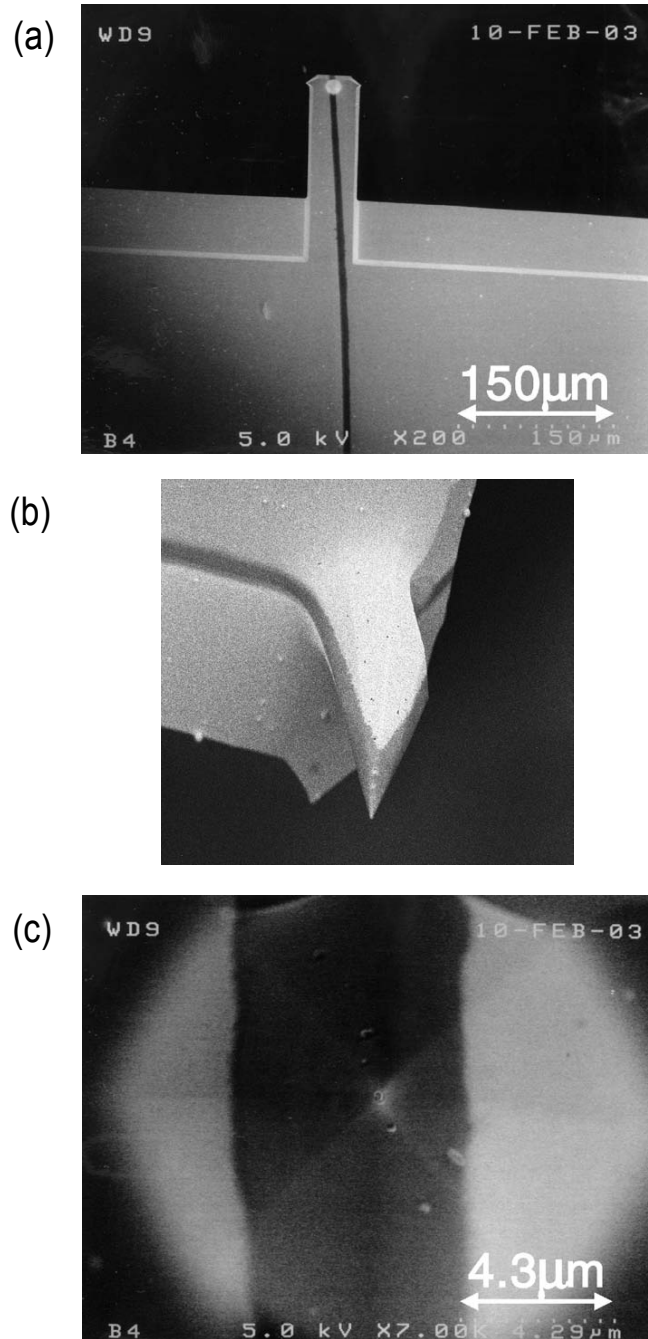


Figure 8.13: [Electrodes on an AFM tip] Views of a tip on which two Au electrodes were deposited. (a) The two contacts run up both sides of an AFM tip's cantilever all the way to the Si chip where they can be contacted by wirebonding. (b) Sideview, and (c) top view of an AFM tip with Au contacts.

successful in making a potent tip, because there was a defect in the stencil mask. The narrow constriction in the center of the line was not etched all the way across the stencil we used creating a large gap (≈ 200 nm) in the middle of the deposited Au line (see Fig. 8.14 (b)). We have no reason to believe that this initial lack of success is linked to any fundamental limitation of the technique. We are confident that devices can be made successfully.

Because we became interested in another fast developing project (see chapters 2-6) we put aside our effort in making g-STM tips. This project was not abandoned because it met any dead end, but for lack of time and man-power. The main challenge left in our endeavor to make high-resolution g-STM tips would be to characterize the tips once they are made. We would need to develop the hardware, software and electronics to make an effective use of such tips using a commercial AFM.

8.4 Outlook

We now reflect on the future of this method as a mean to fabricate SPM probes and its future prospect to deliver probes capable of making meaningful physical measurements. We anticipate that it would be possible to make both gated-STM tips and scanning-single-electron transistors with pattern definitions close to 10 nm [25, 26]. This would greatly increase the sample-gate coupling in gated-STM and would allow operation of scanning single-electron transistors at temperatures well above 1 K [26]. Other applications are also imaginable, including improved near-field optical probes [27] and scanning thermal microscopy (SThM) tips [28]. These projects are technologically challenging and very much labor intensive.

The current fabrication tool (our homemade AFM) does the job we intended it

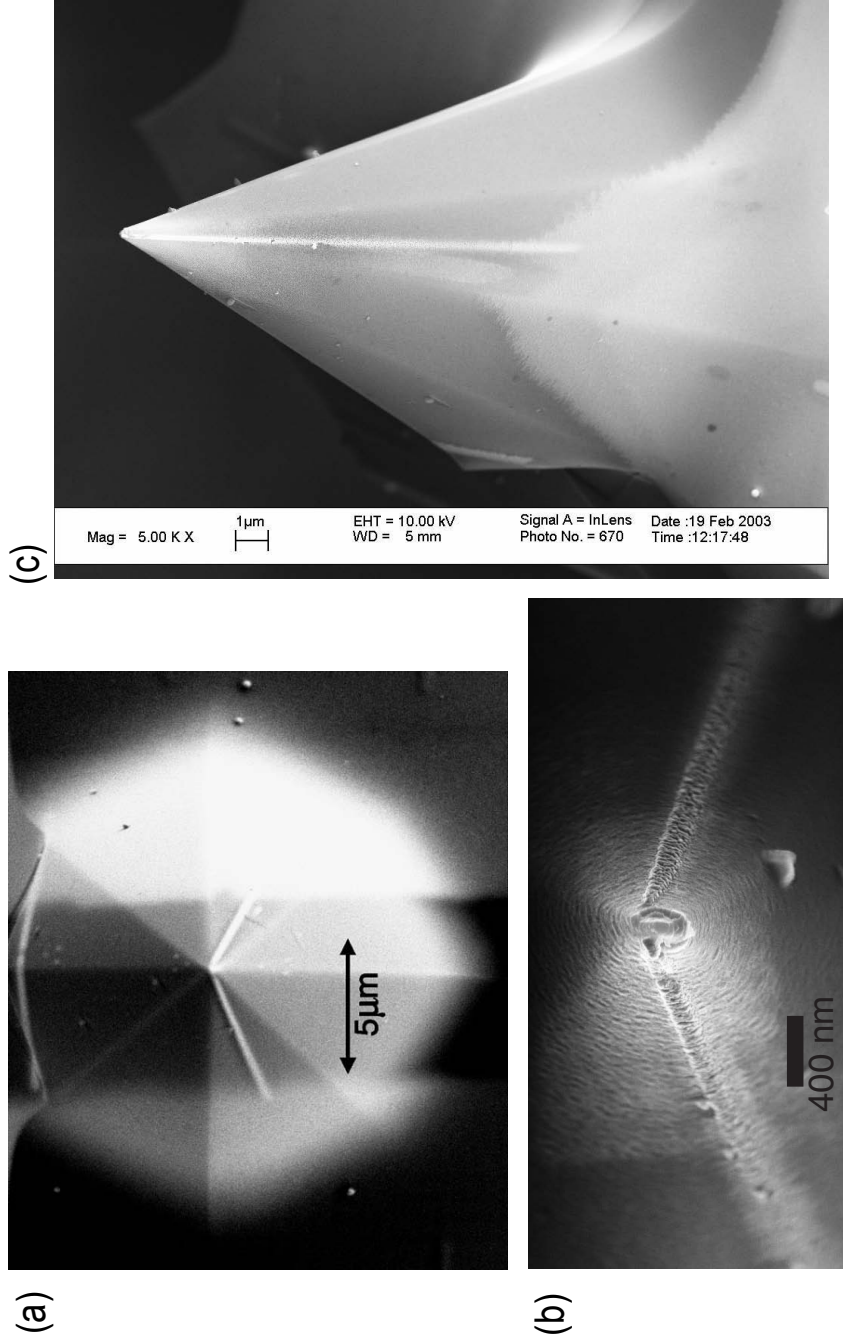


Figure 8.14: [Gated-STM tip] A first attempt at making a gated-STM tip with a small gate-tip spacing. A single Au line with a constriction at its center was evaporated on the apex of an AFM tip, contacting two macroscopic electrodes previously deposited on the tip. (a) A top view of the tip, (b) zooming in we see that the stencil had a defect in its center causing the line to be broken. (c) Sideview showing the overlap between the line and one of the large Au electrodes.

to do (I still can't believe it). Once optimized this fabrication method is robust and has a high yield, > 50% for one step lithography. Yet, the production of sensors is very slow. It takes a good two days to make a simple tip (when everything is working). Moreover, due to their small size, these sensors are very fragile. Any contact between one of our SPM sensors and the surface being imaged risks destroying the probe. The combination of these two facts make it painfully difficult to make interesting physical measurements with our sensors. However, if we can only increase the number of tips we can fabricate by a factor of a few, we will be in a position to carry out many completely original and fascinating physical experiments. So the question stands, how do we get this factor of a few in the number of probes we can make in a given time?

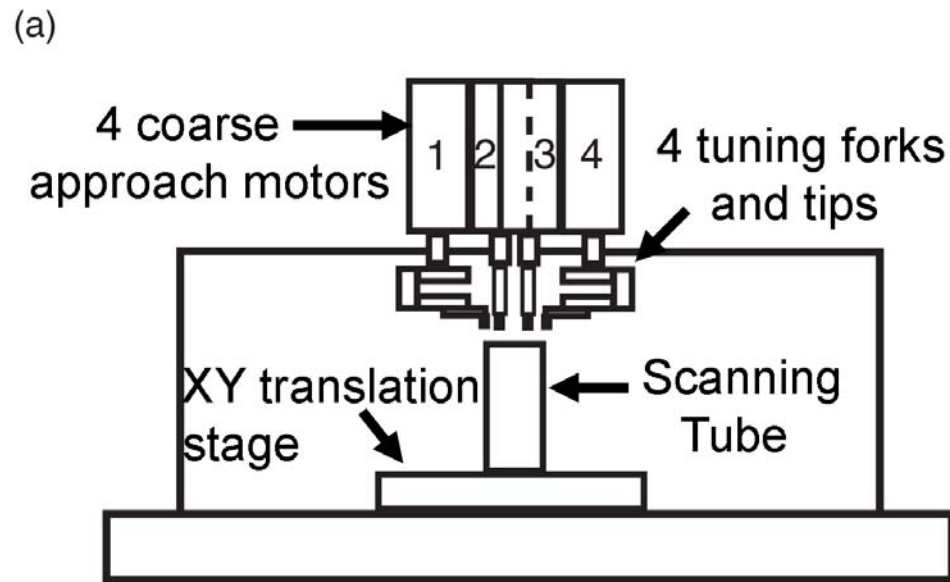
We would need to build a new AFM which would be better suited to do the work. The current microscope has some serious design flaws that make it cumbersome to use. While we have made numerous changes to the original design to improve the microscope's performance, it remains difficult to operate. I now list some of the improvements that the new design should include to really propel the project forward:

1. The microscope should be light and compact (no more than 10-15 pounds heavy, and 10 inches high).
2. It should be made to fit in a currently used evaporation system (Sharon) to alleviate the need to maintain a separate system.
3. It should allow the fabrication of 4 tips in one evaporation run.
4. The stencil masks need to be fabricated with 4 windows per chip to accommodate the 4 tips to be fabricated in one run.

5. A more compact and accurate XY translation system is needed.
6. The clamping-spring system needs to be practical and easy to use.
7. The software would need to be upgraded into one single program.
8. A larger cross-section scanning tube and pinhole should be used.

Although the task of building a new AFM may seem daunting, I believe it can be done quickly by keeping the system small and compact and using commercial solutions. Figure 8.15 (a) shows a cartoon of the proposed new AFM assembly. Figure 8.15 (b) shows an excellent candidate for a precise and compact (fits in a 10 mm diameter) XY translation stage (ThorLabs).

Oh well, if I ever get to have my own graduate students, I'll give this a try.



(b) XY translation stage (Thorlabs)



Figure 8.15: [New AFM design] (a) Cartoon of the new AFM assembly. The two main changes from the previous version are: there are now four AFM tips that can be loaded at once in the microscope, the XY translation system is much more compact and accurate. (b) A commercially available XY translation system that meet the requirements of the new AFM design.

BIBLIOGRAPHY

- [1] A. R. Champagne, A. J. Couture, F. Kuemmeth, and D. C. Ralph, *Applied Physics Letters* **82**, 1111 (2003).
- [2] M. M. Deshmukh, D. C. Ralph, M. Thomas, and J. Silcox, *Applied Physics Letters* **75**, 1631 (1999).
- [3] Mikromasch, <http://www.spmtips.com>.
- [4] K. S. Ralls, R. A. Buhrman, and R. C. Tiberio, *Applied Physics Letters* **55**, 2459 (1989).
- [5] D. C. Ralph, C. T. Black, and M. Tinkham, *Physical Review Letters* **74**, 3241 (1995).
- [6] M. M. Deshmukh, PhD thesis, Cornell University, (2002).
- [7] E. B. Myers, PhD thesis, Cornell University, (2002).
- [8] J. R. Petta, PhD thesis, Cornell University, (2003).
- [9] U. Hartmann, *Annual Review of Materials Science* **29**, 53 (1999).
- [10] S. H. Liou, *IEEE Transactions on Magnetics* **35**, 3989 (1999).
- [11] P. B. Fischer, M. S. Wei, and S. Y. Chou, *Journal of Vacuum Science & Technology B* **11**, 2570 (1993).
- [12] G. D. Skidmore and E. Dan Dahlberg, *Applied Physics Letters* **71**, 3293 (1997).
- [13] T. Arie, H. Nishijima, S. Akita, and Y. Nakayama, *Journal of Vacuum Science & Technology B* **18**, 104 (2000).
- [14] L. Folks et al., *Applied Physics Letters* **76**, 909 (2000).
- [15] G. N. Phillips, M. Siekman, L. Abelman, and J. C. Lodder, *Applied Physics Letters* **81**, 865 (2002).
- [16] Z. F. Deng et al., *Applied Physics Letters* **85**, 6263 (2004).
- [17] K. Babcock, V. Elings, M. Dugas, and S. Loper, *IEEE Transactions on Magnetics* **30**, 4503 (1994).
- [18] H. J. Mamin and D. Rugar, *Applied Physics Letters* **79**, 3358 (2001).
- [19] D. A. Grigg, P. E. Russell, and J. E. Griffith, *Journal of Vacuum Science & Technology A* **10**, 680 (1992).

- [20] M. Dreyer, R. D. Gomez, and I. D. Mayergoyz, *IEEE Transactions on Magnetics* **36**, 2975 (2000).
- [21] Digital Instruments Dimension 3100 AFM.
- [22] S. Evoy et al., *Journal of Applied Physics* **87**, 404 (2000).
- [23] Nanoprobe SPM tips, MESP 66-83 KHz.
- [24] P. J. A. van Schendel, H. J. Hug, B. Stiefel, S. Martin, and H. J. Guntherodt, *Journal of Applied Physics* **88**, 435 (2000).
- [25] L. Gurevich, L. Canali, and L. P. Kouwenhoven, *Applied Physics Letters* **76**, 384 (2000).
- [26] M. J. Yoo et al., *Science* **276**, 579 (1997).
- [27] R. D. Grober, R. J. Schoelkopf, and D. E. Prober, *Applied Physics Letters* **70**, 1354 (1997).
- [28] D. G. Cahill, K. Goodson, and A. Majumdar, *Journal of Heat Transfer-Transactions of the Asme* **124**, 223 (2002).

Appendix A

Numerical simulation of Coulomb blockade in mechanically-adjustable single-molecule transistors

A.1 Introduction

This simple code generates $I - V$ characteristic curves of electronic transport through a quantum dot using the orthodox Coulomb blockade theory. The effect of mechanically tuning the source-drain spacing is simulated by allowing the device's capacitances to linearly evolve between their initial and final values as experimentally measured. The tunnel junctions' resistances are allowed to increase exponentially with motion, and the rate of their increase is adjusted so that the shape of the obtained $I - V$ s mimics the data. This simulation is used to gain intuition for the origin of the features in the data, but cannot be taken too seriously because it contains many adjusted parameters.

A.2 Mathematica code

```
(* Number of charge states evaluated, number of voltage steps, motor steps *)
```

```
MaxStates = 3; VStep = 400; MTurns = 21.5; Mstepsize = 0.25;
```

```
(* Setting up arrays *)
```

```
Tsize = IntegerPart[(MTurns/Mstepsize) + 1];
```

```
Tsize2 = IntegerPart[(MTurns/(4*Mstepsize) + 1) ];
```

```
Array[bb,VStep, Tsize, 3]; Array[dd, VStep, Tsize, 3];
```

```

CC = Table[0, i, 1, VStep*Tsize, j, 1, 3];
R1R = Table[0, i, 1, 2*MaxStates + 1];
R1L = Table[0, i, 2*MaxStates + 1]; R2R = Table[0, i, 2*MaxStates + 1];
R2L = Table[0, i, 2*MaxStates + 1];
P = Table[0, i, 2*MaxStates + 1];

(* Temperature, Boltzman constant, charge of the electron and free space permit-
tivity *)
Temp = 4.22; K = 1.38*10^-23; EL = -1.602*10^-19; E0 = 8.85 *10^-12;

(* Initial and final capacitances *)
CLS = 1.55*10^-18; CLF = 1.6*CLS; CRS = 1.3*10^-18; CRF = 2.6*CRS; CG
= CLS/300;

(* Capacitance step size *)
CRstep = (CRS - CRF)/(Tsize - 1); CLstep = (CLS - CLF)/(Tsize - 1);

(* Calculates the tunnel junction initial size(gap). This is just a way to let the
resistance evolve smoothly with motion. The value obtained is meaningless. *)
Area = 60*10^-18;
DLS = (Area * E0) /CLS;
DRS = (Area * E0) /CRS;

(* Displacement per motor turn *)
DXL = 0.6*10^-12; DXR = 0.3*10^-12;

(* Chemical potential difference between the leads and dot *)
DPHI = 0.027;

For[k = 0, k = (MTurns/Mstepsize), k++,
DL = DLS + (k* DXL); DR = DRS + (k* DXR);
If[k = Tsize2, CL = (CLS - (4*k*CLstep)) ];

```

$$CR = CRS - (k*CRstep);$$

(* Total capacitance *)

$$CS = CL + CR + CG;$$

(* Offset charge as a function of displacement *)

$$Q0 = (CL * DPHI + CR*DPHI) - (CLS * DPHI + CRS*DPHI) + (0.32* EL);$$

(* Tunnel resistances *)

$$RLS = 0.9*10^5; RRS = 1.7*10^5;$$

$$RL = RLS * \text{Exp}[2.3*((DL - DLS)/DLS)]; RR = RRS * \text{Exp}[2.3*((DR - DRS)/DRS)];$$

$$NS = 1;$$

(* Lead potentials, at start and end for the left lead, right lead, gate *)

$$VLS = -0.0433; VLE = 0.0502; VR = 0; VG1 = 0.0;$$

$$VLStepsize = (VLE - VLS)/VStep;$$

(* Voltage Cycle *)

$$\text{For}[VL = VLS, VL < VLE, VL += VLStepsize,$$

(* Potential of the island *)

$$\text{For}[x = 1, x \leq 2*MaxStates + 1, x++,$$

$$NE = x - MaxStates - 1;$$

(* To account for effective gate sweeping when bias sweeping *)

$$V2 = (CL*VL + CG*VG1 + Q0 + EL*NE)/CS;$$

$$VG2 = (VG1 - V2);$$

$$V = (CL*VL + CR*VR + CG*VG2 + Q0 + EL*NE)/CS;$$

(* Change in energy after tunneling *);

$$LF = EL^2 / (2*CS) + EL*V - EL*VL;$$

$$RF = EL^2 / (2*CS) + EL*V - EL*VR;$$

$$LO = EL^2 / (2*CS) - EL*V + EL*VL;$$

```

RO = EL^2 / (2*CS) - EL*V + EL*VR;
(* Tunneling rates 1, 2 - junctions, L, R - direction *);
R1R[[x]] = N[LF / (EL^2*RL*(Exp[LF/(K*Temp)] - 1))];
R1L[[x]] = N[LO / (EL^2*RL*(Exp[LO/(K*Temp)] - 1))];
R2R[[x]] = N[RO / (EL^2*RR*(Exp[RO/(K*Temp)] - 1))];
R2L[[x]] = N[RF / (EL^2*RR*(Exp[RF/(K*Temp)] - 1))];
];
(* Occupation number probabilities *);
P[[MaxStates + 1]] = 1;
For[i = MaxStates + 2, i <= 2*MaxStates + 1, i++,
P[[i]] = P[[i - 1]]*(R2L[[i - 1]] + R1R[[i - 1]]) / (R1L[[i]] + R2R[[i]]);
For[i = MaxStates + 1, i >= 1, i--,
P[[i - 1]] = P[[i]]*(R1L[[i]] + R2R[[i]]) / (R2L[[i - 1]] + R1R[[i - 1]]);
(* Setting up the answer array *);
Su = Sum[P[[n]], n, 1, 2*MaxStates + 1];
Current = Sum[EL*P[[i]]*(R1R[[i]] - R1L[[i]]), i, 1, 2*MaxStates + 1, 1]/Su;
bb[NS, k + 1, 1] = CC[[NS + k*VStep, 1]] = VL;
bb[NS, k + 1, 2] = CC[[NS + k*VStep, 2]] = Current;
bb[NS, k + 1, 3] = CC[[NS + (k*VStep), 3]] = k * Mstepsize;
];
]

```